EXAMINING VERY-LONG-TERM VARIABILITY IN X-RAY BINARIES: ARE ULTRALUMINOUS X-RAY SOURCES INTERMEDIATE MASS BLACK HOLES?

By

Deatrick Foster

Dissertation

Submitted to the Faculty of the

Graduate School of Vanderbilt University

in partial fulfillment of the requirements

for the degree of

DOCTOR OF PHILOSOPHY

in

PHYSICS

December, 2013

Nashville, Tennessee

Approved:

Dr. Keivan G. Stassun

Dr. Philip A. Charles

Dr. David A. Weintraub

Dr. Richard Haglund

Dr. David J. Ernst

DEDICATION

This thesis is dedicated to the loving memory of Joe and Dollie.

ACKNOWLEDGMENTS

I would like to thank my advisers, Dr. Keivan Stassun and Dr. Philip Charles. Without their care, enthusiasm, encouragement and guidance this thesis would not have been possible. I am thankful for my PhD committee members, along with all of my collaborators. Your support was critical to my development as a scientist. I thank Dr. Hakeem Oluseyi, Dr. Abebe Kebede, Dr. James L. "Jim" Smith, Dr. Reva Kay Williams, and Dr. Anthony Johnson, Dr. Jarita Holbrook, and Dr. Doug Swartz for their sound advice, support, mentoring, and friendship.

I would like to acknowledge the National Society of Black Physicists (NSBP), which was critical to my completing this PhD. I would also like to acknowledge funding I received in the form of a NASA Harriett G. Jenkins Fellowship (NASA-JPFP), a National Physical Science Consortium (NPSC) Fellowship, a Vanderbilt Initiative in Data-intensive Astrophysics (VIDA) Fellowship, and the Graduate Assistance in Areas of National Need (GAANN) Fellowship. I would like to thank the Fisk-Vanderbilt Bridge Program for very critical support I received while at Vanderbilt, the Vanderbilt-Cape Town Partnership, the University of Cape Town and the South African Astronomical Observatory.

Finally, and most importantly, I thank my family and friends for their love and support, especially my mother, Lynda, my sister Darneshia, and my aunt Sheeila.

Table of Contents

List of Tables

List of Figures

Chapter I

INTRODUCTION

The immense temperatures and pressures in the cores of stars causes the conversion of hydrogen into helium via nuclear fusion, which produces vast amounts of radiation (Arnett & Clayton, 1970; Arnett, 1973). A star spends most of its life in rough balance between the inwardly-directed gravitational forces due to matter and the outwardly-directed radiation forces due to nuclear fusion. Once the hydrogen fuel is consumed, gravitational forces become dominant and the star contracts. This contraction causes the temperature and pressure in the core to rise, which allows the star to begin fusing the helium in its core to produce carbon and oxygen (Woosley and Weaver, 1995; Woosley et al., 2002).

Fusion continues and produces elements such as oxygen, neon, and magnesium for stars with initial (birth) masses $\simeq 6 - 7$ $M_\odot$. For stars with initial masses ≤ 8 $M_\odot$, the fusion processes come to an end, resulting in the star becoming a white dwarf. Heavier elements up to iron are synthesized in the cores of more massive stars (10 – 140 $M_\odot$; Heger et al., 2003) that have greater core densities and temperatures. Eventually, the stellar cores of the most massive stars collapse under their own weight and explode as supernovae. Depending on the details, but primarily on the initial mass, a supernova can leave a compact remnant such as a neutron star or black hole,

or it can be so powerful that the explosion leaves nothing behind (Heger and Woosley, 2002; Heger et al., 2003; Heger, 2013).

Black holes are exotic, compact astrophysical objects whose gravity is so strong that neither matter nor radiation can escape their gravitational fields. They are important in modern physics because their enormous densities are unlikely to be reproduced in the laboratory and thus they are places where unique physical interactions can occur. Formally, the center of a black hole has infinite density and the conventional physical laws break down at this extreme condition.

In this chapter, we review the basic properties of black holes such as their formation, growth, and environments, as well as the standard model of disk accretion. Important observational discoveries and milestones are discussed, including the confirmation of stellar-mass black holes as astronomical entities and the formation and growth of supermassive black holes.

1.1 Black Holes

Black holes have become an integral feature of modern astrophysics. To date, black holes are known to have masses in two ranges: stellar-mass (i.e. masses in the range of 5 to 15 times the mass of our Sun) which result from the end-of-life processes in massive stars, and supermassive (i.e. masses in the range of millions to billions of times the solar mass) which are found in the centers of nearly all galaxies and are believed to form and grow in lockstep with their host galaxies. There exists

a third, speculative category of black holes, the so-called intermediate-mass black holes (IMBHs), which as their name implies, have masses in the range between that of stellar-mass and supermassive black holes. Unlike the other two types of black holes, there is as yet no hard evidence that IMBHs exist, and no widely accepted theory about how they form; however, there are several IMBH candidates that if confirmed would require a dramatic revision of stellar evolution theory. From what we already know about stellar evolution, if IMBHs do indeed exist they would require very unusual physical conditions to form (Miller and Colbert, 2004).

As strange as black holes are, their properties can be completely expressed in terms of just three parameters: their mass, their electrical charge, and their angular momentum (i.e. spin). Therefore, the study of these important objects hinges on measuring or constraining these three parameters. Astrophysicists are certain that the electrical charge is negligible.

1.1.1 Stellar-mass Black Holes

Stellar-mass black holes result from normal stellar evolution of massive stars. They can form during the collapse of single stars or in binary evolution. There are at least two distinct formation mechanisms—direct collapse or supernova fallback onto a neutron star. Above some initial mass limit, the progenitor star collapses to form a black hole; however, this mass limit can be very different for single stars versus binary stars. In general, the mass limits compare as $M_{BH}^{S} < M_{BH}^{B}$ and it is fairly

certain that $M_{BH}^{S} < 25M_{\odot}$. Here, M_{BH}^{S} and M_{BH}^{B} represent the initial mass limits in the cases of single and binary stars, respectively. M_{BH}^{B} is larger because of increased mass-loss of the primary component in a binary (Fryer, 1999; Heger, Fryer, Woosley, Langer & Hartmann, 2003). Explosions of $\approx 20M_{\odot}$ stars (e.g. *SN 1987A*) give a lower limit to initial stellar mass needed for direct black hole collapse. Stellar-mass black holes have masses in the range $5 - 15M_{\odot}$. Winds and metallicity of progenitor stars are important factors in the formation of stellar-mass black holes and have a lowering effect on the size of the resultant black holes (Fryer, 1999). This is because the radiation pressure generated in the normal stellar evolution process has a larger cross section on which to act since the abundances of heavy elements are increased in higher-metallicity stars. The winds push away heavier nuclei more efficiently than lighter elements, leaving less material behind to collapse into the eventual black hole.

1.1.2 Supermassive Black Holes

Supermassive black holes (SMBHs) are at the dynamical centers of nearly all galaxies (Kormendy and Richstone, 1995; Magorrian et al., 1998). They formed early, possibly before the first stars, due to coherent gravitational collapse in the proto-galactic dark matter halos (Silk and Rees, 1998; Di Matteo et al., 2005). Because of this their formation and growth is strongly tied to that of their host galaxies. SMBHs are in the $\sim 10^{6} - 10^{9.5}M_{\odot}$ mass range. Simulations of galactic mergers that take into account the effects of black hole mergers and quasar feedback support the co-

evolution hypothesis (Volonteri, 2007). The spin of the SMBH changes during the merger with the secondary black hole, or through interacting with the accretion disk and central stars of both galaxies. The coalescence of the black holes does not lead to a systematic effect on the spin, but rather leads to a random-walk about the birth value of the spin. On the other hand, accretion generally acts to increase the spin of the black hole, even if the spin orientation is dynamical. These simulations also show that the spin distribution in SMBHs is skewed toward the rapidly spinning end of the spectrum, that the high spin is established early in the lifetime of the SMBH, and that the spin does not vary much below redshift $z = 5$ (Volonteri, 2007).

1.1.3 Intermediate-mass Black Holes

Intermediate-mass black holes (IMBHs) cover the $\sim 10^2 - 10^4 M_\odot$ mass range and can possibly form by runaway stellar collisions in the centers of dense star clusters (Portegies Zwart and McMillan, 2002). The massive objects can grow to be about 0.1% of the total mass of their host cluster. The growth of an IMBH is halted by sufficiently high mass loss due to stellar evolution. IMBHs formed similarly in other dense clusters can migrate to the center of the galaxy and collide with each other, forming a SMBH. It is plausible that IMBHs can be remnants of Population III stars. Unambiguous detections of IMBHs are not yet a reality, however observations of the X-ray source ESO 243-49 HLX-1 places it among the strongest IMBH candidates (Farrell et al., 2009). It's peak X-ray luminosity and disk-blackbody spectrum imply

a black hole mass of $\sim 10^4$ $M_\odot$ (Farrell et al., 2009; Davis et al., 2011; Servillat et al., 2011; Godet et al., 2012).

1.2 The $M_{bh} - \sigma$ Relation

Theories of galaxy evolution and massive black hole formation have, as either a starting point to be expanded upon or as an implication of a particular theory itself, a relationship between the mass M_{bh} of the central supermassive black hole (SMBH) and the velocity dispersion σ of stars orbiting the galaxy within its half-light radius (Gültekin et al., 2009), and predict that $M_{bh} \propto \sigma^{4-5}$. One such theory is that of Silk and Rees, who hypothesized that massive black hole formation predates galaxy formation and that, through a feedback mechanism, the primordial clouds in which the massive black holes form (via "coherent [gravitational] collapse" of the proto-galactic gas into giant black holes of $M_{bh} \gtrsim 10^6 M_\odot$ before star formation can occur) provide the seed materials for the formation of smaller galaxies through powerful quasar outflows (Silk and Rees, 1998). There are several competing models that attempt to explain the observed $M_{bh} - \sigma$ relation as well, with mechanisms as varied as viscous disk accretion, adiabatic black hole growth, stellar capture by accretion disks, dissipationless merging, gas and dark matter collapse, et cetera (Robertson et al., 2006, and references therein).

Simulations provide further insight into just how the $M_{bh} - \sigma$ relationship is established by galaxy-galaxy collisions (Di Matteo et al., 2005). Accretion of gas onto

the SMBH at near-Eddington rates is typically the phase of black hole growth following their formation. An accretion wind develops to the point that it halts the growth of the central black hole until the galaxy undergoes a merger. The dual growth mechanisms of black hole coalescence and/or accretion of the freshly supplied gas continue the process of massive black hole evolution. High accretion rates again generate powerful outflows of material. Eventually, a balance is established between the masses of the central SMBHs and the masses of the central bulges of the galaxies in which they reside (Silk and Rees, 1998; Magorrian et al., 1998; Di Matteo et al., 2005). Through the competing effects of accretion-generated winds that drive gas out and hierarchical merging that replenishes the gas, the massive black holes are fed at a rate sufficient to expel nearly all the surrounding gas from their immediate neighborhoods yet stimulate star formation in shells of ejected materials that can fragment and cool efficiently. Growth of the galaxies through mergers and the continued growth of the SMBHs through accretion form a self-regulating process that maintains this balance: by conjecture, the dependence of black hole mass upon the spheroidal mass is believed to rise "more rapidly than linearly." (Silk and Rees, 1998) Stimulated by these ideas, Silk and Rees derived a mathematical relationship between M_{bh} and σ that predicted a log-space slope of 5, which is close to, but a bit larger than, what the most recent observations show. However, the predicted normalization agrees very well with the latest observations (Gültekin et al., 2009). The relationship is $\log(M_{bh}/M_{\odot}) = \alpha + \beta \log(\sigma/200 \text{ km s}^{-1})$, with α being the normalization and β

being the power-law index.

Observationally, stellar- and gas-dynamical studies of elliptical galaxies and spiral bulges led to the conclusion that nearly all such galaxies have a massive central dark component that is most certainly a SMBH (Kormendy and Richstone, 1995). Furthermore, the discovery of the low intrinsic scatter (ϵ_0) of the $M_{bh} - \sigma$ correlation implies a connection between black hole formation and galaxy evolution (Ferrarese and Merritt, 2000; Gebhardt et al., 2000). The latest results show best-fit values of (α, β, ϵ_0) = (8.12 $\pm$ 0.08, 4.24 $\pm$ 0.41, 0.44 $\pm$ 0.06) for all galaxies and (α, β, ϵ_0) = (8.23 $\pm$ 0.08, 3.96 $\pm$ 0.42, 0.31 $\pm$ 0.06) for elliptical galaxies (Figure 1.1; Gültekin et al., 2009). To date, no other parameter or combination of parameters have been shown to constrain the central black hole mass with less scatter than σ (Gebhardt et al., 2003).

Two important aspects of the $M_{bh} - \sigma$ relation are: (1) it is relatively easy to measure velocity dispersion with fairly standard techniques involving the broadening of absorption lines (Franx et al., 1989; van Dokkum and Stanford, 2003); so, the relation can be used to estimate the masses of black holes in distant galaxies; and (2) the intrinsic scatter parameter can help constrain theories of black hole formation and galaxy evolution—its magnitude and distribution in mass are key for studying the evolution of the $M_{bh} - \sigma$ relation over cosmic time. It is important to note that emphasis is placed on using black hole masses that were determined dynamically (rather than via reverberation mapping or techniques involving masers) due to the superior resolution of the black hole's dynamical sphere of influence.

1.3 Accretion

The Shakura & Sunyaev standard accretion disk model (Shakura and Sunyaev, 1973) is one of the seminal theoretical/modeling papers on the basic physics of accretion. They demonstrate that the angular momentum of the accreting material being transported outward from the center of accretion causes the infalling matter to form a disk surrounding the black hole. The transport mechanism is some kind of turbulent viscosity that is poorly understood and parametrized by $\nu = \alpha c_s H$, where ν is viscosity, c_s is the speed of sound in the medium, H is the disk height, and α is the free parameter representing our ignorance; it varies between the values zero (meaning no accretion) and approximately one. The assumptions made include hydrostatic equilibrium, conservation of angular momentum, a geometrically thin disk, and constant α for a given accretion disk. Typical values for outbursting dwarf novae are $\alpha = 0.02 - 0.1$ (Lasota, 2001).

The radiation spectrum and the structure of the disk itself depend on the rate $\dot{M}$ at which matter is supplied to the disk. The structure of the disk depends fundamentally on the accretion rate. (See Fig. 1.2.) Panel (a) is the high accretion case $\dot{M} =$ Eddington and panel (b) is the low accretion case. Compared to case (b), case (a) has a much thicker disk that is also more flared at large distances from the black hole. It also has a larger radial size. The disk in case (a) also has a much larger extended hot corona due to the much higher incident flux of ionizing radiation from the center. The above differences in the hot extended coronae lead to predicted differences in the

emergent disk spectra, as shown in Fig. 1.3. For example, for $\dot{M} \gtrsim 10^{-9} M_{\odot}$ yr^{-1}, then the disk will be an intense source of X-rays in the $\sim 1 - 10$ keV energy range, with $L_X \gtrsim 10^{37}$ ergs s^{-1} and the expected optical luminosity will be of order $\sim 1\ L_{\odot}$. An updated model of the effects of X-ray irradiation on the disk shape by Dubus et al. contradicts the assumption of a concave disk. Rather, a self-consistent disk model will produce a convex disk (see Figs. 6 and 7 in Dubus et al., 1999).

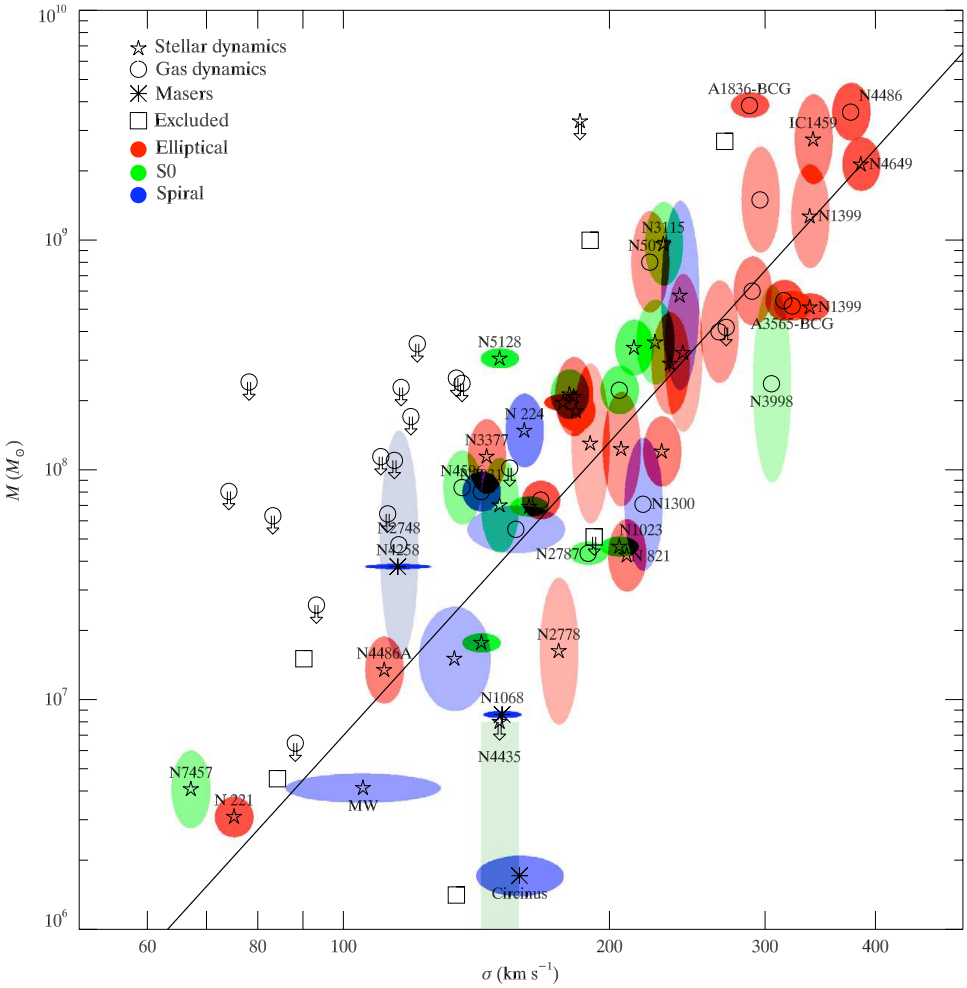

Figure 1.1: "[The] $M - \sigma$ relation for galaxies with dynamical measurements. The symbol indicates the method of BH mass measurement: stellar dynamical (pentagrams), gas dynamical (circles), masers (asterisks). Arrows indicate $3\sigma_{68}$ upper limits to BH mass. If the $3\sigma_{68}$ limit is not available, we plot it at three times the $1\sigma_{68}$ or at 1.5 times the $2\sigma_{68}$ limits. For clarity, we only plot error boxes for upper limits that are close to or below the best-fit relation. The color of the error ellipse indicates the Hubble type of the host galaxy: elliptical (red), S0 (green), and spiral (blue). The saturation of the colors in the error ellipses or boxes is inversely proportional to the area of the ellipse or box. Squares are galaxies that we do not include in our fit. The line is the best fit relation to the full sample: $M_{BH} = 10^{8.12}\ M_\odot(\sigma/200\ \mathrm{km\ s^{-1}})^{4.24}$. The mass uncertainty for NGC 4258 has been plotted much larger than its actual value so that it will show on this plot. For clarity, we omit labels of some galaxies in crowded regions." (From Gültekin et al., 2009, Fig. 1)

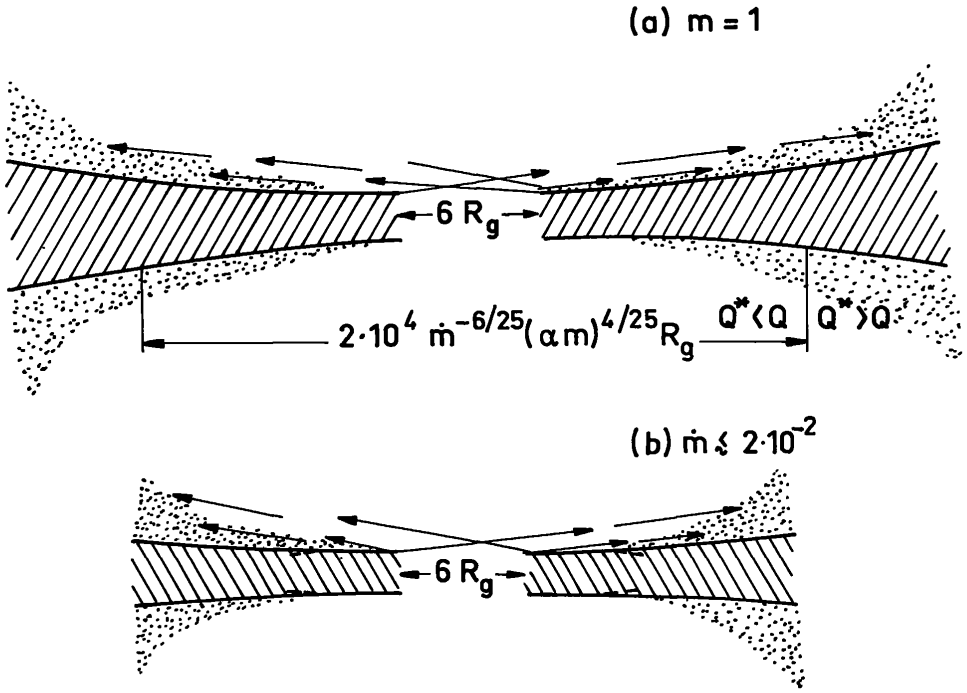

Figure 1.2: Panel (a) is the case of critical accretion which has a much thicker disk that is also more flared at large distances from the BH. (b) is the sub-critical case. The thickness increases with increasing distance from the BH and this effect is more pronounced in (a). Figure courtesy of Shakura & Sunyaev 1973.

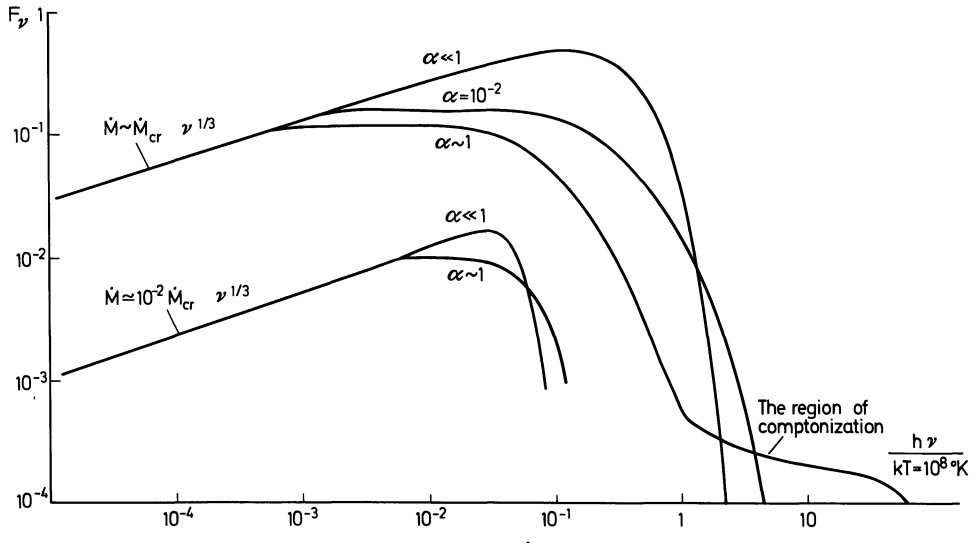

Figure 1.3: An integral spectrum (flux vs. energy) determined from the expression $J_\nu = 2\pi \int F_\nu(R) R\, dR$ for different values of $\dot{M}$ and α. Figure courtesy of Shakura & Sunyaev 1973.

The standard model is invalid when gas pressure is too small (for example, compared with radiation pressure.) In that case, and depending on the physical circumstances, other disk solutions are considered to be a better representation of the conditions in the accretion disk. There are several accretion disk solutions—advection-dominated accretion flows (ADAFs), convection-dominated accretion flows (CDAFs), and hot-settling flows (HSFs) being just three of them (Done et al., 2007). ADAF refers to the situation where the density is low enough for thermalization to break down, causing a hot, geometrically thick, optically thin, two-temperature structure to form in the plasma. Heat energy converted from gravity stays with the radiatively inefficient ions and "advects" onto the black hole. Because radiative energy crosses the event horizon with the ions, advection causes the accretion disk to be less luminous.

This disk supports different temperatures for the protons and electrons, with $T_p \gg T_e$, with the electron temperature $\sim 10^9$ K. CDAFs are similar to ADAFs, but happen because of enhanced viscosity which moves out angular momentum, heat, and matter, impeding accretion on to the black hole. HSFs occur only around rapidly spinning black holes. The magnetic field couples to the spin of the black hole which torques the gas and causes it to shine brighter than it would be otherwise; the enhancement in the luminosity goes as j^4, where j is the spin of the black hole (Medvedev and Murray, 2002). One example of how these accretion flow solutions affect observation is that ADAFs modify the standard disk spectrum and probably arise as the black hole-accretion disk system transitions from state to state based on changes in the rate of accretion. When the accretion rate is low the disk consists of two regions, the inner accretion disk which is dominated by and ADAF and extends down to the event horizon of the black hole, and the outer region that is the standard thin disk. As the accretion rate increases the thin disk extends inward, down to the innermost stable orbit (Esin et al., 1997, and Fig. 1.4).

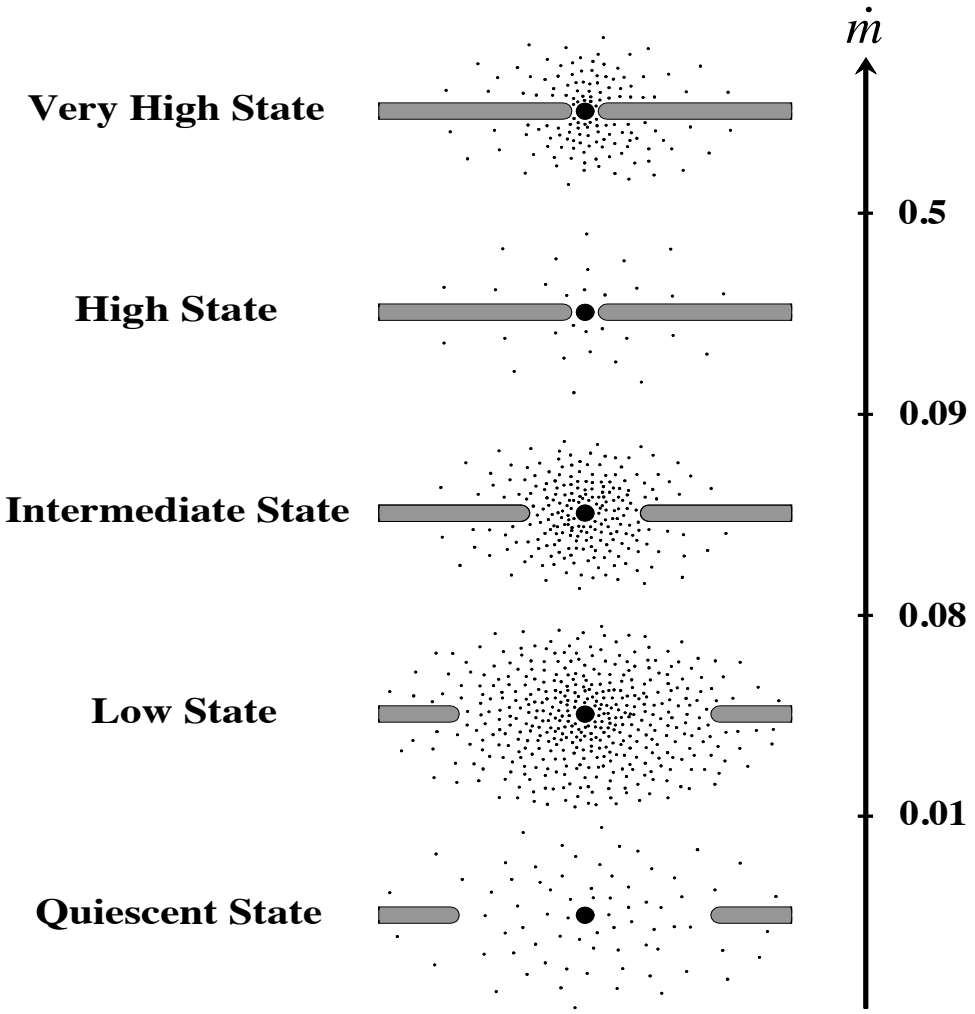

Figure 1.4: Spectral state transitions of the thin disk with ADAFs. When the accretion rate is low the disk consists of two regions, the inner accretion disk which is dominated by and ADAF and extends down to the event horizon of the black hole (represented by the dots), and the outer region that is the standard thin disk (represented by the thin slabs.) As the accretion rate $\dot{m} = \dot{M}/\dot{M}_{Edd}$ increases the thin disk extends inward, down to the innermost stable orbit. Figure courtesy of Esin et al. 1997.

At low mass accretion rates, there is an important hydrogen ionization instability in these disks referred to as the disk instability model (DIM), and represented graphically by an 'S-curve' because of the shape energy vs. disk mass plot as in Figure 1.5.

The left panel illustrates how the instability works. Because the opacity rises steeply in the range near the ionization temperature of hydrogen, the energy of the absorbed photons remains within the disk rather than escaping and allowing the material to cool, causing a rise in the disk temperature. This process continues until nearly all of the hydrogen in the disk is ionized. At that point, there is no longer a large discontinuity in the opacity and the thermal instability triggers a viscous instability in the disk. The increased mass accretion rate at an annulus (due to the increased temperature at that radius) eats away at material at that radius and the pressure drops. Decreasing the pressure decreases the temperature enough for hydrogen to recombine. The thermal instability is again triggered, but this time with run-away cooling until nearly all the hydrogen is neutral. The low temperature leads to a lower accretion rate than input, so the disk is built up again and the cycle repeats. The discontinuities at a particular radius will affect adjacent annuli and therefore will cause the entire disk to exhibit this cycle. This oscillatory behavior has observable consequences, as shown in the right hand panel. The oscillation in $\dot{M}$ (bottom panel) leads to a direct oscillation in the optical luminosity (top two panels). The mass of the disk oscillates due to build up of material from the mass donor until a sufficiently high temperature is reached and the thermal instability is triggered, resulting in an increase mass accretion rate and a drop in disk mass. (Lasota, 2001; Done et al., 2007).

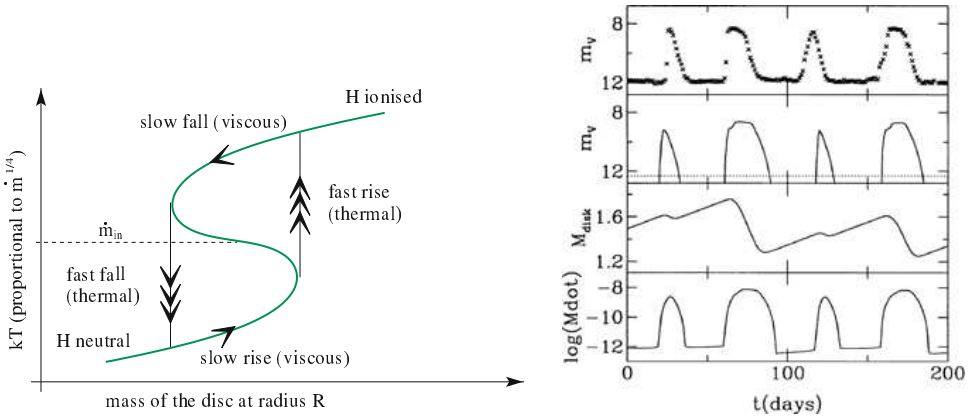

Figure 1.5: Hydrogen ionization instability. *Left*: Illustration of the local effect of the instability. The mass accretion rate through the disk changes abruptly at a given radius. *Right*: Theoretical results of "the effect of the local instability on the global disk structure. The entire disk alternates between outburst and quiescence, matching very well to the observed behavior of dwarf novae such as SS Cyg, as shown in the top panel." (Quoted from Done et al., 2007)

High rates of accretion at small radii produces a similar S-curve caused by a radiation-pressure instability (Fig. 1.6). The rapid increase in heating resulting from a change from gas-pressure dominance to radiation-pressure dominance mean that a small growth in temperature corresponds to a huge growth in pressure. Since the stresses within the disk are assumed to be proportional to the total pressure, there is also an increase in heating of the disk material. Large jumps in temperature that are not balanced by similar changes in opacity means that there will be run-away heating. However, there is not much proof that this radiation instability really exists. The standard Shakura-Sunyaev disk predicts the radiation pressure instability at $\geq 0.06\ L_{Edd}$, yet the spectra of black hole binaries exhibit stable disks up to and beyond $L = 0.7 L_{Edd}$ (Done et al., 2007). This is in contradiction to the standard

disk picture, but alternative descriptions have not necessarily resolved the question of the onset of local instabilities that do not make the whole disk unstable. It is encouraging that in the case of *GRS 1915+105*, which is known to exhibit super-Eddington accretion, it has been shown to undergo a process akin to cyclic behavior as in Figure 1.6. Perhaps only when the accretion rate gets as high as in *GRS 1915+105* is the radiation instability triggered.

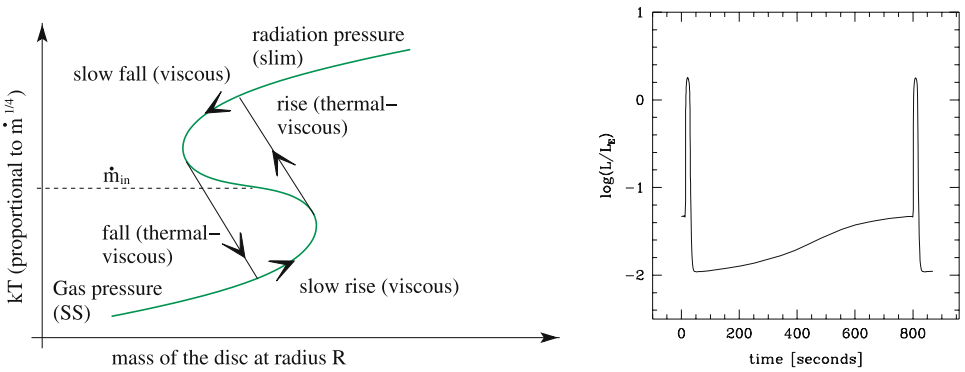

Figure 1.6: Radiation pressure instability. *Left*: The local effect of the instability is illustrated here. "The mass accretion rate through the disk jumps discontinuously at a given radius. *Right*: Theoretical model of the effects of the instability on the global disk structure with the Shakura-Sunyaev viscosity (α=0.1), for L/L$_{Edd}$=0.06. No BHB shows anything like this behavior at this luminosity" (Quoted from Done et al., 2007; Szuszkiewicz and Miller, 2001).

For the extensively studied black hole candidate *Cyg X-1*, the DIM can adequately account for the observed long-term behavior of its light curve; however, the observed spectral behavior is not addressed satisfactorily. The X-ray and γ-ray spectra do not maintain a steady, quasi-thermal shape that would be expected of the standard disk. Figure 1.7 shows the broadband spectrum of *Cyg X-1* for two separate observations, plotted in νF_ν so that the peak of the curves correspond to the characteristic photon energy emitted by the source during the observation. Clearly the two curves represent different spectral states. The one on the left (in red) is typical of a standard, thermally dominant disk with a peak energy below 10 keV, but with an additional non-thermal tail component extending to energies above 500 keV that is not covered in the standard model. This state is also called the "high" or "soft" state. Referred to as the "low" or "hard" state, the curve on the right (in blue) is definitely not the standard disk,

having its peak occur well above 100 keV but also having a low temperature disk component. The potentially confusing nomenclature stems from a gradual increase in our understanding of the spectral states. Early on, these objects were only observed in the $2-10$ keV band, so it seemed natural to distinguish between the spectral states in terms of the observed count rate, which varied by a factor of about 5. This is the origin of the "high" versus "low" distinctions. Later on, an increase in the observed energy range revealed that the bolometric luminosity actually changed by only a small amount. The discovery of hysteresis—the lack of one-to-one correspondence between spectral states and the observed variations in L/L_{Edd} which is believed to arise from the non-stationary character of the accretion flow—in other black hole binaries led to the "soft" versus "hard" distinctions based on the spectral shape rather than the intensity. As more data from transient black hole binaries were obtained and evaluated, it was shown that more spectral states could be observed for cases of high accretion rates. These states have shapes similar to that of the soft state, having peaks on the νF_ν plot below 10 keV, but with very strong high-energy component that is steeper than in either the hard or soft states. This state is referred to as the "very-high" or "steep power-law dominant" state. Another state was discovered having a strong disk-like emission with a strong but steep power law component. It was named the "intermediate" state, but is now thought by many to be roughly the same as the "very high" state. Figure 1.8 displays examples of these states. Note that the "ultrasoft" state denotes an extreme form of the soft state in which the tail

emission is very weak.

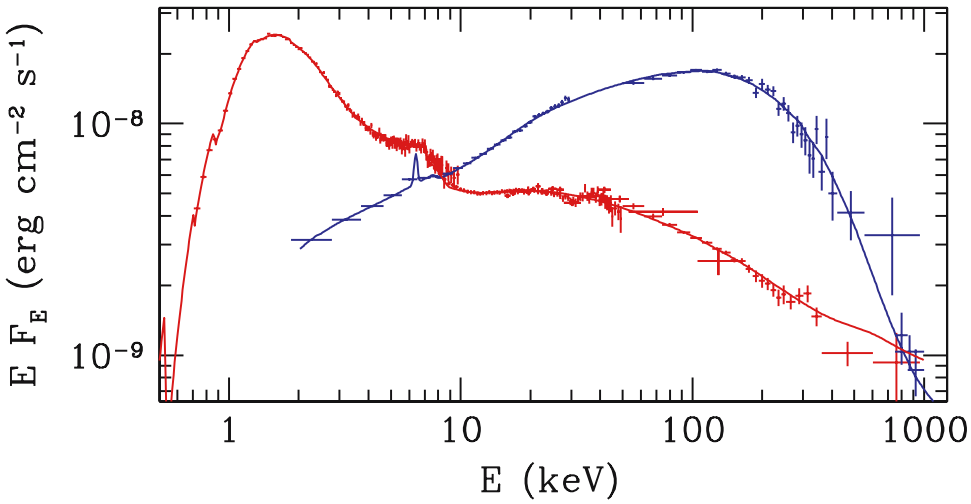

Figure 1.7: X-ray and γ-ray data from *Cyg X-1* . *Red*: The high/soft state in which the peak is less than 10 keV and the emission is from a thermally dominant disc with a nonthermal tail component. *Blue*: The low/hard state in which the peak is above 100 keV and the emission is dominated by non-thermal photons. Figure courtesy of Done et al. 2007

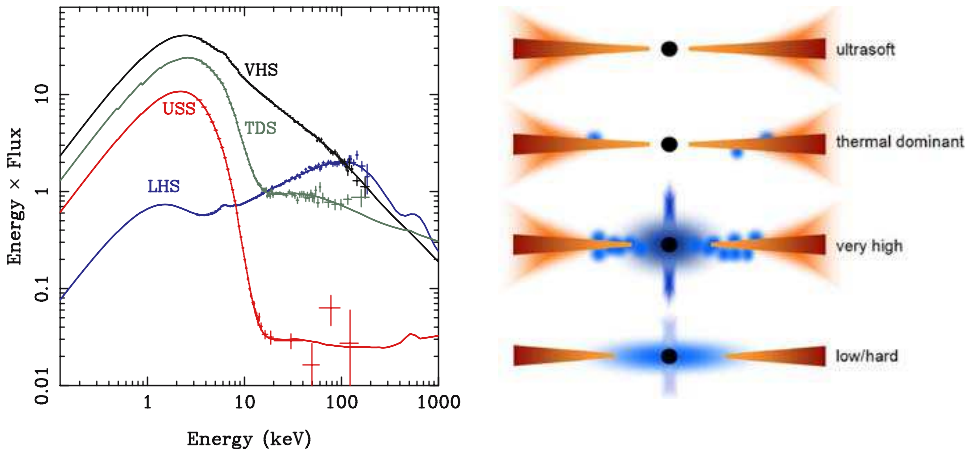

Figure 1.8: BH spectral states of GRO J1655-40. *Left*: A selection of spectra taken from a 2005 outburst. *Right*: Proposed accretion flows that may explain the differences. Components from the disk, hot inner flow, active regions above the disk, and winds all contribute to the observed spectra (Done et al., 2007).

Truncated disk spectra are produced by a combination of two stable accretion flow structures in a single disk. The inner hot, optically thin, geometrically thick flow (present only at low luminosities) exists along side the outer cool, optically thick, geometrically thin flow. The radius at which the disk transitions between the two structures is called the "truncation radius." This disk is usually invoked to explain the contrasting hard and soft spectra in X-ray binaries. Decreasing the truncation radius produces softer spectra, higher frequencies in the disk power spectrum, and higher velocity outflows ("which are invoked to explain the dramatic radio flares seen in the hard-to-soft [but NOT the soft-to-hard] transitions"; Done 2007). In the case of black hole binaries the hot inner accretion flow breaks down at the radius of the innermost stable circular orbit, triggering a substantial reduction in the radio flux while feeding material into a polar jet. This might be the origin of the hard/soft

transition in black hole binaries. Neutron stars follow the same model, with an added component due to their surface. The lack of a surface component in the black hole case implies the presence of an event horizon, and is therefore taken as confirmation that they are indeed black holes. (See Fig. 1.9)

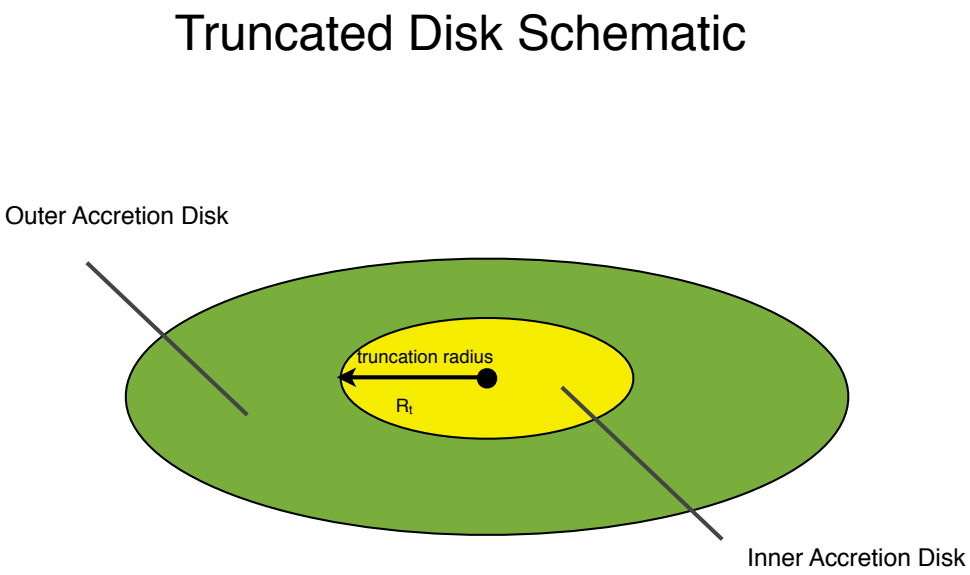

Figure 1.9: Cartoon of the truncated disk. Truncated disk spectra are produced by a combination of two stable accretion flow structures in a single disk. At low luminosities, the inner hot, optically thin, geometrically thick flow exists along side the outer cool, optically thick, geometrically thin flow. The radius at which the disk transitions between the two structures is called the "truncation radius."

Super-Eddington luminosities can reduce the effective gravitational force, leading to more powerful winds emanating from closer to the black hole. Such winds could alter the structure of the accretion disk, but not to the extent that the luminosity falls below the Eddington limit. There are a few Galactic black hole binaries and accreting neutron stars that have been observed with super-Eddington luminosities, including *V404 Cyg*, *GRS 1915+105*, and *SS 433*. According to the DIM, the peak luminosity is proportional to the size of the disk in which the wind is born. Based on this and the trend displayed in the several super-Eddington galactic sources, we can conclude that only systems with comparatively large orbital periods are capable of exceeding the Eddington luminosity since their accretion disks are sufficiently large.

1.4 Observations

One of the first black hole candidates to be identified is *Cyg X-1*, whose companion star *HD 226868* was observed to have an orbital period of 5.6 days with velocity amplitude of about 64 km s^{-1} (the velocity amplitude was refined in later work to be 75 km s^{-1}) (Webster and Murdin, 1972; Casares, 2007). Variations in the radial velocity and known constraints on the maximum mass of neutron stars suggest that the compact component of *Cyg X-1* is a stellar-mass black hole candidate. Using the mass function $f(M_x)$, which marks the lower limit of the X-ray emitting compact object mass M_x, we can relate two observable quantities, the velocity K_n of the mass donor and orbital period P to the masses of X-ray emitting compact object M_x and the mass donor M_n of the binary

$$f(M_x) = \frac{PK_n^3}{2\pi G} = \frac{M_x^3 \sin^3 i}{(M_x + M_n)^2},$$

where $K_n = 2\pi a_n \sin i/P$. For the case of *Cyg X-1*, $f(M_x) = PK_n^3/2\pi G = 0.25M_\odot$. A conservative estimate of the inclination based on the lack of X-ray eclipses in the observed light curve is $i = 60°$. Initially thought to be an early B star, it is likely that the companion is an undermassive (because of mass transfer and binary evolution) O star conservatively estimated to be of a typical companion mass at $M_n \sim 15M_\odot$. This yields a lower limit for the compact object of $M_x \gtrsim 4M_\odot$ (Casares, 2007). This is greater than the currently accepted theoretical estimate of the maximum neutron star mass of $\approx 3.0 - 3.2M_\odot$.

The observations of *Cyg X-1* did not quell the debate over the existence of black holes. Subsequent to the detection of *Cyg X-1*, there have been other observations of black hole candidates with masses near the threshold neutron star mass, including the high mass X-ray binary (HMXB) *LMC X-3*, and the X-ray transient *A0620-00*. However, there were many proposals put forward to explain these observations without invoking the presence of black holes. These hypotheses included, but were not limited to, unusual forms of the equation of state for neutron stars and triple star systems. At this point, the search was on for systems with mass functions clearly above 5 $M_{\odot}$ which would imply more forcefully the presence of a black hole. The discovery of the X-ray transient *V404 Cyg* went a long way to settling the question. Analysis of spectroscopic data collected during quiescent periods confirmed the presence of a K0 companion with a velocity amplitude of 211 km s^{-1} and an orbital period of about 6.5 days. From these values the mass function is computed to be 6.3 ± 0.3 $M_{\odot}$. This immediately implies a compact object mass of at least 6 $M_{\odot}$, *without having to make any assumptions for the inclination or the mass of the companion* (Casares et al., 1992), moving black holes out of the realm of mere mathematical speculation and placing them firmly within modern observational astrophysics. Since this discovery, there have been many confirmed black holes based on dynamical measurements (see Casares, 2007, Table 1).

1.4.1 Ultraluminous X-ray Sources

The nature of the ultra-luminous X-ray sources (ULXs) discovered by *Einstein* and *ROSAT* surveys of nearby galaxies remains highly controversial. ULXs are point-like, non-nuclear X-ray sources characterized by extremely high X-ray luminosities $L_X \sim 10^{39} - 10^{41}$ erg s^{-1}. The Eddington luminosity for a ~ 20 M$_\odot$ black hole is $L_E = 4\pi c G m_p M_{BH}/\sigma_T \approx 3 \times 10^{39}$ erg s^{-1}. Most are binary stellar systems with one normal and one compact component, which we believe to be a black hole. Based purely on the observed, and well established (given the accurately known distances) high luminosities it is believed that ULXs may harbor the long-sought intermediate-mass black holes (IMBHs). If IMBHs exist, they would be in the mass range $10^2 - 10^4$ M$_\odot$, which is light enough not to plunge to the centers of their host galaxies, but massive enough to emit radiation as bright as the observed luminosities of ULXs. Making the reasonable assumptions that ULXs emit radiation isotropically and that the Eddington limit is valid, one can naturally conclude that ULXs are powered by IMBHs. Corroborating evidence that they are IMBHs arises from central mass estimates based on the observed X-ray spectral energy distribution. The ULXs occupy a distinct region of the luminosity-temperature diagram (see Fig. 1.10). The fact that ULXs are much brighter than the stellar-mass black holes and yet have cooler disks suggests that they might contain IMBHs. X-ray spectral fits with multi-color disk blackbody models yield black hole masses in the $M_{BH} \sim 10^{3-4}\ M_\odot$ range, although the applicability of these models remains a controversial topic since they do not fully

describe the observations.

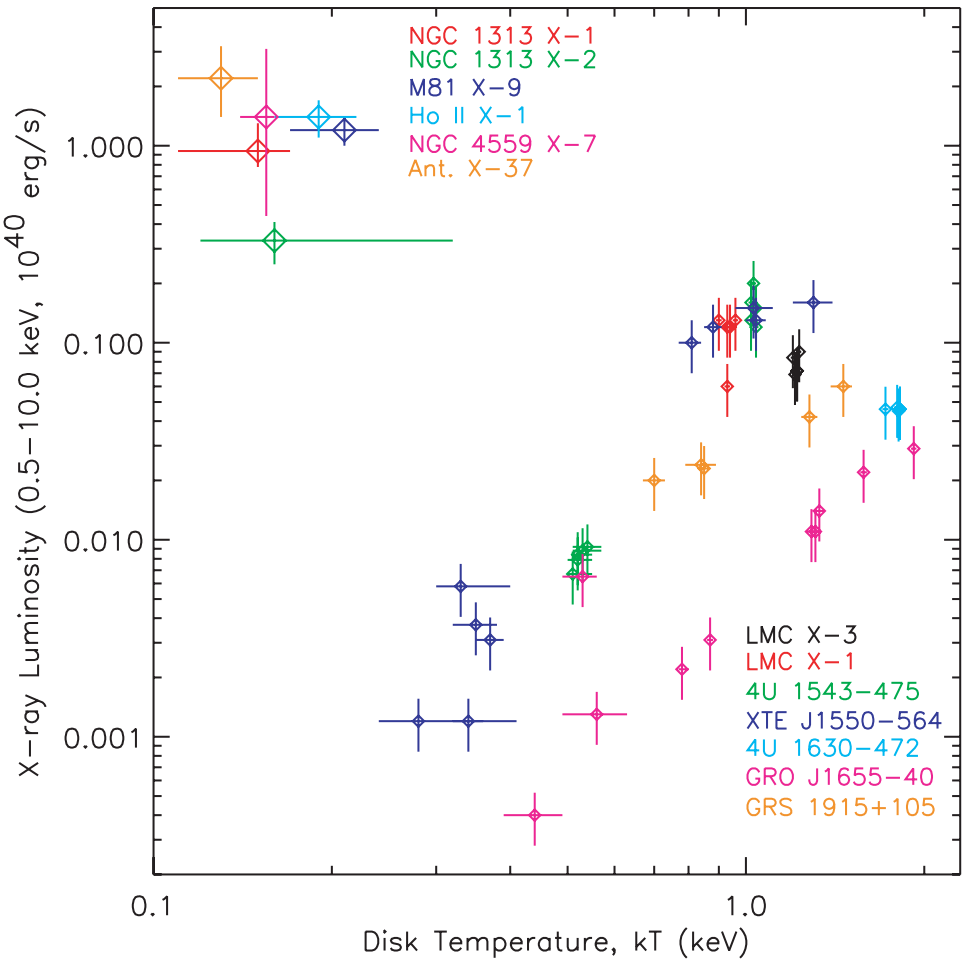

Figure 1.10: Luminosity vs. Temperature for ULXs (upper left data points) and Galactic black holes. ULXs occupy a distinct region of the luminosity-temperature diagram and are well fitted with multi-color disk (MCD) models. The fact that ULXs are much brighter than the stellar-mass black holes and yet have cooler disks suggests they might contain IMBHs. The Galactic black hole disk temperatures approximate those of ULXs only at luminosities that are at least 2 orders of magnitude below the ULX luminosities. From Miller et al. 2004.

Super-Eddington luminosities are inferred for ULXs from relatively precisely known galactic distances and suggest that ULXs may harbor the long-sought intermediate-mass black holes (IMBHs). Corroborating evidence that they are IMBHs arises from central mass estimates based on the observed X-ray spectral energy distribution; X-

ray spectral fits with multi-color disk blackbody models yield black hole masses in the $M_{BH} \sim 10^{3-4}\ M_{\odot}$ range, but these are not dynamically measured masses. Also, these fits hinge on the noisiest part of the X-ray spectral data. In fact, the peak temperature of the inferred accretion disk is so low that it lies outside the observed energy range and requires arbitrarily high values for the absorbing hydrogen column density. Detailed imaging and spectral analysis of ULX IMBH candidates find that they can be satisfactorily fit by models that do not require ultra-low temperature accretion discs, such as coronal accretion models. ULXs may instead be powered by an extreme form of "conventional" stellar-mass black holes (BHs), in which the observed disk temperatures due to dissipation of the energy in the inner accretion disk by an optically thick corona that obscures the disk somewhat (Gladstone et al., 2009).

1.4.2 Fundamental Plane of Black Hole Activity

A fundamental plane of black hole activity can be formed by studying the correlation between the radio luminosity and both the X-ray luminosity and mass of the black hole (Merloni et al., 2003, 2005). The correlations present an alternative unification scheme to the one based on orientation (Urry and Padovani, 1995). The fundamental plane unifies black holes through a very small number of parameters, the most important of which are the black hole mass and accretion rate. However, the fundamental plane correlation is not as tight as that of the $M_{bh} - \sigma$ relation. "A correlation between X-ray and radio emission is expected if there is a fundamental

connection between accretion flows and jet activity. Thus, at a qualitative level, the existence of the Fundamental Plane . . . is not surprising. However, on a quantitative level, the presence of such a plane and the measurement of the correlation coefficients associated with it provide powerful probes of accretion physics and of the inner jet." (Quoted from Merloni et al., 2003, section 5)

The changes in the shape of the intrinsically narrow Kα emission line of iron are due to the relativistic Doppler and gravitational effects of the black hole (Tanaka et al., 1995; Fabian and Iwasawa, 2000; Reynolds and Nowak, 2003). This emission line has a rest frame energy of 6.4 keV. It is produced as a result of the iron atoms in the inner accretion disk absorbing hard X-rays, then generating fluorescent radiation when the excited iron electrons transition from the L-shell down to the innermost K-shell and re-emit X-rays, but at the characteristic line energy of 6.4 keV. However, the observed line profile has a distorted shape because of gas motions in the strong gravity field of the black hole (e.g. Fabian and Iwasawa, 2000). This is important because we can use the shape distortion to measure the orbital motion of the atoms emitting the radiation, and thereby measure properties of the black hole and its environment, including the mass and spin of the black hole itself. For example, in a recent statistically robust study of black hole spin distribution in AGN, spectroscopic analysis of *MCG-6-30-15* show that its spin is nearly 99% of the theoretical maximum (Brenneman, 2007). Estimates of the spin in the case of microquasars in our Galaxy have ranged from $10-80\%$ of the theoretical maximum (Middleton et al., 2006). The

orbital velocity of matter in the disk causes broadening of the line, and variations due to special relativistic effects means that the 'blue side is brighter than the 'red' one. The transverse Doppler effect and gravitational redshift then reddens the emission. The net result is a broad, skewed, emission line similar to that observed in Figure 1.11.

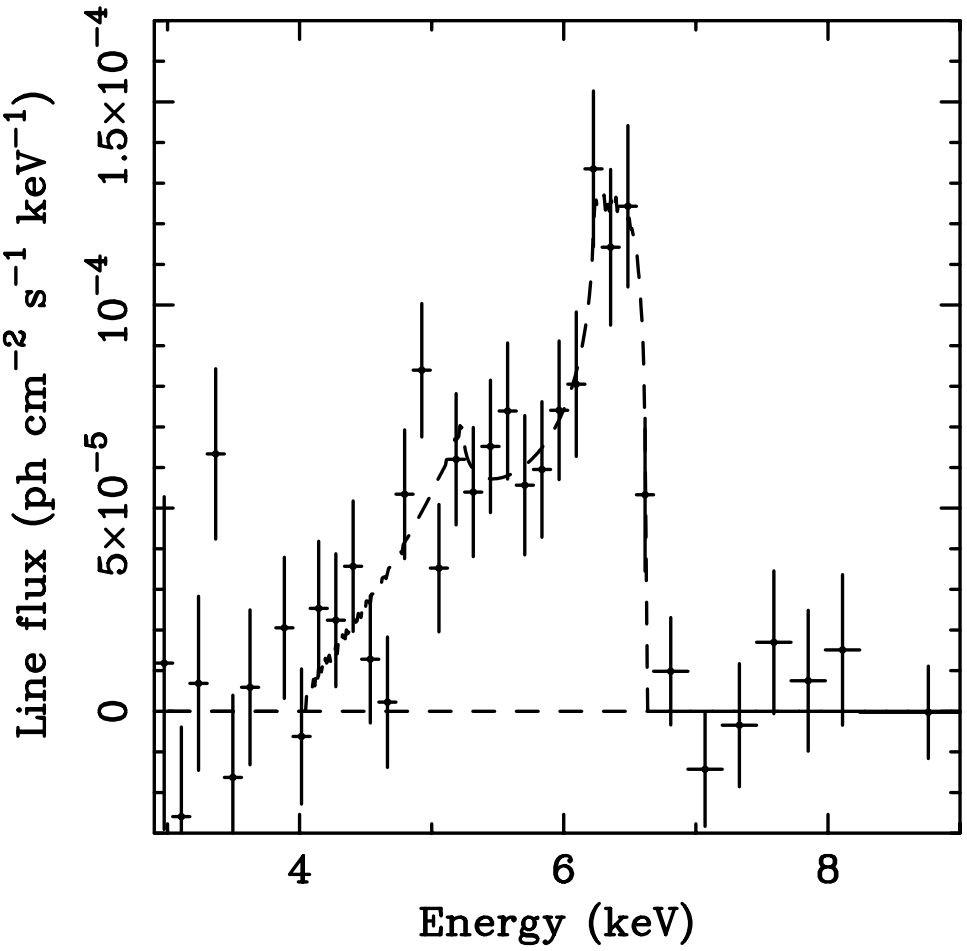

Figure 1.11: Continuum subtracted iron line from the long July-1994 *ASCA* observation of the Seyfert-1 galaxy *MCG6-30-15*. The changes in the shape of the intrinsically narrow K-α emission line of iron is due to the relativistic Doppler and gravitational effects of the black hole. Figure from Tanaka et al., 1995

1.5 Executive Summary

This thesis focuses on the very-long-term (weeks to years) timing properties of high mass X-ray binaries (HMXBs), including the so-called ultraluminous X-ray sources (ULXs).

In Chapter II, I explore the astrophysical implications of super-orbital periods in X-ray binaries (XRBs), which could be linked to the coupled precession of their accretion disks and relativistic jets. These modulations arise in environments that feature super-Eddington mass transfer onto central black holes, inviting comparisons with the archetype microquasar SS433. I studied the ULX NGC 5408 X-1 to see if its behavior could be better explained as a hyper-accreting HMXB with a stellar-mass black hole, rather than by the alternate interpretation of an accreting IMBH. We found that in the case of NGC 5408 X-1, a stellar-mass black hole could not be ruled out as the properties of this ULX could be accounted for without invoking IMBHs.

In Chapter III, I outline a pilot study measuring the very-long-term variability of X-ray sources in the nearby galaxies, which require multi-epoch X-ray observations. Using all the available data from the *Chandra X-ray Obseratory*, the nearby galaxy M87 was searched for X-ray sources exhibiting strong, very-long-term variability. Measuring super-orbital periods is difficult, especially for extragalactic sources, and this thesis work highlights the need for long-term monitoring campaign with a good sampling plan.

In Chapters IV and V, I present a spectroscopic analysis of a recently discovered HMXB found in the Large Magellanic Cloud (LMC) and within a supernova remnant (SNR). Its nebular environment invites comparisons to both SS433 and NGC 5408 X-1 (Chapter II). The nature of the compact object in this particular HMXB remains unresolved; however, its bright optical counterpart and its X-ray variability points to

an accretion-powered compact binary. I present an analysis of the variations in the Doppler shift of the lines in its optical spectra. The best explanation for the observed X-ray luminosity and optical properties is a HMXB with a black hole or neutron star primary component undergoing wind accretion from a massive early-type donor. The orbital period is weeks, and the optical companion is likely the earliest found in a HMXB, making it a highly unusual system.

Chapter VI highlights works in progress and future research projects enabled by this thesis work.

Chapter II

INTERPRETATION OF THE 115 DAY PERIODIC MODULATION IN THE X-RAY FLUX OF NGC 5408 X-1

(Published as: Foster et al. 2010)

We comment on the recent observation of a 115-day modulation in the X-ray flux of the ultraluminous X-ray source (ULX) NGC 5408 X-1, and in particular, the interpretation of this modulation as the orbital period. We suggest that this modulation may instead be due to a precessing jet, and is thus *superorbital* in nature. Comparing the properties of this ULX with those of the prototypical micro-quasar SS 433, we argue that NGC 5408 X-1 is very similar to SS 433: a hyper-accreting stellar-mass black hole in a shorter-period binary. If the analogy holds, the 115-day modulation is best explained by the still poorly-understood physics of inner-disc/jet precession and a longer observing baseline would be able to reveal an intrinsic phase jitter that is associated with such a precession.

2.1 Background

The nature of ultra-luminous X-ray sources (ULXs) discovered by *Chandra* and *XMM-Newton* surveys of nearby galaxies remains highly controversial (e.g. Fabbiano and White, 2006; Zampieri and Roberts, 2009). ULXs appear as point-like, non-nuclear X-ray sources characterised by extremely high X-ray luminosities ($L_X \gtrsim 10^{39}$

erg s^{-1}) compared to *Galactic* X-ray binaries (XRBs) (Long et al., 1981a; Fabbiano, 1989; Makishima et al., 2000; Fabbiano et al., 2001; Colbert et al., 2004).

Making seemingly reasonable assumptions that ULXs emit radiation isotropically and that they are Eddington limited, one might naturally conclude that ULXs harbour the long-sought intermediate-mass black holes (IMBHs) whose masses are $\sim 10^{2-4}$ $M_\odot$ (Miller and Colbert, 2004; Miller, 2005; Fabbiano and White, 2006). If IMBHs exist, they would be too light to plunge to the centres of their host galaxies via dynamical friction, but would be massive enough to power ULX luminosities.

NGC 5408 X-1 is one of the brightest ULXs, with a well-determined X-ray luminosity of $L_X \approx 2 \times 10^{40}$erg s^{-1} in the 0.3–10 keV band (Strohmayer, 2009). Presently, this source is one of the best IMBH candidates, with mass estimates well in excess of 100 $M_\odot$, but possibly up to 9000 $M_\odot$ (Kaaret et al., 2003; Strohmayer et al., 2007; Strohmayer, 2009; Strohmayer and Mushotzky, 2009). Such large range of uncertainty in the mass must surely be a cause for concern. This is particularly true given that a number of studies have suggested that ULXs may merely be stellar-mass black hole binaries (BHBs) that exhibit super-Eddington accretion which can be achieved via beaming of the emission, super-critical mass accretion, or a combination of both (Begelman et al., 2006; King, 2008a,b, 2009).

As a prime example of the difficulty in using the X-ray luminosity to pin down the black hole mass, consider the case of SS 433, a remarkable Galactic X-ray source and the prototypical micro-quasar (see Margon, 1984). SS 433 very likely contains a

total mass $\sim$ 40 $M_\odot$, with a $\sim$ 4 $M_\odot$ black hole as the compact accretor (Blundell et al., 2008; Kubota et al., 2010), and with the bulk of its energy output mechanically beamed (e.g. Begelman et al., 2006). Indeed, supporting evidence for the stellar-mass black hole scenario lies in the relativistic jets which precess with a 162-day period about the binary orbital axis. In addition, there are well-studied massive outflows due to hyper-Eddington mass transfer (Fabrika, 2004; Begelman et al., 2006; Blundell et al., 2008). The jet itself has a kinetic luminosity $\gtrsim 10^{39}$ erg s^{-1}, which exceeds the observed L_X by a factor of $\sim 10^3$. However, its high orbital inclination obscures the intrinsic X-ray brightness from direct view. All of this together suggests that if viewed externally and at lower inclination, SS 433 would be bright enough to appear as a ULX (Fabrika and Mescheryakov, 2001). Under these circumstances it would be miscategorised as an IMBH (Begelman et al., 2006).

Model-independent system mass estimates are possible in Galactic X-ray binaries based on their kinematics (Charles and Coe, 2006). In the case of SS 433, the mass of the X-ray emitting accretor plus the accretion disc is $\approx 16 M_\odot$ (Blundell et al., 2008). However, such system mass estimates have not yet been possible for any extragalactic ULX.

Recently, a case for an IMBH in NGC 5408 X-1 has been made, citing its principal observed property of an extremely high L_X and the presence of a low-frequency quasi-periodic oscillation (QPO). The X-ray luminosity alone implies a black hole mass of $\sim$ 100 $M_\odot$ if we assume that the ULX is radiating at the Eddington limit. Adding weight

to the interpretation that this source is an extreme form of high mass X-ray binary, there is a recent discovery of a 115-day modulation in the X-ray flux. Strohmayer (2009) interpreted this modulation as the binary orbital period for a system with a ~ 1000 $M_{\odot}$ black hole for the primary component and a 3–5 $M_{\odot}$ giant or supergiant star for the secondary component.

In examining the properties of NGC 5408 X-1, we suggest here that it may be instructive to make further comparisons with SS 433. Both sources are known to be engulfed in photo-ionised, steep-spectrum radio nebulae of similar size (Margon, 1984; Soria et al., 2006; Lang et al., 2007; Poutanen et al., 2007; Kaaret and Corbel, 2009), strongly favouring the presence of optically-thin synchrotron emission powered by an accreting black hole over X-ray emission from a supernova remnant (SNR). And both may have formed from HMXBs undergoing mass transfer on a thermal time-scale (King et al., 2000). This raises the question of whether NGC 5408 X-1 may be more similar to SS 433 than previously realised. There now exists an extensive observational database for SS 433, particularly for its precessing jets (Eikenberry et al., 2001), and we investigate here whether its properties are sufficiently similar to those of NGC 5408 X-1 to consider them both part of the same population.

2.2 Comparing NGC 5408 X-1 and SS 433

2.2.1 Properties of NGC 5408 X-1

NGC 5408 is a dwarf irregular galaxy at a distance of 4.8 Mpc (Karachentsev et al., 2002). Kaaret et al. (2003) discovered radio emission at the position of the ULX NGC 5408 X-1, and they found that the X-ray, optical, and radio fluxes were consistent with beamed emission from a relativistic jet of an accreting stellar-mass black hole (although they could not rule out jet emission from an IMBH.) However, subsequent radio observations (Lang et al., 2007) showed that, in fact, the radio emission was too extended ($1\farcs5 - 2\farcs0$, or $R \approx 35 - 46$ pc) to be associated with relativistic jets and was more likely optically thin synchrotron emission from a surrounding nebula.

Because the ULX is located in a relatively unobscured and uncrowded region, its optical counterpart has been identified (Kaaret and Corbel, 2009). It has been shown that NGC 5408 X-1 is confined within a photo-ionised nebula (of size $R \sim 30$ pc) displaying strong high-excitation emission lines of He II λ4686 and [Ne V] λ3426. The optical continuum emission of the counterpart was weak and there were no absorption features present that might be associated with the donor's photosphere, thereby precluding a kinematic study (cf. Prestwich et al. 2007 in the case of IC 10 X-1; Kaaret and Corbel, 2009).

A potentially crucial feature of this ULX is the presence of a low frequency ($\simeq$ 10 mHz) quasi-periodic oscillation (QPO) in the soft X-ray band (Strohmayer et al., 2007; Strohmayer, 2009). The physical origin of such QPOs remains controversial

(Poutanen et al., 2007). However, QPO phenomenology has been studied over the last decade, and it is commonly assumed that the black hole mass is inversely proportional to the QPO frequency at a given value of the power-law spectral index (Titarchuk et al., 1998; Titarchuk and Fiorito, 2004; Shaposhnikov and Titarchuk, 2009). Given this assumption, the observed QPO frequency suggests a black hole mass well in excess of 1000 $M_{\odot}$, possibly as high as 9000 $M_{\odot}$ (Strohmayer and Mushotzky, 2009). If these properties were confirmed, then NGC 5408 X-1 would indeed be a remarkable and extremely important object for black hole population studies.

2.2.2 Properties of SS 433

A twenty-year baseline of many optical photometric and spectroscopic campaigns has revealed multiple periodicities in SS 433: a well- established orbital period of $P_{\rm orb} = 13.07$ d (Crampton et al., 1980), a precessional period $P_{\rm prec} = 162.375$ d (Eikenberry et al., 2001), and a nutation period $P_{\rm nu} = 6.3$ d (Mazeh et al., 1980; Katz et al., 1982) due to a periodic torque produced by the secondary component which does not affect the mean precession rate but does produce an instantaneous oscillation in the precession with a period of about one-half the orbital period (Katz et al., 1982; Bate et al., 2000).

SS 433 has an observed X-ray luminosity of $L \sim 10^{36}$ erg s^{-1}, but as an eclipsing binary, it has a high inclination and fits the description of a classic *accretion disc corona* (ADC) source (Watson et al., 1986; Frank et al., 1987); the obscuration by

Table II.1. Comparing QPO frequency, P_{sup}, and M_X in BHBs

Source	P_{sup} (day)	f_{QPO} (Hz)	M_X ($M_\odot$)
NGC 5408 X-1	115.5 ± 4[a]	0.010[a]	—
SS 433	162.375 ± 0.011[b]	0.100[c]	4.3 ± 0.6[d]
GRS 1915+105	590 ± 40[e]	0.001–67[f]	14 ± 4[g]
GRO J1655-40	$\simeq 3$[i]	0.1–450[j,k,m]	6.3 ± 0.5[n]
Cygnus X-1	$\simeq 300$[p]	0.040–0.070[q]	21 ± 8[p]

[a]Strohmayer (2009)

[b]Eikenberry et al. (2001)

[c]Kotani et al. (2006)

[d]Kubota et al. (2010)

[e]Rau, Greiner, and McCollough (2003)

[f]Morgan, Remillard, and Greiner (1997)

[g]Greiner et al. (2001)

[i]Hjellming and Rupen (1995)

[j]Remillard et al. (1999)

[k]Strohmayer (2001)

[m]Remillard et al. (2002)

[n]Greene et al. (2001)

[p]Rico (2008)

[q]Vikhlinin et al. (1994)

the disc implies that the intrinsic $L_{\rm X}$ is a factor 10^{2-3} higher. The observed kinetic luminosity in the jets is in the range $L_k \sim 10^{39-41}$ erg s^{-1} (Margon, 1984; Fabrika, 2004). As pointed out in King (2008a), this kinetic luminosity is already larger (possibly very much so) than the Eddington luminosity for a ~ 10 M$_\odot$ black hole. The mass ejection rate from the jets is $\dot{M}_{\rm jets} \gtrsim 5 \times 10^{-7} M_\odot$ yr^{-1} (Begelman et al., 2006).

SS 433 is located at the centre of the supernova remnant W50 whose size is $\approx 1.5^\circ$ across its largest dimension, corresponding to ≈ 64 pc at its distance of 5.5 kpc (Margon, 1984). It is worth noting that this is comparable in extent to that of the NGC 5408 X-1 optical nebula. W50 has long been known to exhibit "ears" that align with the SS 433 jets, perhaps caused by the strong outflowing wind velocity of ≈ 1500 km s^{-1} (Fabrika, 2004). These winds may be driven by hyper-Eddington accretion onto the black hole at $\approx 5000 \dot{M}_{\rm Edd}$ (Begelman et al. 2006; see also Fig. 9 of Shakura & Sunyaev 1973). Such a hyper-accreting object will generate a mechanically beamed accretion luminosity (Begelman et al., 2006; King, 2008b). Consequently, most of the light is geometrically collimated into a cone along the outflow axis with a solid angle Ω that cannot be estimated *a priori*, since its inverse determines the apparent luminosity. For consistency with the number of progenitor high mass X-ray binaries in the Milky Way, it is assumed that $\Omega/4\pi \gtrsim 0.1$ for SS 433 (Begelman et al., 2006; Fabrika and Abolmasov, 2007; Poutanen et al., 2007; King, 2008b,a, 2009).

2.3 The nature of the 115-day periodic modulation in NGC 5408 X-1

A $115\overset{d}{.}5$ modulation was detected in the X-ray flux of NGC 5408 X-1 with the *Swift*/X-ray Telescope and was interpreted as being orbital in origin (Strohmayer, 2009). Since the stability of this modulation has not yet been established, this conclusion was largely based on the assertion that 115 days is shorter than all other known superorbital periods for stellar mass BHBs in the Galaxy. However, it is not substantially less than the well-established superorbital precession period for SS 433.

In fact, the question of whether there is significant overlap in the orbital timescales of black holes and neutron stars remains unanswered to date. Superorbital periods in neutron stars are known to range from tens to hundreds of days (Wen et al., 2006; Charles et al., 2008)—in some cases even longer than the 115 days in NGC 5408 X-1 (Charles et al., 2008; Kotze and Charles, 2010). Taking into account that there are considerably more known neutron star binaries than BHBs, that there are a comparatively small number of known, persistently bright black hole candidates, and that there are *several* mechanisms to explain these periodicities (i.e. the Kozai mechanism, radiation-driven disc warping, etc.; Kozai, 1962; Maloney et al., 1996, 1998), the need for a comprehensive statistical analysis of the orbital timescales in neutron stars and black holes is apparent.

So far, the modulation period in NGC 5408 X-1 has only been determined to $\pm$ 4 days as a result of the small number of cycles sampled. We note that if the 115 d modulation is orbital, then longer observing baselines will define this more and

more precisely, whereas a superorbital modulation (such as for SS 433) will suffer an intrinsic phase jitter. At this time, the observations cannot distinguish between the two interpretations and we propose here that the modulation is instead superorbital in origin and hence similar to SS 433.

2.4 Discussion

2.4.1 Mass estimates from QPOs

For Galactic BHBs with high Eddington ratios ($L/L_{\rm Edd}$), there exist kinematic data that constrain their masses to be $\sim$ 10–15 $M_\odot$ (e.g. GRS 1915+105, Greiner et al., 2001). However, for ULXs there is no such dynamical information due to their extreme optical faintness and lack of direct detection of the donor. Therefore, we must use indirect methods.

Under the assumption that they are signatures of Keplerian orbits of the material in the inner accretion flow, low-frequency QPOs have been used to infer the masses of the primary components of BHBs. This line of enquiry seems promising in light of more recent work (Shaposhnikov and Titarchuk, 2009), although the techniques involved have thus far only been applied to a small number of stellar-mass black holes ($M_{BH} \sim 5{-}15$ $M_\odot$), so the range of masses sampled is low.

NGC 5408 X-1 is a ULX whose observed properties suggest two different masses for its compact accretor. The $L_{\rm X}$ alone implies a $\sim$ 100 $M_\odot$ black hole if we assume a high Eddington ratio. Yet, this ULX exhibits a low-frequency QPO in its soft

flux, suggesting the presence of an IMBH of mass 2000−5000 $M_\odot$ (Strohmayer and Mushotzky, 2009). However, similar low-frequency oscillations have been observed in Galactic binaries that are well-established *stellar-mass* binary systems (see Table 1). For example, GRS 1915+105 exhibits low-frequency QPOs $\sim 0.001-10$ Hz (Morgan et al., 1997) and Cygnus X-1 has low-frequency QPOs $\sim 0.04-0.07$ Hz (Vikhlinin et al., 1994). Furthermore, the sample of stellar mass BHBs used to determine the scaling relationship (which is based on the range of the best-fitting power-law slopes in their reference sample of sources) for NGC 5408 X-1 in Strohmayer and Mushotzky (2009) uses systems with known stellar-black-hole masses whose observed Eddington fraction is much higher than would be the case for NGC 5408 X-1 if its black hole has a mass of 5000 $M_\odot$ (as predicted in Strohmayer & Mushotzky 2009) and therefore $L_{\rm Edd} \gtrsim 10^{42}$ erg s^{-1}. The observed $L_{\rm X} \approx 2 \times 10^{40}$ erg s^{-1} is only $\sim 2\%$ $L_{\rm Edd}$ and this may not be reasonable given the environment of this ULX and the apparently steady flux level. Therefore, one should exercise caution when using the presence of low-frequency QPOs to infer black-hole masses.

2.4.2 Mass Transfer from the Donor

Two distinct effects of super-Eddington mass transfer can cause the X-ray luminosity to exceed the Eddington limit. First, the disc accretion luminosity has an

additional, logarithmic component due to the inner transition region:

$$L_{\rm acc} \simeq L_{\rm Edd}\left[1+\ln\left(\frac{\dot{\rm M}}{\dot{\rm M}_{\rm Edd}}\right)\right] \tag{2.1}$$

which could enhance the luminosity by as much as 5−10 times $L_{\rm Edd}$ (Poutanen et al., 2007). Secondly, the luminosity is modified by mechanical (i.e. geometrical, non-relativistic) beaming, resulting in collimation by a factor b (typically $\gtrsim 0.1$):

$$L \simeq \frac{L_{\rm Edd}}{b}\left[1+\ln\left(\frac{\dot{\rm M}}{\dot{\rm M}_{\rm Edd}}\right)\right] \tag{2.2}$$

(King, 2002; Rappaport et al., 2005; Poutanen et al., 2007; King, 2008b,a). Hence it should not be considered surprising that X-ray emitting binaries can exceed $L_{\rm Edd}$ by as much as an order of magnitude in certain circumstances.

A key point to consider is that for SS 433, a system with mass ratio $M_2/M_X > 1$, the inferred mass transfer rate ($\sim 10^{-4}$ $\rm M_\odot$ $\rm yr^{-1}$) requires that it is in a very short-lived phase (Begelman et al., 2006). The clear implications are that either such systems are very rare, or their mass transfer rates are highly variable and/or the systems are very young, being located in star-forming regions.

2.4.3 Is the 115-day modulation due to disk/jet precession?

The observed modulation in the X-ray flux of NGC 5408 X-1 is $\approx 13-24\%$, depending on energy. Roughly the same levels of modulation were observed in SS 433

(Gies et al., 2002). These energy-dependent modulations in both SS 433 and NGC 5408 X-1 could be a common feature of such systems, and the spectral effects are perhaps simply related to the orientation of the precessing discs relative to our line of sight.

Figure 2.1 illustrates the relationship between the modulation and hardness ratio for SS 433. The relative flatness of the hardness ratio for SS 433 compared with that of NGC 5408 X-1 (cf. Figs. 3 and 4 of Strohmayer, 2009) may be accounted for by the difference in viewing angle; that is, SS 433 is an ADC source whose spectrum is modified by its obscuring corona but the same effect is less pronounced in NGC 5408 X-1 because of its lower inclination. Notably, the effect of absorption and emission of X-rays by a partially ionised wind from a companion star was suggested as a link between the energy-dependent amplitudes of the 115-day modulation and the orbital period of the system (Strohmayer, 2009); however, the same effect should be present in the case of SS 433 but is not. Also, the effect of beaming could concentrate the soft emission, which would explain the softening of the emission in NGC 5408 X-1 that occurs when the source brightens as a result of its assumed precession (Begelman et al., 2006). We suggest, therefore, that the 115-day periodicity found by Strohmayer (2009) for NGC 5408 X-1 is more likely superorbital in nature and similar to SS 433. This has implications for the determination of the black hole mass in ULXs, significantly reducing the mass needed to produce the observed properties.

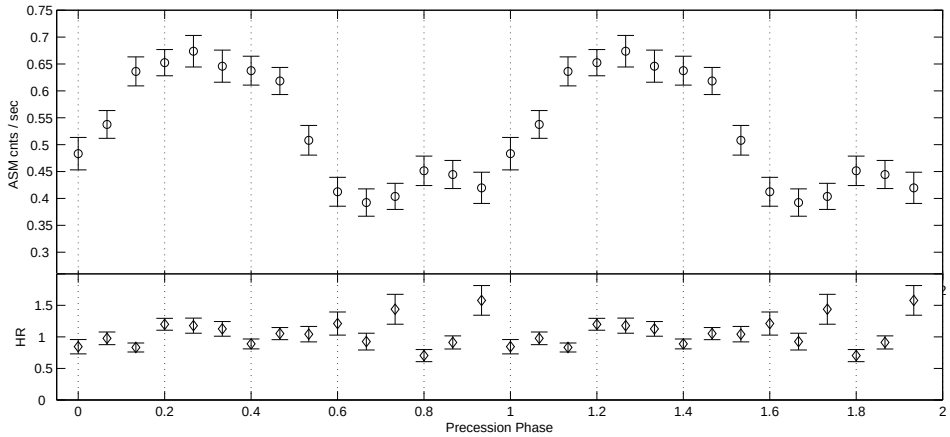

Figure 2.1: *Top panel*: RXTE/ASM count rate (vertical axis, in cts s^{-1}) for SS 433, plotted against precession phase (horizontal axis). *Bottom panel*: ASM hardness ratio, defined as C-band / (A-band + B-band), versus precession phase. The precession period is 162 days (Eikenberry et al., 2001).

2.5 Conclusions

If the nature of the ultra-luminous X-ray source (ULX) NGC 5408 X-1 is similar to that of the Galactic microquasar SS 433, then this ULX may be best described as an extragalactic high mass X-ray binary undergoing mass transfer at or near the Eddington rate, but at a lower inclination than would be typically seen in an accretion disc corona source (Begelman et al., 2006; Fabrika and Abolmasov, 2007; King, 2009). This would mean that in the case of NGC 5408 X-1, we are viewing the hot inner accretion flow, substantially boosting the apparent brightness of this source. The 115 day periodicity could be due to precession of the inner-disc/jet of NGC 5408 X-1, similar to SS 433, and not necessarily the orbital period as assumed in Strohmayer (2009).

With *Chandra* or *XMM-Newton*, the best currently-available X-ray imaging tele-

scopes, the count rate is typically too low to resolve the nature of the 115-day modulation in NGC 5408 X-1. Settling this will be possible with a next-generation X-ray facility that has a greater collecting area. Indeed, it is certainly possible that the entire class of ULXs are merely high mass X-ray binaries that are undergoing super-critical mass accretion onto a stellar-mass black hole, substantial beaming, or a combination of both. If we can confirm that NGC 5408 X-1 does contain a stellar-mass black hole, the link between ULXs and intermediate-mass black holes will have been severely challenged.

Note: the following is not part of the original Foster et al. 2010 paper.

Using a temporal baseline of $\sim$ 485 days, Strohmayer (2009) suggested that the observed 115-day modulation in the ULX NGC 5408 X-1 is the orbital period. The analysis presented in this chapter challenges this conclusion of Strohmayer (2009) and reinterprets this long-term modulation as being superorbital in nature. Since the publication of the Foster et al. (2010) paper, an additional study of the long-term temporal X-ray variability has been published by Grisé et al. (2013). Continued monitoring of NGC 5408 X-1 with *Swift* yielded a temporal baseline of 1532 days (including 2 periods of nearly daily observations—116 days in 2011 and 29 days in 2012), the most detailed monitoring of a ULX to date, allowing Grisé et al. to revisit the nature of the 115-day modulation. They found that while the overall X-ray spectral behavior remained unchanged over this expanded temporal baseline, the significance of the 115-day period did not increase. Furthermore, the 115-day

modulation disappeared after a few cycles, strongly confirming the work presented in this chapter. They found other modulations with a range of significance, but none that could be interpreted as a stable orbital period.

Chapter III

MONITORING THE VERY-LONG-TERM VARIABILITY OF X-RAY SOURCES IN THE GIANT ELLIPTICAL GALAXY M87

(Published as: Foster et al. 2013)

We report on our search for very-long-term variability (weeks to years) in X-ray binaries (XRBs) in the giant elliptical galaxy M87. We have used archival *Chandra* imaging observations to characterise the long-term variability of 8 of the brightest members of the XRB population in M87. The peak brightness of some of the sources exceeded the ultra luminous X-ray source (ULX) threshold luminosity of $\sim 10^{39}$ erg s^{-1}, and one source could exhibit dips or eclipses. We show that for one source, if it has similar modulation amplitude as in SS433, then period recoverability analysis on the current data would detect periodic modulations, but only for a narrow range of periods less than 120 days. We conclude that a dedicated monitoring campaign, with appropriately defined sampling, is essential if we are to investigate properly the nature of the long-term modulations such as those seen in Galactic sources.

3.1 Background

Chandra's sub-arcsecond resolution routinely images tens to hundreds of X-ray sources in individual observations of galaxies out to Virgo-cluster distances down to detection limits of $\sim 10^{37}$ erg s^{-1}. In analogy with the Milky Way, these are mostly

X-ray binaries (Fabbiano, 2006; Fabbiano and White, 2006). Detection limits are of order 10 counts, corresponding to count rates of several 10^{-4} c s^{-1} for typical exposure times of 10 to 100 ks so that meaningful lightcurves can only be obtained for the most luminous sources and only over time intervals of order 1 day at most. In rare cases, these lightcurves display periodic dips or other structures that can be used to constrain properties of the XRBs (e.g. Trudolyubov et al., 2002).

Multi-epoch X-ray observations of nearby galaxies allows for the study of the long-term variability of their X-ray source populations. We know from previous temporal and spectral analysis on the most luminous XRBs in nearby galaxies that they exhibit behaviours similar to what is seen in the Galactic XRBs (Fabbiano, 2006, and references therein). For example, Kong et al. (2002) find that among the 204 sources detected in the nearby spiral galaxy M31, 50 per cent are variable on the time-scale of several weeks and 13 are transients. We expect that ultraluminous X-ray sources (ULXs, defined as extranuclear point-like sources of X-rays with $L_X \gtrsim 10^{39}$ erg s^{-1}; e.g. Fabbiano and White, 2006) exhibit similar very-long-term modulations to those seen in the Galactic XRB population.

Owing to the lack of regular, multi-epoch observations of extragalactic XRBs, not much is known about their variability on time-scales of tens to hundreds of days (Fridriksson et al., 2008). Shorter time-scales can also be challenging for a variety of reasons: (a) count rates are always too low to see very short fluctuations like pulse periods; (b) a few short, presumably orbital, modulations have been detected in rare

cases in which the modulations occur 2–3 or more times within a single observation; however, these required exposure times in the 10–100 ks range, yet the typical *Chandra* exposure times reported here are less than this; and (c) transient-like behaviour–in which variations in luminosity are by a factor of 100 or greater–can almost always only be seen in multi-epoch exposures (typically separated by of order 100 days; e.g. Barnard et al., 2012a). Notable exceptions are some of the super-soft sources that vary rapidly within a given observation as well as between observations (Swartz et al., 2002; Fabbiano et al., 2003; Mukai et al., 2003; Fabbiano, 2006; Orio, 2006; Carpano et al., 2007). Thus, there are only a handful of examples of category (b) and (c). However, Kong (2011) demonstrated that regular pointed X-ray observations can be successfully deployed as monitoring instruments for extragalactic XRBs. This is particularly true of *Chandra X-ray Observatory* because of its superior resolution.

Longer term, non-orbital periodicities have been observed in both LMXBs and HMXBs, are termed *superorbital*, and range from tens to hundreds of days (Wen et al., 2006; Charles et al., 2010). The study of these modulations are a probe of the physical processes occurring within both the donor star and the accretion disc, and also a probe of the interaction of the intense X-ray luminosity with the accretion flow. These superorbital modulations display different properties depending on the type of interacting binary in which they are found (Charles et al., 2010). Highly relevant here are systems which display long-term superorbital modulations due to the coupled precession of their accretion discs and relativistic jets, such as the 35-d

modulation of Her X-1 (Petterson, 1977) and the 162-d modulation of SS433 (Margon, 1984); this mechanism may be responsible for the 115-d modulation seen in the ULX NGC 5408 X-1 (Foster et al., 2010). Only with a properly designed long-term monitoring program can we distinguish between the competing physical explanations of these superorbital periods.

To date, there have been extensive investigations of low-mass X-ray binaries (LMXBs) in M87 (Jordan, 2004; Jordán et al., 2004). Some studies contain observations separated by $\sim$ years, but without regularly repeated visits (typical of monitoring campaigns) extended over a baseline of many years. These have primarily focused on the pointing-to-pointing variability of the spectra and fluxes of LMXBs, and their association with globular cluster systems within M87. Other important work on these XRBs includes the nature of the apparently years-long transient outbursts discovered in these sources (Irwin, 2006). Better samplings have been obtained for LMXBs in globular clusters near the central region of M31 (Barnard et al., 2012b).

Monitoring of XRBs in the Milky Way has led to numerous major discoveries. For example, the discovery within our own Galaxy of relativistic jets and their superluminal motion in an accreting compact binary (Mirabel and Rodríguez, 1994) provided a link to the physics of distant quasars that are thought to behave in a similar (yet much more powerful) manner. The discovery of warping and precessing of the accretion discs was revealed through monitoring the long-term periodic variations in systems like SS433, Her X-1, and LMC X-3 (Margon et al., 1980; Cowley et al., 1991;

Gerend and Boynton, 1976). And, the discovery of sub-millisecond quasi-periodic oscillations (QPOs) in Sco X-1 (van der Klis et al., 1996) demonstrated a probe of the dynamics of the inner accretion flow in a XRB. As was shown in Margon et al. (1980), only with regular, sustained monitoring is it possible to measure longer-term (quasi-) periodicities that range from weeks to hundreds of days, with greater precision for the longer variations such as that achieved for SS433 coming only after years (up to decades) of follow-up observations (Eikenberry et al., 2001).

Chandra has now studied M87 many times over ~ 10 years; this has the potential for showing long-term modulations or transient behaviour in several XRBs in M87 (NGC 4486, $D = 17$ Mpc; Tully et al., 2008). We have selected a handful of the brightest sources in this galaxy and searched archival data to study their very long-term variability.

3.2 Methods

3.2.1 Observations and data reduction

The CIAO data reduction threads were used to process the data, generating level-2 events lists for each observation. We used version 4.4.1 of CIAO and version 4.5.1 of CALDB to reprocess the data. All the data presented here were recorded with *Chandra's* Advanced CCD Imaging Spectrometer (ACIS) S3 chip.

The data span the period 2000 July 29 to 2010 May 14. With a handful of exceptions, the 85 independent observations included in this analysis were typically

5 ks in duration. Chandra detects photons at a rate of about 10^{-4} c s^{-1} for a source of about 10^{-15} erg cm $^{-2}$ s^{-1} or only about 15 counts from a borderline ULX ($\sim 10^{39}$ erg s^{-1}) in these 5 ks observations. Also, many of the observations were performed in subarray mode (mostly due to the brightness of the core and jet of M87) and with varying roll angles. This led to somewhat sporadic coverage for a few sources.

To test for the presence of periods of high background or strong flares, we excluded the regions of the chip containing the core and jet of M87, as well as regions containing point sources detected by the CIAO tool `wavdetect`, then examined the lightcurve of the remaining events of the observation (binning of 200s) using the tool `lc_sigma_clip`, rejecting any events that are beyond 5σ from the mean count rates. No significant flares or periods of high background are detected. This means that the total exposure accumulated during the good time intervals (GTIs) as recomputed by `lc_sigma_clip` are nearly identical to the value of the keyword `EXPOSURE` in each observation's FITS file, and this time was used to compute the mean count rate.

3.2.2 Source selection

Eight sources were visually selected for analysis based on their apparent relative brightness in the X-ray images, their higher sampling given the roll angles of the observations, and their being distinct from either the nucleus of the galaxy or the jet (including knots or other clumps of diffuse emission). All of these sources appear in the catalogue of sources analysed in Jordán et al. (2004). The X-ray sources are

Table III.1. Summary of M87 X-ray source properties

No.	Name (CXOU)	Observation-specific properties $F_{\max}$ (10^{-14} erg cm^{-2} s^{-1})	$L_{\max}$ [D=17Mpc] (10^{39} erg s^{-1})	OBSID	General properties Median Rate (10^{-3} c s^{-1})	χ^2/dof	p
X1	J123047.7+122334	12.56	4.34	8576	3.42	178/79	$< 10^{-4}$
X2	J123049.2+122334	6.81	2.36	8513	3.69	193/79	$< 10^{-4}$
X3	J123049.6+122333	1.73	0.60	8516	1.18	79/79	0.54
X4	J123047.1+122415	8.98	3.10	8513	3.51	1199/32	$< 10^{-4}$
X5	J123053.2+122356	2.68	0.93	11513	1.01	115/37	$< 10^{-4}$
X6	J123044.7+122434	3.15	1.09	2707	0.56	297/7	$< 10^{-4}$
X7	J123050.8+122502	6.54	2.26	4918	4.09	577/59	$< 10^{-4}$
X8	J123049.1+122604	4.40	1.52	2707	3.64	557/13	$< 10^{-4}$

Note. — Maximum flux and luminosity (at the distance to M87) for each source, calculated as described in section 3.3.1 and uncorrected for absorption. The observation identification numbers (OBSID) corresponding to the peak values $F_{\max}$ (in 10^{-14} erg cm^{-2} s^{-1}) and $L_{\max}$ (in 10^{39} erg s^{-1}) for each source are shown for reference. Each source's data are fitted to a constant (the median count rate), and the resulting χ^2 statistic is tabulated, along with the degrees of freedom (dof). p is the null hypothesis probability.

listed in Table 3.2.2, and are hereafter individually referred to by the labels indicated therein (X1, X2, et cetera).

3.2.3 Extraction of source count rates

Source regions were defined as 1.5-arcsec circles centred on the identified point sources. The background regions were defined for the sources as annuli centred on the sources with inner and outer radii of 1.5 and 2.5 arcsec, respectively, to account for the diffuse emission that surrounds some of the sources while minimizing the effects of overlapping source and background regions. A spatial extraction of the total number of counts in the source and background regions, in the 0.5–8.0 keV range, was performed using the CIAO tool `dmextract`, with the error in the counts estimated using Gehrels' method (Gehrels, 1986). The larger of the asymmetric Poisson errors

is used for all calculations, so as to be conservative. Each point on the lightcurves represents the mean count rate (in c s^{-1}) of an individual observation. Data points on the lightcurves that are consistent with zero counts per second to within twice their 1σ Poisson errors are denoted by arrow markers on all lightcurves, and we treat these data as upper limits. An example is shown in Figure 3.1, which is the long-term lightcurve for the source X7.

The largest distance of any of these sources from the focal point (i.e. the narrowest point-spread function, or PSF) of the ACIS S3 chip is ≈ 3 arcmin. We estimate the 90 per cent encircled energy radius of a 1.5-keV event to be 1.0 arcsec on-axis and 2.0 arcsec at 3 arcmin off-axis, and that for a 6.4-keV event to be 2.0 arcsec on-axis and 2.6 arcsec at 3 arcmin off-axis. We checked the most off-axis sources for any differences in period detection arising from the factor of 2 increase in the radii of the extraction apertures and background annuli, finding none. In the event that a particular source was not on the active subarray, there was no data point recorded for such a source. We confirmed each off-subarray instance visually with SAOIMAGE DS9 after inspecting all extractions returning exactly zero counts for both source and background regions.

3.3 Analysis & Results

3.3.1 Peak X-ray Flux and X-ray Luminosity

Table 3.2.2 shows the observations having the largest X-ray flux and luminosity for each source. $F_{\rm max}$ (in units of 10^{-14} erg cm^{-2} s^{-1}) and $L_{\rm max}$ (in units of 10^{39} erg

s^{-1}) are the maximum values of the net model-independent (i.e., directly summed) X-ray flux and luminosity, respectively, over the entire baseline of observations. The sum of the flux within each source and background region was computed using the CIAO tools `eff2evt` and `dmstat`. The source regions are defined exactly as in the lightcurve extraction step and background fluxes were estimated for a region of the same radius near the source using SAOIMAGE DS9. The events were filtered on the 0.5–8 keV band. The fluxes are estimates based on the most likely energy of each arriving photon, and do not take into account a spectral model and the redistribution matrix. The luminosities are scaled to the assumed distance to M87 of 17 Mpc and uncorrected for absorption. All of our analysis below uses only the relative fluxes to search for variability and periodicity. The OBSID of the data sets corresponding to the peak values $F_{\max}$ and $L_{\max}$ for each point source is given as a reference.

3.3.2 Statistical analysis

Having invoked the Gehrels error estimation method in the counts extraction step, the Poisson errors in the case of low counts are properly taken into account. To be conservative, the larger of the asymmetric Poisson errors is used.

Each lightcurve was fitted with a horizontal line representing the median count rate for the individual sources to determine how well they agree with being constant. The results are shown in Table 3.2.2. In the goodness-of-fit analysis for χ^2, the null hypothesis is rejected for each source except for X3, indicating that the sources are

very unlikely to be non-variable.

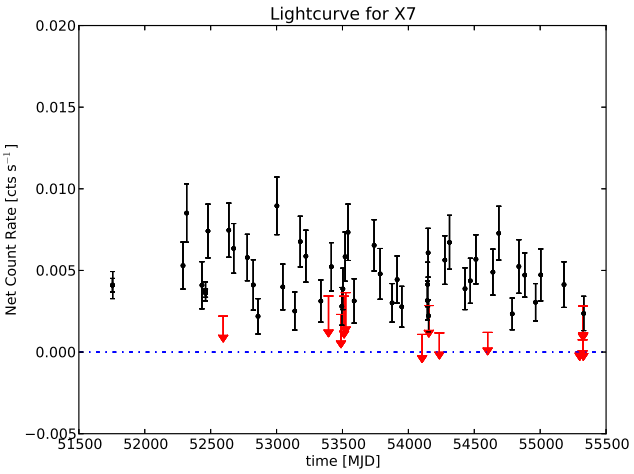

Figure 3.1: Long-term lightcurve for X7. Events were extracted in the 0.5–8.0 keV band. Each point on the lightcurves represents the mean count rate (in c s^{-1}) of an individual observation. The level of zero counts per second is represented by the dashed line. Arrow markers represent data that are consistent with zero counts per second, and the arrow length is the measurement error associated with the particular data point. In our analysis, we treat these points as upper limits.

3.3.3 Period search

Lomb-Scargle periodogram (LSP) analysis (Lomb, 1976; Scargle, 1982; Press and Rybicki, 1989) was applied to all extracted lightcurves and the resulting power spectra were searched for periods ranging from 30 days to 5 years. Figure 3.2 is the LSP of the data in Figure 3.1. In order to identify spurious period detections due to sampling, each power spectrum was compared to its corresponding window function power spectrum. Figure 3.3 is the window function of the data in Figure 3.1

corresponding to the power spectrum in Figure 3.2.

To determine the white noise levels, Monte Carlo simulations of 10,000 randomly generated data sets for each source were made using the time values, and the mean and standard deviation of the count rate values. LSPs were computed for the random data sets, and the resulting maxima in the power spectra are used to construct a cumulative probability distribution function, which describes the false-alarm probability (FAP) associated with each value of the power. Hence, a 3σ confidence level is the power associated with FAP of 0.27 per cent. For our lightcurves, the power typically associated with FAP of 0.27 per cent is $\approx$ 6–10. For the source X6, the number of data points is very small, and the computed 3σ confidence level is suspiciously low and perhaps not the "true" value.

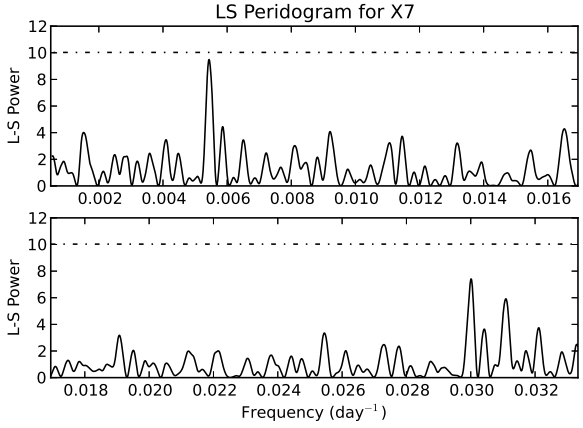

Figure 3.2: Lomb-Scargle periodogram for the data plotted in Figure 3.1. The frequencies correspond to periods ranging from 30 d to 5 yr. The highest peak corresponds to a period of $\sim$ 180 d. The dashed line represents the 3σ Monte Carlo confidence level.

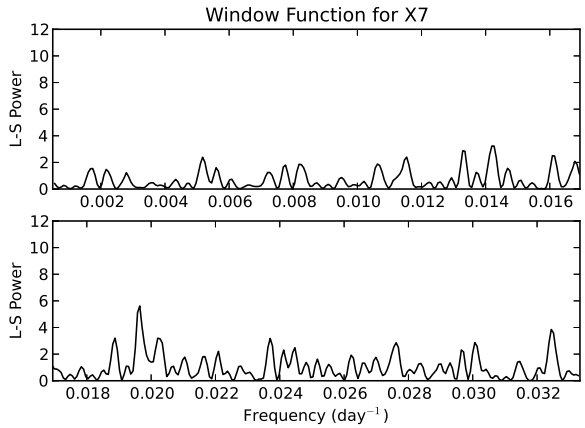

Figure 3.3: Window function for the data plotted in Figure 3.1. The frequencies correspond to periods ranging from 30 d to 5 yr.

3.3.4 Period recoverability analysis

Following an identical period search algorithm in section 3.3.3, we used our observed lightcurves to perform Monte Carlo simulations to calculate the recoverability of an extended range of periods. The recoverability chart for the data plotted in Figure 3.1 is shown in Figure 3.4. We conducted period recoverability analysis for amplitudes ranging from 25–200 per cent for the source X7. Generally, the recoverability charts show the expected result that the sampling of the available data is adequate for recovery of longer-term periods for higher amplitude modulations and for higher count rates. Interestingly, the charts also show that for amplitudes of $\sim$ 20 per cent, which is similar to that found in SS433, long-term periods would have low recoverability with the current sampling, and hence we would not have expected to see them had they been present. However, a more extreme amplitude variation of $\gtrsim$ 50 per cent could have enabled recovery of a wide range of periods in the existing

data for the source X7 had they been present.

3.4 Discussion

None of the sources show strong evidence for periodic variations, although the source X7 does show marginally significant periodic variability. The remaining sources may show variability of a more general nature (see Table 3.2.2). Henceforth, we will use the case of X7 (see Figure 3.1) as an exemplar in our discussion, although the analysis discussed in Section 3.3 was applied to all sources.

3.4.1 The need for a long-term *Chandra* campaign

The nature of ULXs in nearby galaxies continues as a subject of intense speculation and debate. Once considered to be the long-sought intermediate-mass BHs, current models invoke slightly heavier than stellar-mass BHs (20–50$M_{\odot}$) to account for their observed spectra and luminosities (Gladstone and Roberts, 2009). Their controversial status has been maintained with contemporary mass estimates for the ULX NGC 5408 X-1 ranging from 20 to 5000$M_{\odot}$ (Strohmayer, 2009). Its 115-d modulation is either orbital, or superorbital and related to a precessing jet, as in the hyperaccreting SS433. If the latter is the case then ULXs might be expected to display superorbital variations in the 50–200 day range, and these should be visible in X-ray lightcurves. Such variations require multi-year long term systematic studies and could only be carried out by *Chandra* due to its superior spatial resolution and its

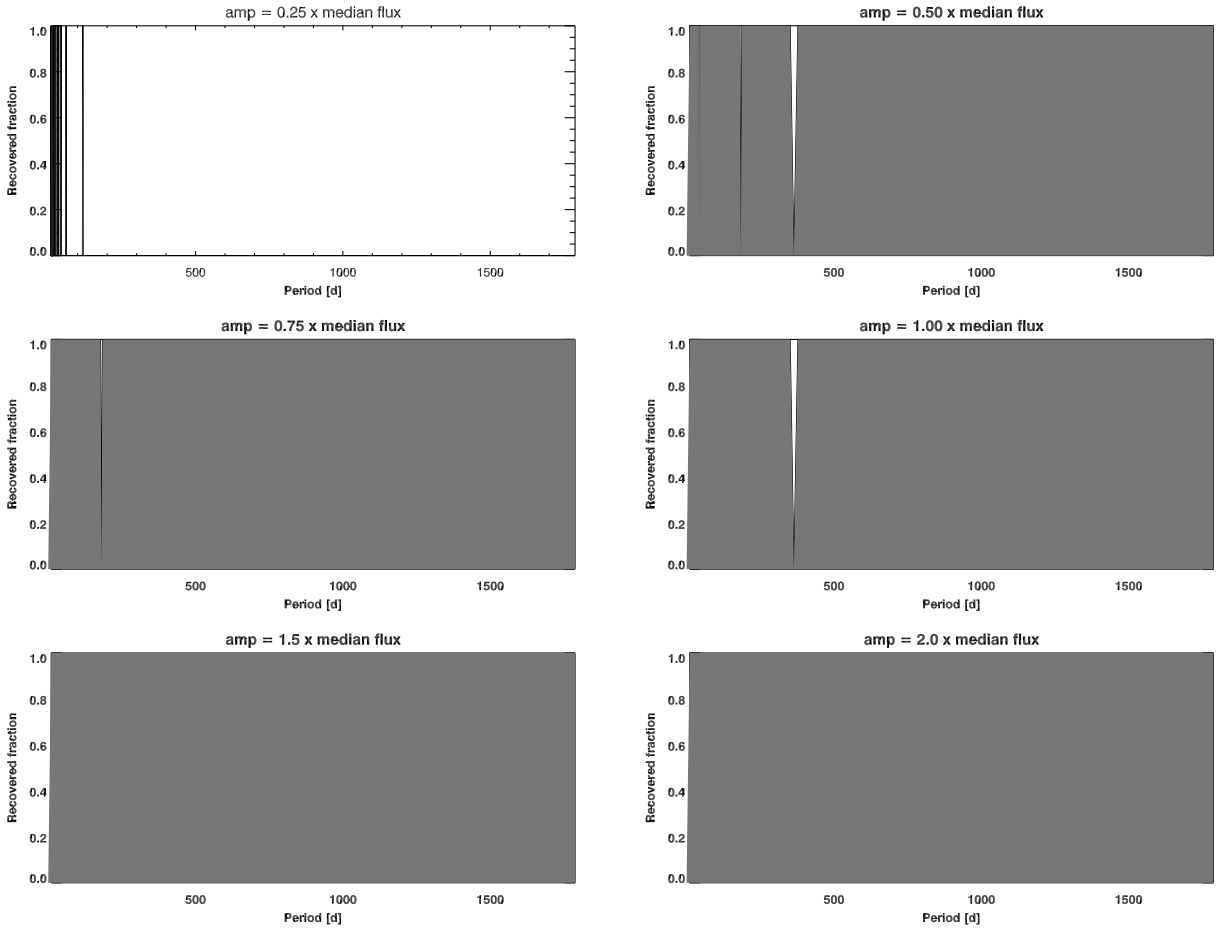

Figure 3.4: Period detection sensitivity for X7. We use the times and counts errors of the data points of the extracted lightcurve to generate 10,000 simulated lightcurves per period bin with randomized phases. LSP analysis was performed to test whether the input periods are recovered. The recovery fraction of each input period is determined by evaluating the LSPs of all the simulated lightcurves in each period bin. Each panel represents a different fixed input modulation amplitude. The recovery fraction is indicated by grey shading. Agreement to within 10 per cent of the input period is deemed a successful recovery.

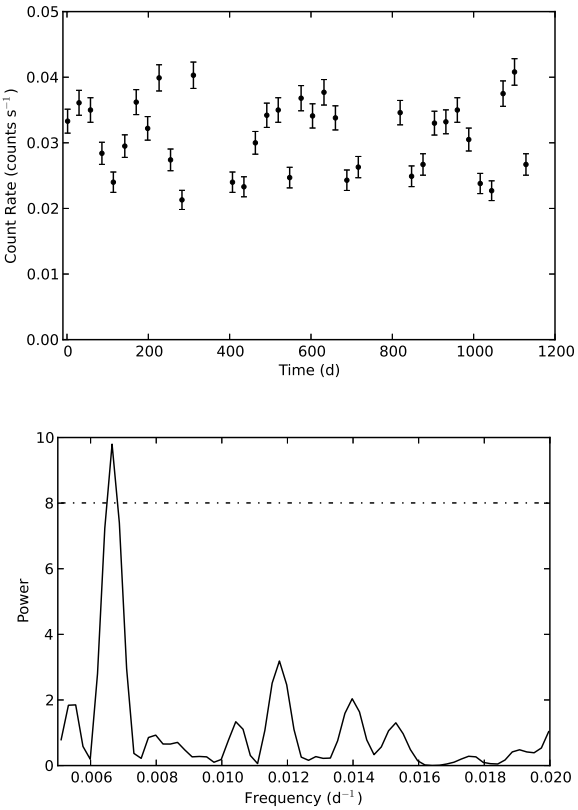

Figure 3.5: *Top panel*: Simulated *Chandra* ACIS light-curve of a ULX with a mean count rate of 0.03 c s^{-1}, which exhibits a 150-d sinusoidal modulation of 20 per cent. Twelve observations (one every 4 weeks) are simulated during each year for 3 years. *Bottom panel*: Lomb-Scargle periodogram of the data plotted to the left, together with the 3σ Monte Carlo confidence level (dashed line).

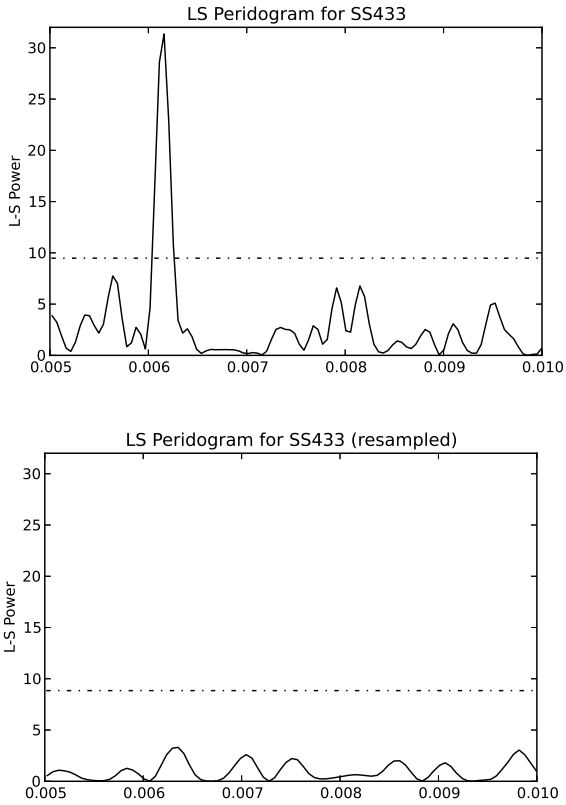

Figure 3.6: *Top panel*: Lomb-Scargle periodogram of the full 15-year RXTE/ASM 1-day averages lightcurve of SS433, which exhibits a ∼160-d sinusoidal modulation. *Bottom panel*: Lomb-Scargle periodogram of the same data resampled to match the sampling of X1, one of the best sampled sources in our analysis. The dashed lines represent the 3σ Monte Carlo confidence limits, illustrating that the random sampling has missed a known long-term period.

more flexible scheduling capabilities compared with other X-ray telescopes. Rather than having random sampling of the XRBs, if we design a sampling plan such as is proposed here (section 3.4.2) then we are able to recover these long-term periods.

3.4.2 Simulation of a long-term variability

To demonstrate the potential of a long-term X-ray campaign, we have used the observed X-ray modulations of NGC 5408 X-1 and SS 433 (described above as indicative of the periodicities we wish to search for) as input to simulate the outcomes of such a campaign. The range that we wish to be sensitive to (40–200 days) infers a data sampling rate of 12 observations per year (i.e. one every 3–4 weeks), which is then repeated over the subsequent two years. We found that the observations within each year's observing window can be pseudo-random, in that they should not be closer together than 14 days.

To test the viability of such a program, we have simulated the expected lightcurves for ULXs having a mean count rate of 0.03 counts per second. A time series is generated with an aperiodic, white noise component with root mean square variability rms_N to which we add a coherent sinusoidal signal with amplitude A and period P. The average of the series is taken to be the actual detected count rate of the ULX being simulated. The time series is binned over the typical observation duration of $\Delta T = 10^4$ s and a Poisson realisation is undertaken to obtain a simulated light-curve of counts per time bin. The simulated light-curve is then sampled on the 36

observations spread over the 3 years, and these data points are input to periodogram analysis, in order to see whether the input periodicity P can be recovered.

We have constructed simulations with periodic modulations of 50, 100 and 150 days, with amplitudes of 20 per cent (typical of M82 X-1, NGC 5408 X-1, and SS433), and for a variety of samplings. All recover the input periodicity, but with varying degrees of significance. Best results are obtained with 12 observations per year (spacings of 2–4 weeks), for all the periodicities, and a typical example, including both the lightcurve and the power spectrum, is shown in Figure 3.5. Compare this with the power spectrum of the 15-year *RXTE*/ASM 1-day averages data (Wen et al., 2006) for SS433 in Figure 3.6, which shows that if we have the random sampling of the M87 data (right panel), the well-established 162-d period (e.g. Eikenberry et al., 2001) is not recovered.

All previous attempts to study long-term variability with *Chandra* and/or *XMM-Newton* have been based on relatively few archival observations randomly distributed in time. They serve only to indicate why such a study needs to be undertaken in a well-defined, systematic manner over at least a 3-year baseline, as simulated here.

3.5 Conclusions & Future Work

We identified 8 XRBs in M87 to search for very-long-term periods ($P \sim$ weeks to years). Using Lomb-Scargle periodogram analysis, we found no statistically significant periods. We also found no visible evidence of transient outburst events. However,

using period recoverability analysis we found that for amplitude modulations of ~ 20 per cent (similar to what is observed for SS433, NGC5408, and M82), period recovery with the current data is very low for a wide range of periods. Only if the amplitude of the modulation is $\gtrsim 50$ per cent could a wide range of periods be found.

We continue to monitor the *Chandra* archive for sources observed over many years. Perhaps with better sampling of these sources with facilities such as *Chandra*, we can begin to understand their longer-term variations and its consequences for the dynamics of XRBs.

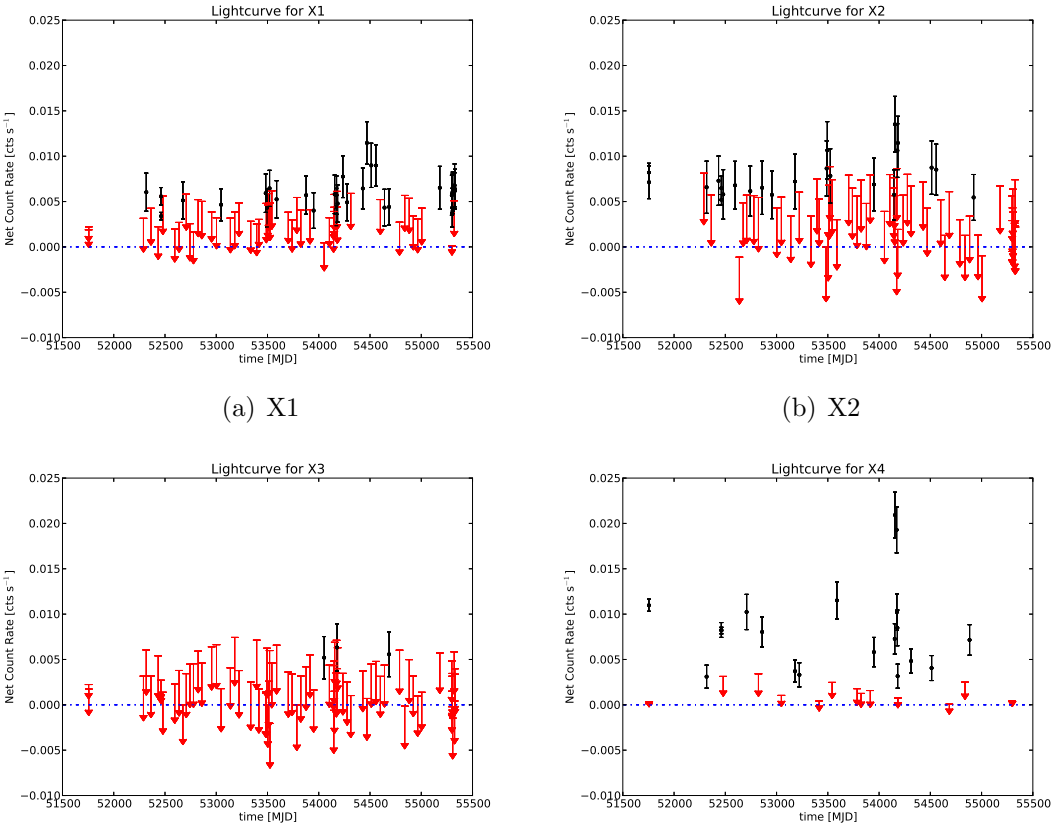

(a) X1

(b) X2

(c) X3

(d) X4

Figure 3.7: Long-term lightcurve for sources X1, X2, X3, and X4. Events were extracted in the 0.5 - 8.0 keV band. Each point on the lightcurves represents the mean count rate (in c/s) of an individual observation. The level of zero counts per second is represented by the dashed line. Arrow markers represent data that are consistent with zero counts per second, and the arrow length is the measurement error associated with the particular data point. In our analysis, we treat these points as upper limits.

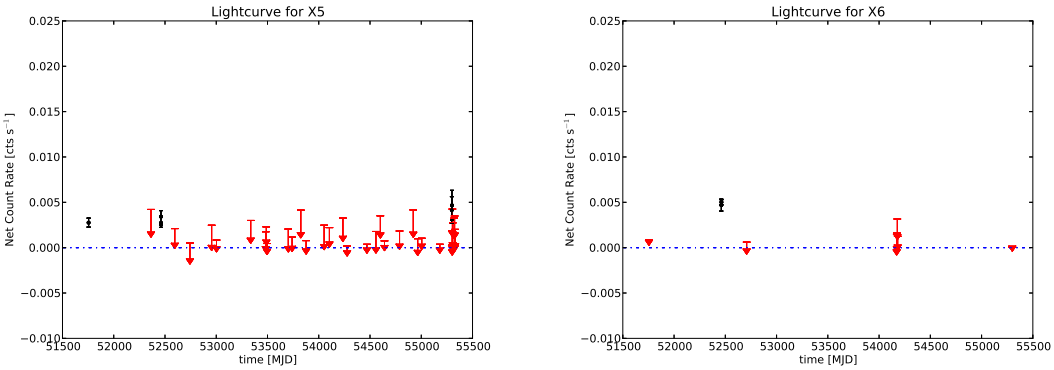

(a) X5

(b) X6

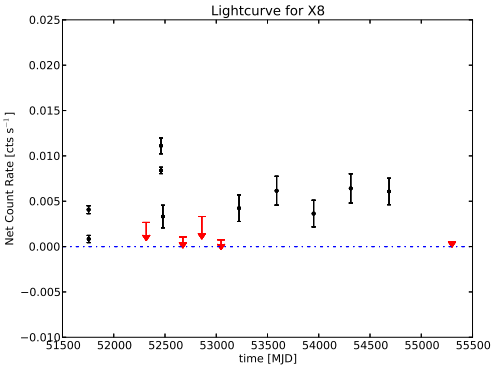

(c) X8

Figure 3.8: Long-term lightcurve for sources X5, X6, and X8. Events were extracted in the 0.5 - 8.0 keV band. Each point on the lightcurves represents the mean count rate (in c/s) of an individual observation. The level of zero counts per second is represented by the dashed line. Arrow markers represent data that are consistent with zero counts per second, and the arrow length is the measurement error associated with the particular data point. In our analysis, we treat these points as upper limits.

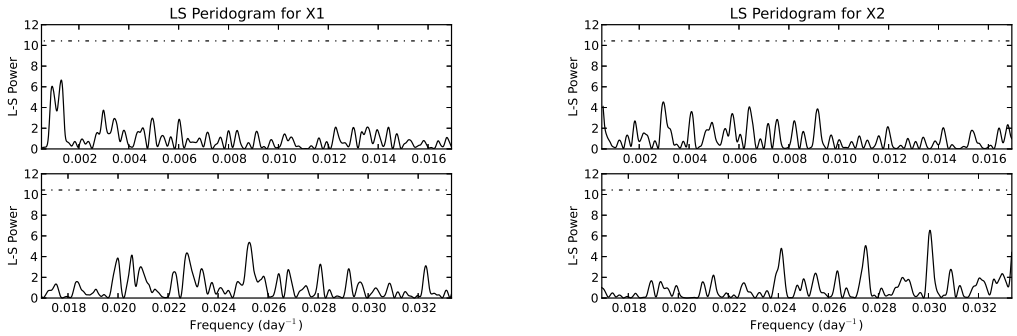

(a) X1

(b) X2

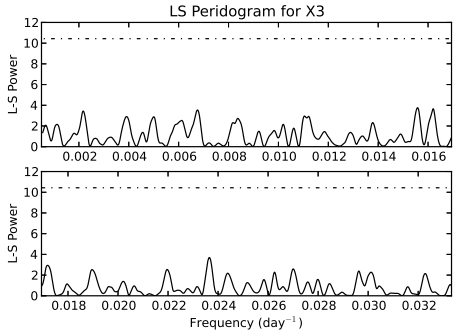

(c) X3

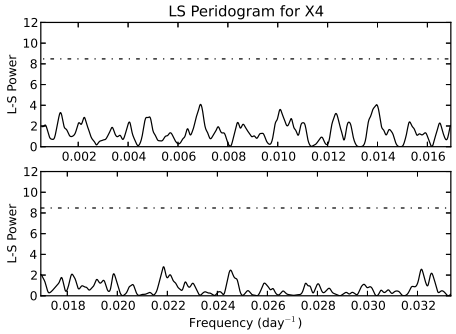

(d) X4

Figure 3.9: Lomb-Scargle periodograms for the data plotted in Figure 3.7. The frequencies correspond to periods ranging from 30 d to 5 yr. The dashed line represents the 3σ Monte Carlo confidence level.

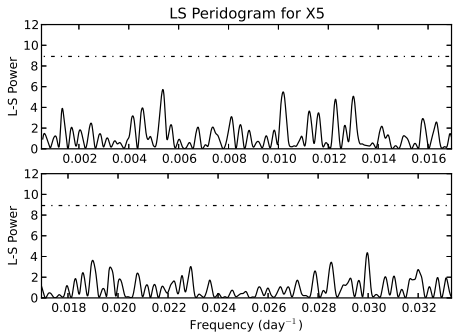

(a) X5

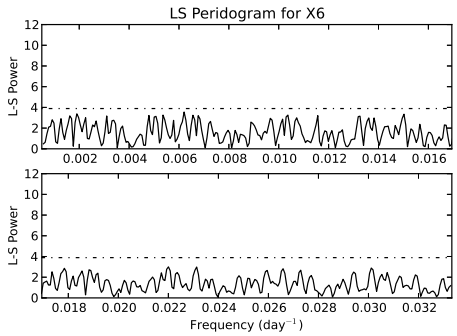

(b) X6

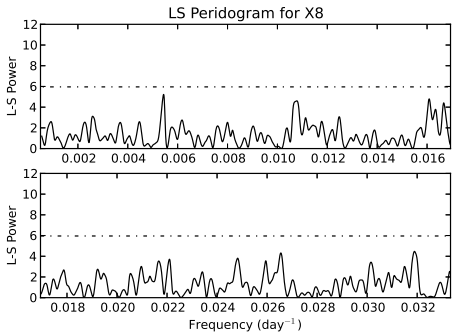

(c) X8

Figure 3.10: Lomb-Scargle periodograms for the data plotted in Figure 3.7. The frequencies correspond to periods ranging from 30 d to 5 yr. The dashed line represents the 3σ Monte Carlo confidence level.

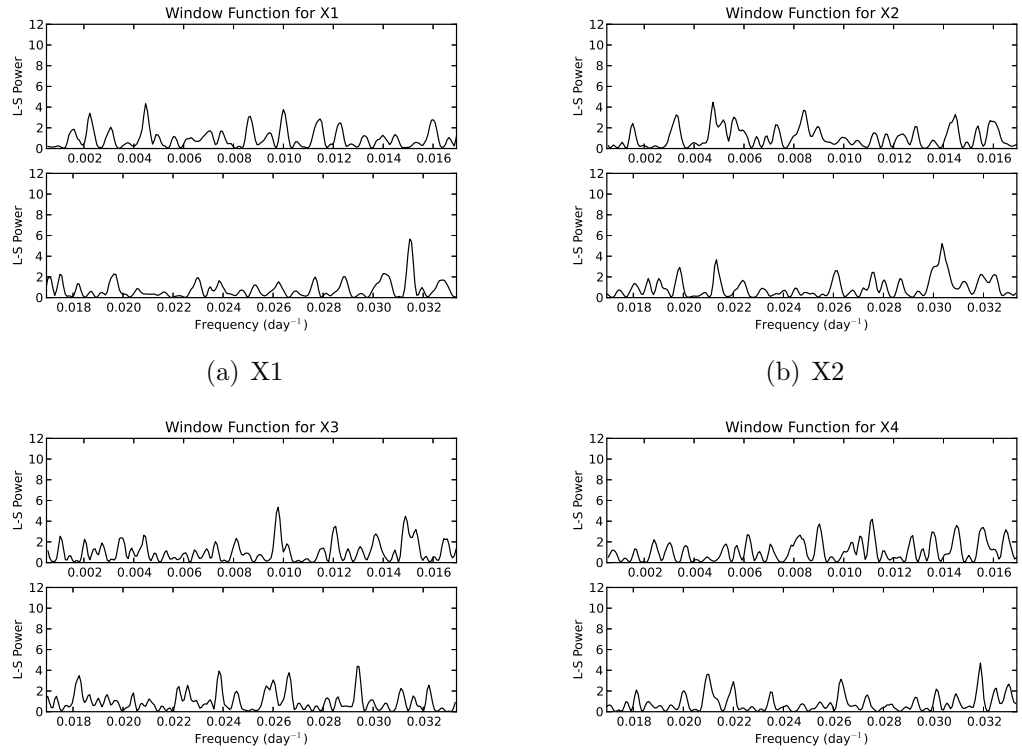

(a) X1

(b) X2

(c) X3

(d) X4

Figure 3.11: Window functions for the data plotted in Figure 3.7. The frequencies correspond to periods ranging from 30 d to 5 yr.

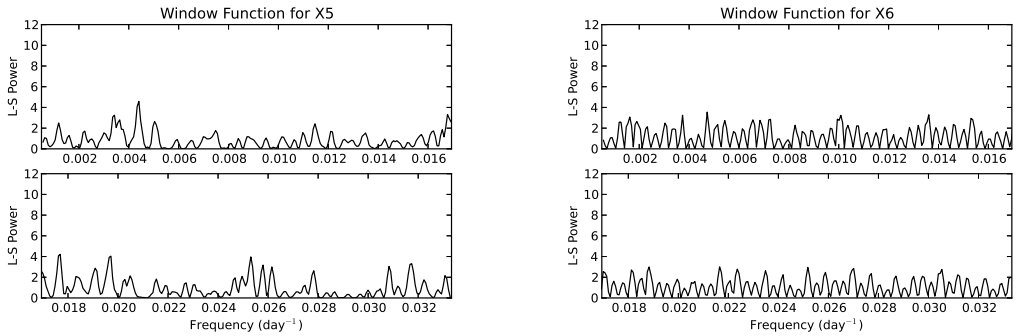

(a) X5

(b) X6

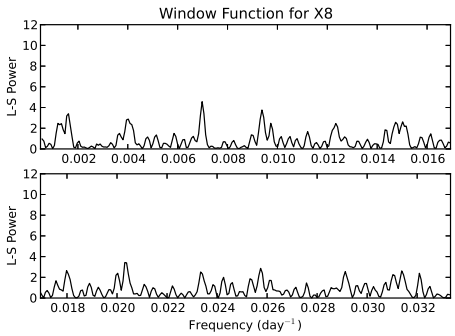

(c) X8

Figure 3.12: Window functions for the data plotted in Figure 3.7. The frequencies correspond to periods ranging from 30 d to 5 yr.

3.9 Period Detection Sensitivity

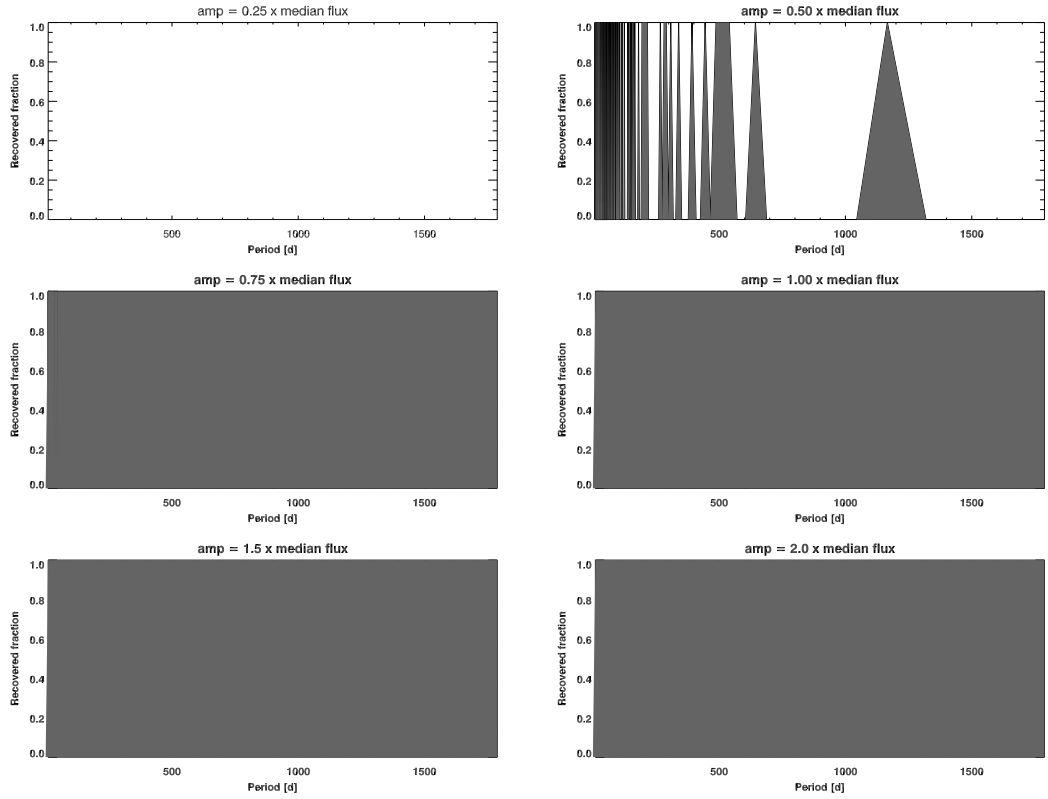

Figure 3.13: Period detection sensitivity for X1. We use the times and counts errors of the data points of the extracted lightcurve to generate 10,000 simulated lightcurves per period bin with randomized phases. LSP analysis was performed to test whether the input periods are recovered. The recovery fraction of each input period is determined by evaluating the LSPs of all the simulated lightcurves in each period bin. Each panel represents a different fixed input modulation amplitude. The recovery fraction is indicated by grey shading. Agreement to within 10 per cent of the input period is deemed a successful recovery.

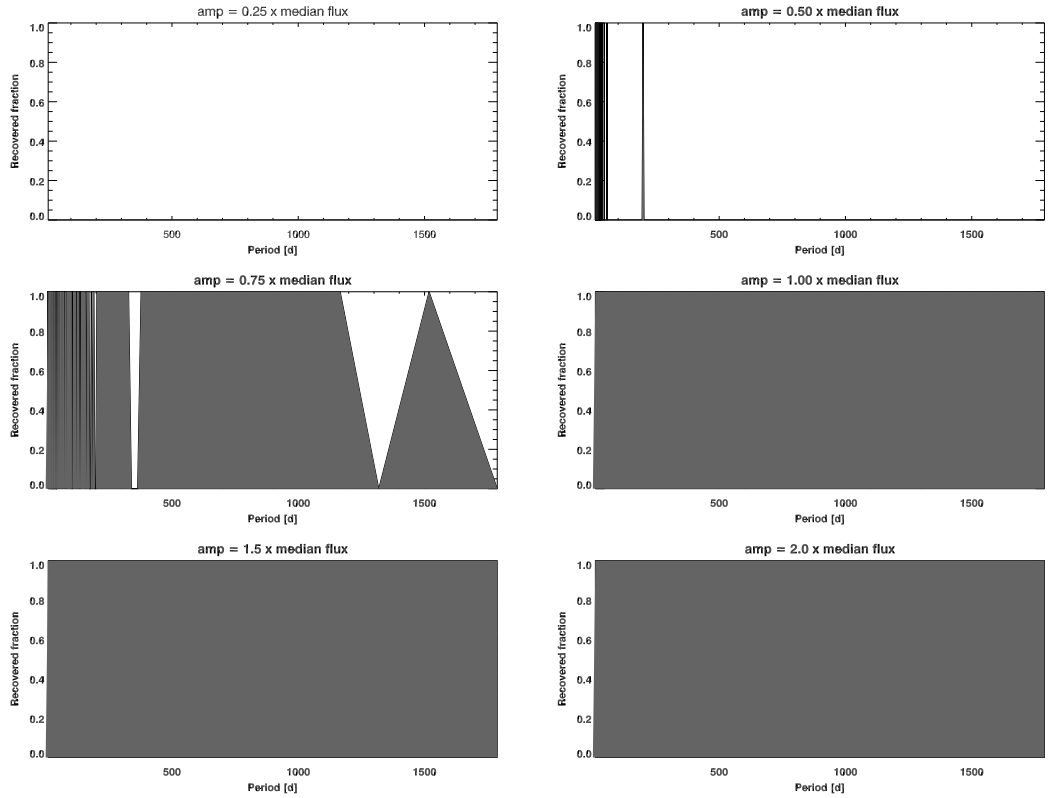

Figure 3.14: Period detection sensitivity for X2. We use the times and counts errors of the data points of the extracted lightcurve to generate 10,000 simulated lightcurves per period bin with randomized phases. LSP analysis was performed to test whether the input periods are recovered. The recovery fraction of each input period is determined by evaluating the LSPs of all the simulated lightcurves in each period bin. Each panel represents a different fixed input modulation amplitude. The recovery fraction is indicated by grey shading. Agreement to within 10 per cent of the input period is deemed a successful recovery.

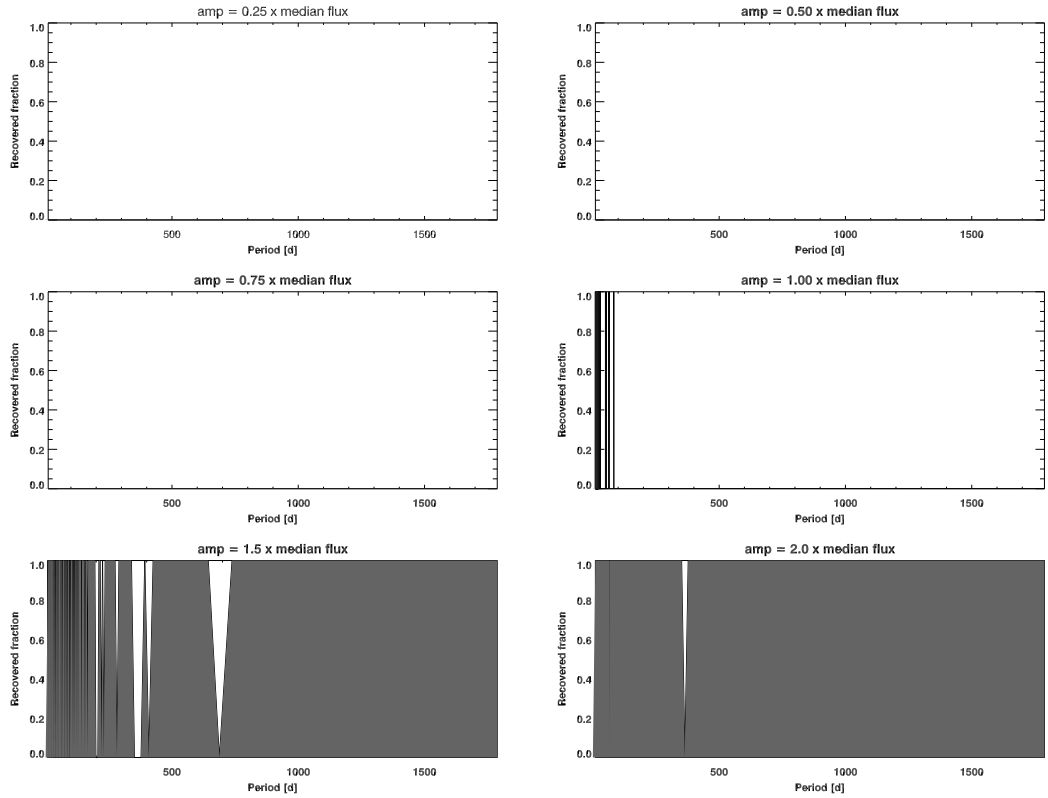

Figure 3.15: Period detection sensitivity for X3. We use the times and counts errors of the data points of the extracted lightcurve to generate 10,000 simulated lightcurves per period bin with randomized phases. LSP analysis was performed to test whether the input periods are recovered. The recovery fraction of each input period is determined by evaluating the LSPs of all the simulated lightcurves in each period bin. Each panel represents a different fixed input modulation amplitude. The recovery fraction is indicated by grey shading. Agreement to within 10 per cent of the input period is deemed a successful recovery.

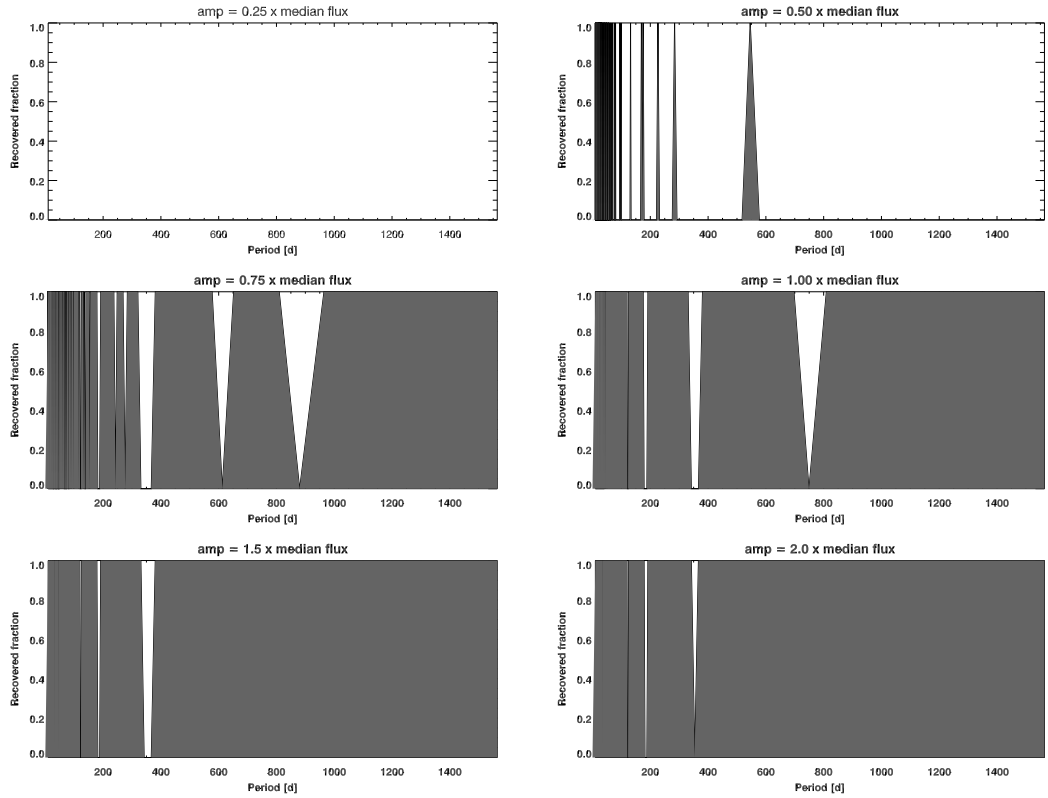

Figure 3.16: Period detection sensitivity for X4. We use the times and counts errors of the data points of the extracted lightcurve to generate 10,000 simulated lightcurves per period bin with randomized phases. LSP analysis was performed to test whether the input periods are recovered. The recovery fraction of each input period is determined by evaluating the LSPs of all the simulated lightcurves in each period bin. Each panel represents a different fixed input modulation amplitude. The recovery fraction is indicated by grey shading. Agreement to within 10 per cent of the input period is deemed a successful recovery.

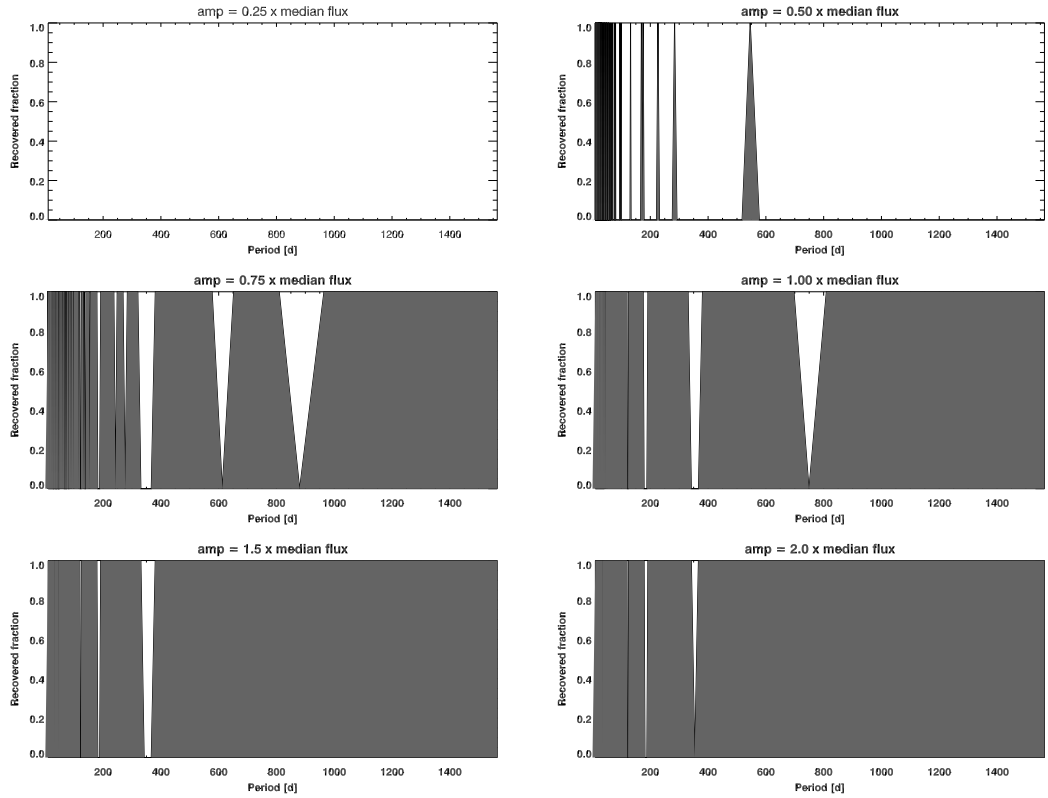

Figure 3.17: Period detection sensitivity for X5. We use the times and counts errors of the data points of the extracted lightcurve to generate 10,000 simulated lightcurves per period bin with randomized phases. LSP analysis was performed to test whether the input periods are recovered. The recovery fraction of each input period is determined by evaluating the LSPs of all the simulated lightcurves in each period bin. Each panel represents a different fixed input modulation amplitude. The recovery fraction is indicated by grey shading. Agreement to within 10 per cent of the input period is deemed a successful recovery.

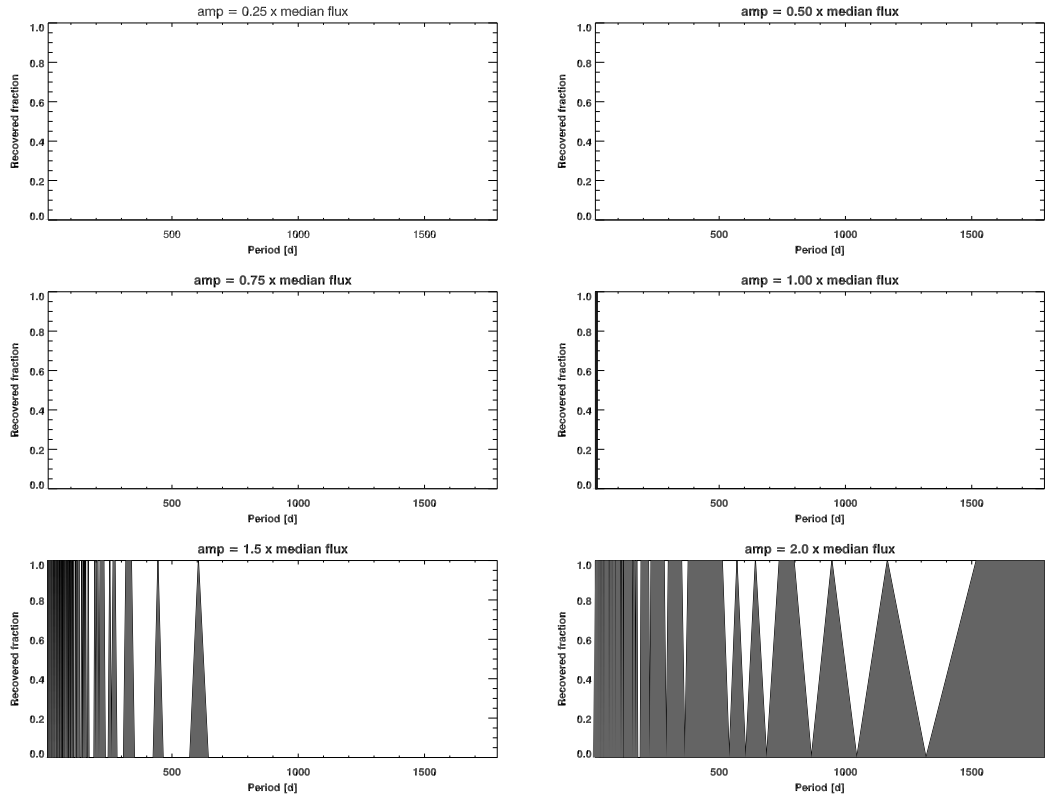

Figure 3.18: Period detection sensitivity for X6. We use the times and counts errors of the data points of the extracted lightcurve to generate 10,000 simulated lightcurves per period bin with randomized phases. LSP analysis was performed to test whether the input periods are recovered. The recovery fraction of each input period is determined by evaluating the LSPs of all the simulated lightcurves in each period bin. Each panel represents a different fixed input modulation amplitude. The recovery fraction is indicated by grey shading. Agreement to within 10 per cent of the input period is deemed a successful recovery.

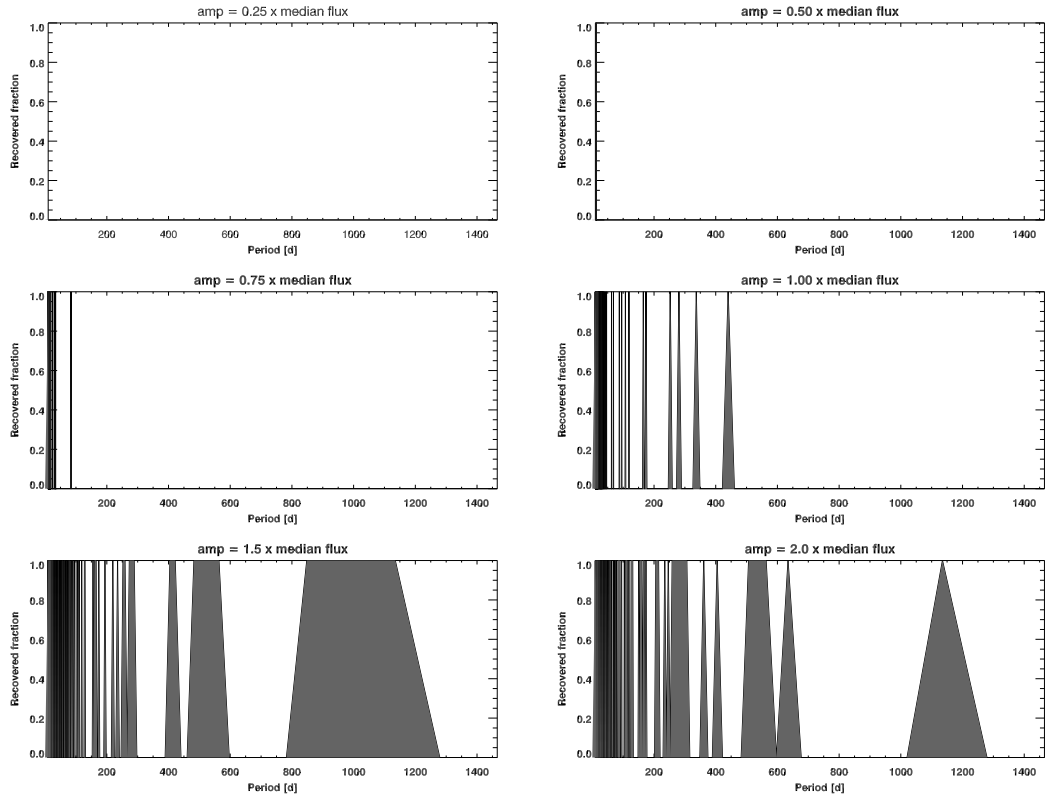

Figure 3.19: Period detection sensitivity for X8. We use the times and counts errors of the data points of the extracted lightcurve to generate 10,000 simulated lightcurves per period bin with randomized phases. LSP analysis was performed to test whether the input periods are recovered. The recovery fraction of each input period is determined by evaluating the LSPs of all the simulated lightcurves in each period bin. Each panel represents a different fixed input modulation amplitude. The recovery fraction is indicated by grey shading. Agreement to within 10 per cent of the input period is deemed a successful recovery.

Chapter IV

DEM L241, A SUPERNOVA REMNANT CONTAINING A HIGH-MASS X-RAY BINARY

(Published as: Seward, Charles, Foster, et al. 2012)

A *Chandra* observation of the Large Magellanic Cloud supernova remnant DEM L241 reveals an interior unresolved source which is probably an accretion-powered binary. The optical counterpart is an O5III(f) star making this a High-Mass X-ray Binary (HMXB) with orbital period likely to be of order tens of days. Emission from the remnant interior is thermal and spectral information is used to derive density and mass of the hot material. Elongation of the remnant is unusual and possible causes of this are discussed. The precursor star probably had mass $> 25 M_{\odot}$

4.1 Background

In the Magellanic Clouds there are now 34 supernova remnants known to emit X-rays. Ten of these have interior pulsar-wind nebulae (PWNe) or compact objects which also radiate in the X-ray band. Although the sample is small, there is great diversity. Several manifestations of neutron stars are represented and the present observation may be an example of yet another.

X-rays from the supernova remnant SNR 0535-67.5 in the H II region DEM L241

(Davis et al. 1976) were first detected in 1979 by Long et al. (1981). The supernova remnant was first identified by Mathewson et al. (1985) and mapped using the optical [S II] emission as seen in Figure 4.1 which shows the remnant and the surrounding H II emission. Since the initial *Einstein* observation there have been X-ray detections by *ROSAT* (Williams et al. 1999), *XMM* (Bamba et al. 2006), and now *Chandra*. The *XMM* data provided the first detailed X-ray image and showed elongated diffuse emission filling the area outlined by [SII] filaments with a bright hard point source centered in the SE section. Because the spectrum of this source was a power law, Bamba et al. (2006) identified it as an unresolved PWN. The *Chandra* observation was planned to resolve this object and to distinguish the expected point-like pulsar from surrounding diffuse emission. The *Chandra* result indeed shows a clear point-like hard source but there is no sign of a PWN close to or surrounding the point source.

4.2 The *Chandra* Observation

Chandra observed DEM L241 on 2011 February 7 and 8 for 46 ks with the ACIS detector. The observation was in two continuous parts of length 22 and 24 ks (OBSIDs 12675 and 13226) separated by an interval of 40 ks. Figures 4.2 and 4.3 show the result. The supernova remnant has dimension $2.2' \times 5.3'$ with diffuse emission filling the interior and with no limb brightening from an outer shell. The remnant appears to be almost divided into two parts. The southern section, called the "Head" by Bamba et al (2006) has dimension approximately $1.4' \times 1.8'$ with the bright compact source

somewhat off-center. The elongated northern part, called the "Tail" has dimension $2.2' \times 3.7'$. The entire X-ray remnant fits within and follows the [S II] filaments seen in Figure 4.1. The compact source, being close to the brightest diffuse emission, appears to be associated with the remnant but its characteristics are unusual, as will be discussed in the next section.

4.3 The Compact Source

4.3.1 X-rays

The compact X-ray source appears point-like and has a luminosity $\sim 2 \times 10^{35}$ erg s^{-1} at the LMC distance of 50 kpc. No extended PWN is visible in the immediate vicinity and the diffuse emission close to the point source is thermal. As shown in Figure 4.4, the *Chandra* telescope PSF (Point Spread Function) accounts very well for the appearance of the source. The source X-ray spectrum is a power law and it is appreciably harder than that from the diffuse parts of the remnant.

It is very unlikely that the object is a background AGN. There are an average of 0.2 AGN deg^{-2} at this flux level (Kim et al. 2007) so the chance of finding one even within the $2' \times 5'$ remnant is only $\approx 6 \times 10^{-4}$. Furthermore the X-ray spectral index is -1.3 which is harder than the mean index of -1.9 (with dispersion of 0.5) for radio quiet QSOs.

The X-ray spectrum is also too hard to be that of a foreground normal star or even that of the optical counterpart O5III(f) star. This star itself is expected to be

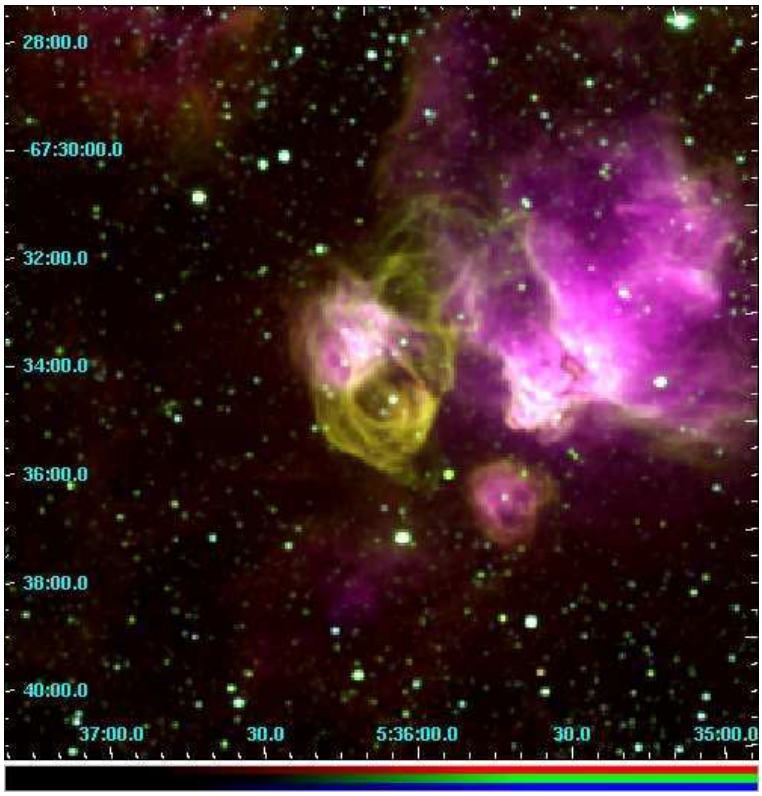

Figure 4.1: The H II region DEM L241 showing H emission in red and [S II] emission in yellow. The [S II] emission defines the supernova remnant and correlates well with the X-rays. Figure from Smith et al. (1999).

an X-ray source but with a soft spectrum and luminosity only 1% of the flux we observe here (Chlebowski 1989). Colliding winds in a binary system could be more energetic but the luminosity of observed systems (e.g. W140 - Pollock et al. 2005) is still an order of magnitude less than that of this object. We conclude that the source is neither a foreground nor a background object and is probably associated with the remnant.

The *Chandra* X-ray spectrum is shown in Figure 4.5. Data are from a circular region with radius 4″ centered on the source and background was taken from a

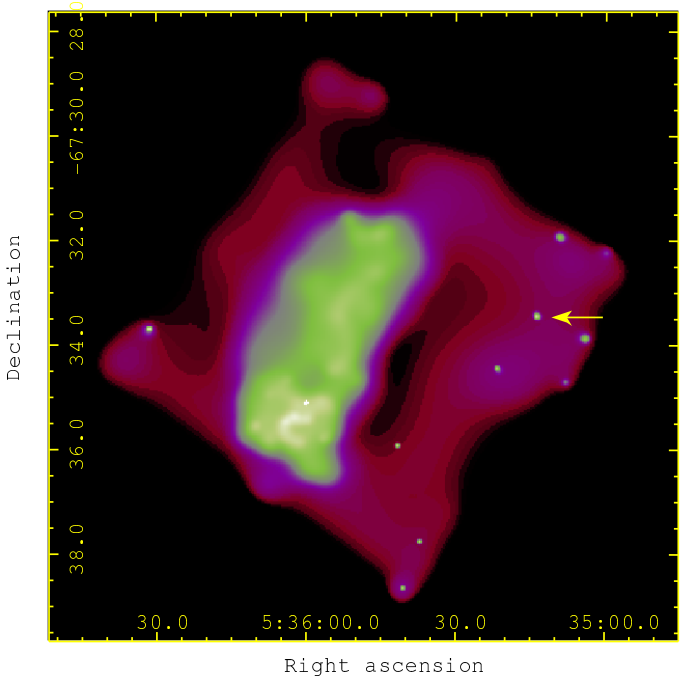

Figure 4.2: The field of the $8' \times 8'$ *Chandra* S3 chip. This is an adaptive smoothing of X-ray data in the energy range 0.3 - 3 keV. The color map shows increasing surface brightness going from red to green to white. The scale has been set so that the supernova remnant in this figure is green. The point source in the SE part of the remnant is quite bright and is unresolved by *Chandra*. The next Figure better shows the true prominence of this source. Other unresolved sources in this field are foreground or background objects. One of these, the star HD 269810, is indicated by an arrow and serves as a fiducial reference.

surrounding $5''$ wide annulus. The count rate was 0.057 s^{-1} which, in the ACIS instrument which integrates for 3.2 s, leads to a 3% chance of two events being recorded as one. This pileup is not severe but enough to distort the spectrum. We therefore incorporated a pileup correction, *jdpileup*, in the *Chandra CIAO/SHERPA* spectral analysis. Results are listed in Table 1. The best fit was a power law with index -1.28 $\pm$0.08 and is shown in the figure. Without the pileup correction the best-fit index was -1.10 $\pm$0.06. (The uncertainties given are 1σ.) The index measured with *XMM*,

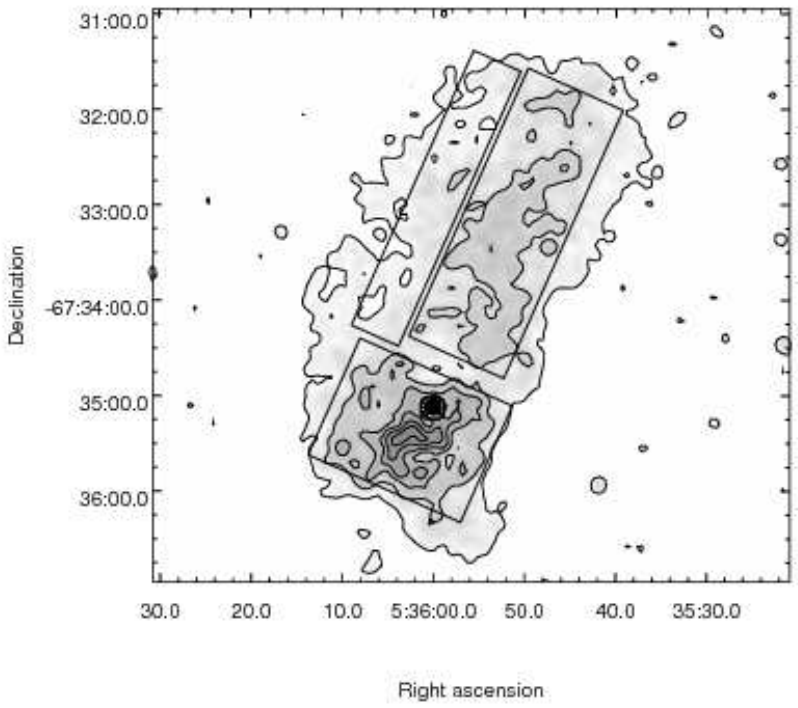

Figure 4.3: *Chandra* observation of the remnant showing contours of constant X-ray surface brightness overlaid on a smoothed image. Smoothing is Gaussian with $\sigma = 5''$. Contours are linear with separation 0.3 counts arcsecond^{-2}. Note the diffuse structure just south of the bright unresolved source. The three boxes show spectral extraction regions.

free of pile up but with larger background subtraction, was -1.57±0.05 (Bamba et al. 2006). The lack of agreement could be due to an inadequate pileup correction, larger uncertainties than quoted, or a variable source. The *Chandra* and *XMM*-measured luminosities are the same. The luminosity range in Table 1 is due to the observed variability. We also fit a *xsdiskbb* model to the data since this is appropriate for accretion powered sources and there is reason to believe this object may be part of a binary system. The fit is reasonable but the absorption is too low. If this is an accretion powered system, a more elaborate model is needed.

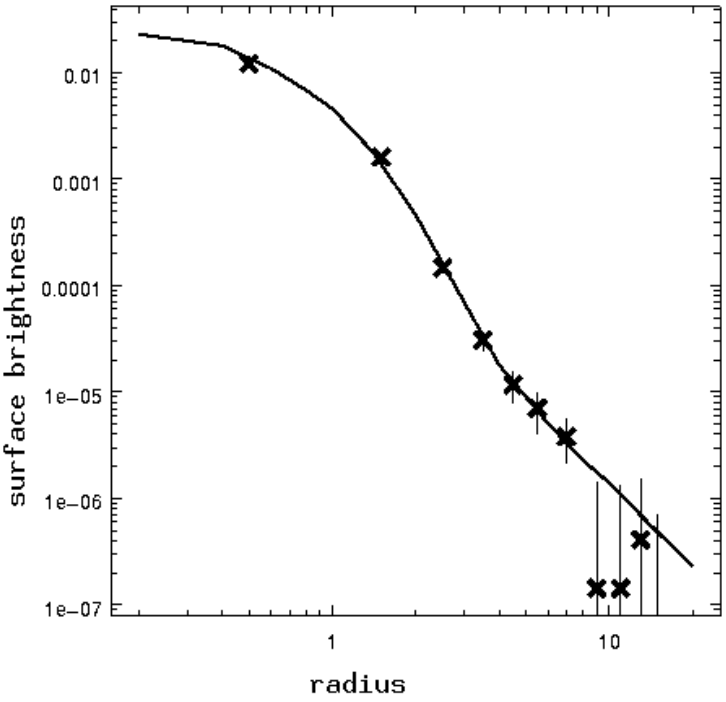

Figure 4.4: Radial surface brightness of CXOU 053600.0-673507 compared with the *Chandra* telescope point spread function (PSF). The diffuse SNR emission has been subtracted. Data points are crosses with 1 σ uncertainties due to counting-statistics. The solid curve is the *Chandra* mirror PSF from Jarius 2002. Units of radius are ACIS pixels (=0.492 arcsecond). Units of surface brightness are counts s^{-1} $pixel^{-1}$.

4.3.2 Location and variability

The bright optical counterpart, a V=13.5 O5III(f) star, is easily visible within the Head of the remnant in Figure 1. This had been noted as a possible counterpart to the *Einstein* source CAL 60 (from the catalog of Long et al, 1981) by Crampton et al. (1985) who published a finding chart and spectrum. Since the source CAL 60 includes the diffuse emission as well as the point source we will refer to the point source as CXOU 053600.0-673507. Our X-ray position is 2.2″ S of the *XMM* position and $< 0.6''$ from this O star. X-ray positions are listed in Table 2 with uncertainty

Table IV.1. Compact source spectral fits

Form	Energy Range (keV)	Photon Index	ISM Absorption N_H (10^{22})	Reduced χ^2	L_x (erg s^{-1})
power law	0.3-10	$\Gamma = 1.28 \pm 0.08$	0.19 ± 0.034	1.26	$2.5 - 3.2 \times 10^{35}$
diskbb	0.3-10	$kT_{in} = 2.43 \pm 0.23$	0.073 ± 0.023	1.38	2.3×10^{35}

Table IV.2. Measured source positions

Source	Waveband	RA (J2000)	Dec (J2000)
CXOU J053600.0-673507	X-ray	05:36:00.01 ± 0:0:0.02	-67:35:07.5 ± 0:0:0.2
O star	optical	05 35 59.9 ± 0:0:0.08	-67 35 06.3 ± 0:0:0.5
O star	IR	05:36:00.01	-67:35:07.6
HD 269810	X-ray	05:35:13.82 ± 0:0:0.05	-67:33:28.0 ± 0:0:0.3
HD 269810	IR	05:35:13.89	-67:33:27.6
HD 269810	TYCHO-2	05:35:13.90	-67:33:27.6

the larger of that from counting statistics or the difference between positions from the two halves of our observation. The systematic error associated with *Chandra* positions is 0.6″ at 90% confidence. The star HD2269810 is also in the field and our X-ray position for this star is 0.5″ from the optical and 2MASS IR survey position, so the registration of the *Chandra* field is good and we adopt 0.6″ as the uncertainty of the X-ray position.

The source is variable. The count rate in the second part of the observation increased 25% over that obtained in the first part. No variability was seen on time scales shorter than $\sim 10^4$ s although the observation was not sensitive to periods shorter than 6 s or to pulsed fractions $< 20\%$. This object cannot be an unresolved

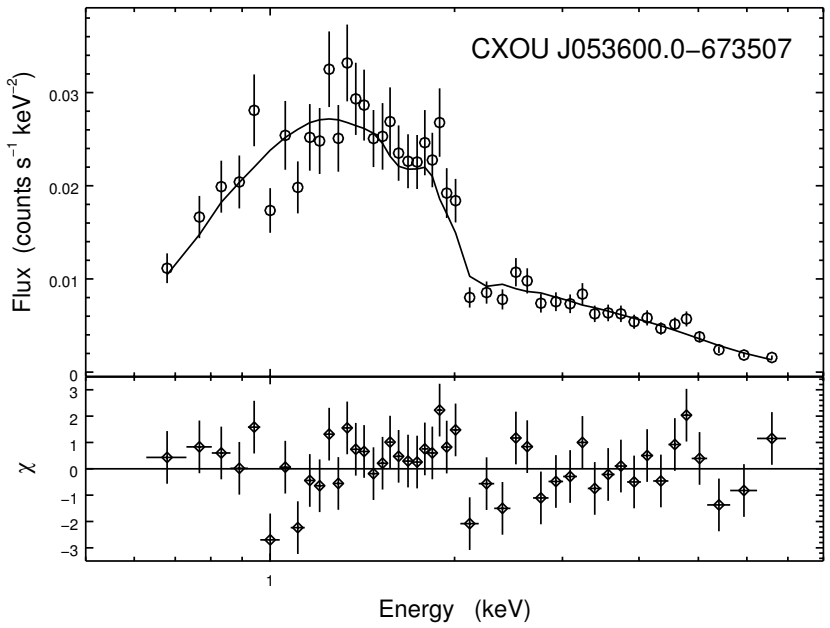

Figure 4.5: X-ray spectrum of the compact source. The solid line is the best-fit power law with pileup correction and the lower panel illustrates deviation of data points from this fit. Uncertainties are 1σ in number of counts.

PWN as was reasonably inferred from the *XMM* observation by Bamba et al.

Since in $\approx$ 12 hours the *Chandra* flux varied 25% we searched for variability in past observations. These were all of limited sensitivity but could show variability extremes. Table 3 lists imaging observations which have detected this remnant. We inspected the archival *Einstein* and *ROSAT* fields and, in all cases could distinguish the Head and Tail of the remnant but could not separate the point source in the Head from the diffuse emission. The diffuse and compact parts of the remnant are only well separated in *XMM* and *Chandra* observations. Indeed, the spatial resolution and low count rate in *Einstein* and *ROSAT* observations make it impossible to do this if the

Table IV.3. X-ray observations of DEM L241

Date	Spacecraft	Energy Range (keV)	Compact Source 0.5–5 keV Abs. Flux (10^{-13} erg cm^{-2} s^{-1})	Compact Source L_x 0.3-10 keV (10^{35} erg s^{-1})	Diffuse Absorbed 0.5-5 keV Head flux (10^{-13} erg cm^{-2} s^{-1})	Ref.
1979 Apr 10	*Einstein* IPC	0.15-4	-	-	4.1 ± 1.4	1
1979 Nov 5	*Einstein* HRI	0.15-4.5	-	-	5.4 ± 1.4	2
1991 Feb 14	*ROSAT* HRI	0.15-2.5	-	-	6.0 ± 1.6	3
1993 Jul 24	*ROSAT* PSPC	0.15-2.5	-	-	4.2 ± 0.8	
1995 Jul 9,17	*ROSAT* HRI	0.15-2.5	-	-	5.1 ± 1.0	4
2004 Dec 29	*XMM*	0.5-10		2.32 ± 0.14		5
2011 Feb 7	*Chandra*	0.3-10	3.71 ± 0.10	2.52 ± 0.07	4.42 ± 0.12	6
2011 Feb 8	*Chandra*	0.3-10	4.70 ± 0.12	3.19 ± 0.08	4.43 ± 0.12	7

[1]Long et al. 1981

[2]Mathewson et al. 1985

[3]Schmidtke et al. 1994

[4]Schmidtke et al. 1999

[5]Bamba et al. 2006

[6]this chapter

[7]this chapter

point source is no stronger than in our observation. In these past observations only 10-20% of the counts in the Head should be from the point source and total counts from the Head range from ∼30 to ∼200 with the higher rates from detectors with the lower spatial resolution. In all cases the counting rate was about the same from the Head and Tail regions as it is in the *Chandra* observation, so this is reassuring.

In order to compare observations of the diffuse source we have converted count rates to flux levels with PIMMS, assuming a thermal spectrum with $kT = 0.5$ keV and $N_H = 2 \times 10^{21}$ cm^{-2}. To avoid large absorption corrections at energies below 0.5 keV, we calculated the flux in the range 0.5 to 5.0 keV and these results are summarized in Table 3. Uncertainties are counting statistics only. The luminosity, L_X, of the

compact source is calculated for the *Chandra* range 0.3-10 keV. The agreement of past observations is good, as indeed it should be for the diffuse emission. Any variation of the point source less than a factor of $\sim$3 is undetectable in the *Einstein* and *ROSAT* data. The past observations of this remnant therefore show that there have been no major outbursts at these times.

We searched for regular pulsations in the *Chandra* data and found nothing significant. Since the ACIS instrument integrates for 3.2 s, the search was only valid for periods between 6.4 s and 6 h and the signal of 2500 counts limited the search to pulsed fraction above $\approx$ 20%. Bamba et al. searched *XMM* and ASCA data in the period range 0.15 - 500 s at about this same sensitivity with null result. A short period and/or a $\approx$10% pulse fraction is quite possible.

4.3.3 Optical/NIR

We have measured the optical spectrum of this star with the SAAO 1.9 m telescope at Sutherland, South Africa in October 2011 and April 2012. The spectrum from 2011 Oct 24 is shown in Figure 4.6. This spectrum is almost identical to that of Crampton et al., indicating no long-term spectral variability. The velocity we measure from the Balmer (mean of H-β and H-γ) absorption lines is 324$\pm$7 km s^{-1} so it is clearly in the LMC and an association with the remnant is possible. Further spectra on 2012 April 12 and 15 yielded velocities of 301 and 296 km s^{-1} respectively (and with similar uncertainties). These values are consistent with the Crampton et al. (1985) mean

value of 304 km s^{-1}, as well as the variability by 34 km s^{-1} that was noted then. The small velocity change noted between our April spectra are indicative of a long period system, likely tens of days or more.

IR photometry in the J, H and K_S wavebands of the optical counterpart was obtained during the month of November 2011 using the 1.4m IRSF telescope at SAAO's Sutherland observing station. These showed no significant variability to within 0.1 mag.

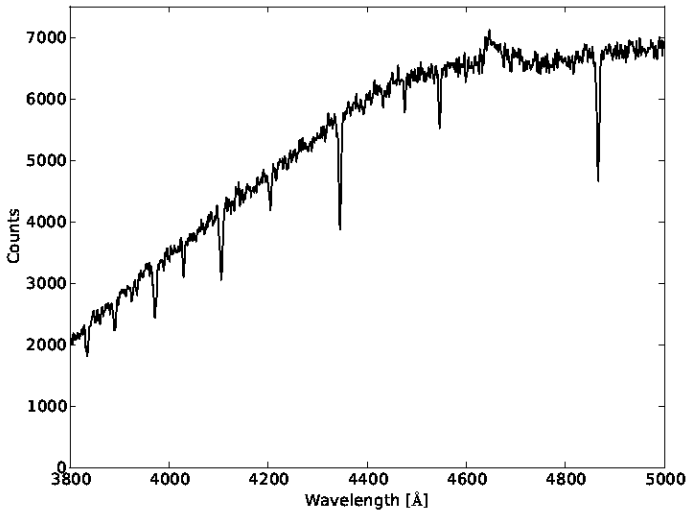

Figure 4.6: Spectrum of the O5III(f) counterpart of CXOU 053600.0-673507 taken with the SAAO 1.9m telescope. Absorption lines are from H and He. The emission feature is the Bowen blend, typical of very early O stars.

4.4 The Diffuse Emission

4.4.1 Radio Observations

Moderate-resolution radio observations of this area were made during surveys at 8.6- and 4.8-GHz (Dickel et al. 2005), at 1.4 GHz (Hughes et al. 2007), and at 843 MHz (Mauch et al. 2003). The best resolution is at 8.6 GHz with a half-power beam width of 20″. An overlay of the X-ray image on the 8.6 GHz radio contours is shown in Fig. 4.7. The X-ray emission has been smoothed with a 5-arcsecond Gaussian. The H II region is clearly delineated by the contours with its two brightest parts N59A on the west and N59B on the east as designated by Henize (1956). Because of the overlap with the bright H II region it is difficult to separate a possible contribution of the SNR to the radio emission. The rms noise should give a 5 sigma limit of about 1 mJy/beam but the contamination could make the limit a few mJy/beam. The fact that no radio emission appears to match with the X-ray emission is unusual. Most SNRs with significant X-ray emission are readily visible at radio wavelengths as well. Apparently the surrounding H II region complex masks the non-thermal emission from the SNR.

With the current resolution, any point radio source would be difficult to distinguish from the somewhat irregular background, but the absence of any feature at the position of the point source suggests that it would be less than a few mJy. For comparison, the X-ray only pulsar 0537-6910 in N157B is less than .06 mJy at 22 cm (Crawford et al. 1998) and PSR 0540-693 in the composite SNR of the same name

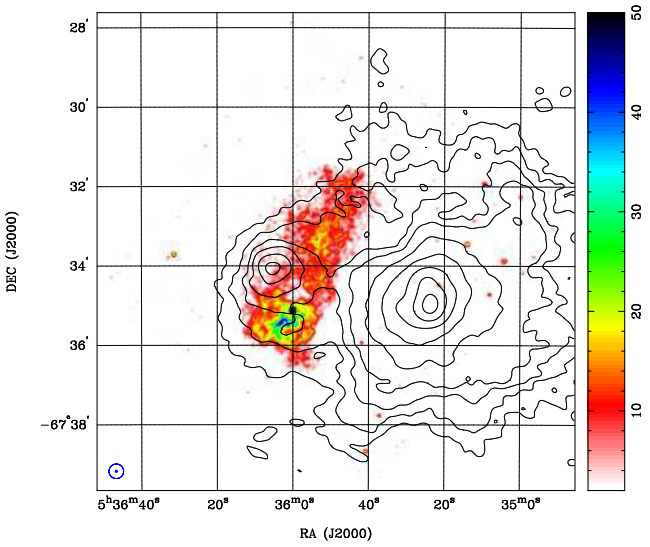

Figure 4.7: Contours of constant 3.5 cm radio surface brightness overlaid over the smoothed X-ray emission. The X-ray field is that of Figure 4.2 but with 5″ Gaussian smoothing. Radio contours are drawn at 2, 3, 4, 5, 7, 10, 20, 50 & 100 mJy/beam. The dot in the lower left represents the 5-arcsec resolution of the smoothed X-ray image and the surrounding circle is the 20-arcsec beam width at 3.5 cm. The two radio maxima are from the bright H II regions seen in Figure 4.1.

is 0.4 mJy at 640 MHz. N206 is a shell-like radio SNR with a radio jet-like feature with an X-ray point source at the tip, but no radio point source or pulsar at $< .02$ mJy (Williams et al. 2005). Thus the radio limit on the point X-ray source is not very significant or unexpected.

Another way to distinguish between the thermal emission from H II regions and the non-thermal synchrotron emission from SNRs is the radio spectrum. H II regions have a nearly flat spectrum with a slope, or spectral index, near 0 while PWN have a modest decrease in brightness as frequency increases with an index of about -0.2 to -0.3. Shell SNRs have average spectral index slopes of -0.5 with young remnants

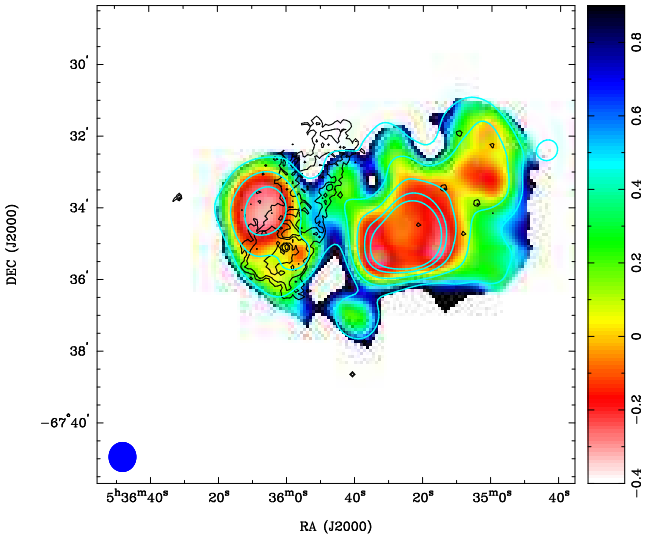

Figure 4.8: Color indicates the radio spectral index with red showing the flat spectrum characteristic of thermal emission. There is no indication of the steeper spectrum expected from the shell of a supernova remnant. Smoothed contours of constant 21.7 cm radio surface brightness are overlaid and drawn at 10, 20, 40, 70, & 100 mJy/beam where the 48.5"x45" radio beam is indicated at the bottom left of the figure. Black contours show the X-ray surface brightness at levels of 0.25, 0.5, 1, 2.5, and 12 counts arcsecond^{-2}.

being steeper and old ones flatter. Figure 4.8 shows a four-wavelength radio spectral index map of the entire region. Production of this image required convolution of all the data to the 48.5 x 45.0 arcsec resolution of the 36-cm image. Obviously, part of the X-ray Tail is missing in the radio but other areas could contain some synchrotron emission from a PWN or very old SNR in addition to the thermal emission from the H II regions. From the spectral index map, we cannot distinguish the separation of various components.

4.4.2 Optical Observations

For comparison with optical wavelengths, we used images from the Magellanic Cloud Emission Line Survey (MCELS; Smith 1999). These images were taken at the UM/CTIO Curtis Schmidt telescope at Cerro Tololo Inter-American Observatory (CTIO). The detector, a Tek 2048 x 2048 CCD with 24 micron pixels, gave a scale of 2.3 arcsec per pixel and a resulting angular resolution of approximately 2.6 arcsec. The narrow band images were taken with filters centered on the [O III] (5007 Å, FWHM = 40 Å), H-alpha (6563 Å, FWHM = 30 Å), and [S II] (6724 Å, FWHM = 50 Å) emission lines. The image shown in Figure 4.1 has been reduced using the IRAF software package for bias subtraction and flat-field correction, and the astrometry was derived based on the HST Guide Star and USNO-A catalogs. This image, however, has not been flux-calibrated or continuum-subtracted.

Because of the presence of the bright H II region, a good way to depict the SNR

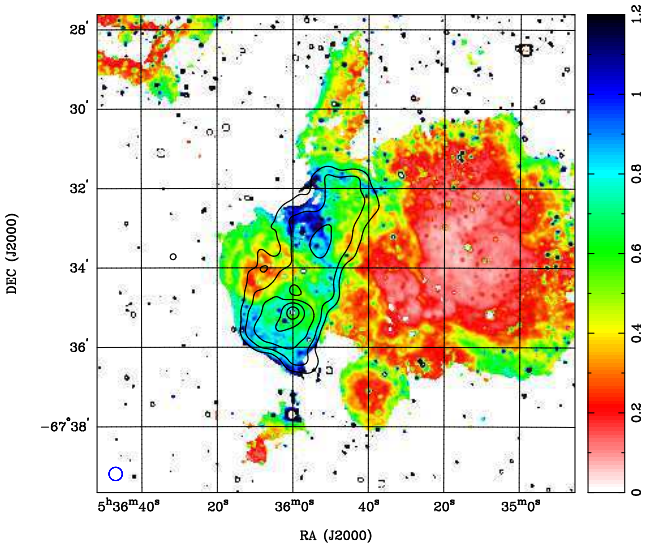

Figure 4.9: Contours of constant X-ray surface brightness overlaid on the ratio of [S II] to Balmer optical emission. X-ray data have been smoothed with a 20″ Gaussian and X-ray contours are drawn at levels of 0.12, 0.25, 0.5, 1 & 2 counts arcsecond^{-2}.

is to show the [S II]/Hα ratio. The [S II] doublet at 671.7 and 673.1 nm is enhanced by shocked material so any region with an [S II]/Hα ratio greater than about 0.5 is considered a supernova remnant. In Fig. 4.9 we show the ratio superimposed on contours of the X-ray emission. There is clearly a good correlation except on the eastern edge where the bright H II-region component N59B overwhelms emission from the remnant.

No X-rays are observed from the outer shock traced by the [S II] filaments. This implies that the temperature of hot gas in the shock is $< 8 \times 10^5$ K. The Sedov model then, can be used to estimate an age limit. Assuming $E_0 = 10^{51}$ ergs and using the densities given in Table 5, we derive an age of $> 5 - 7 \times 10^4$ years.

4.4.3 X-rays

There are two major parts to this object. The X-ray spectra of the Head and the Tail are sufficiently similar to indicate that they are parts of the same remnant rather than two separate objects and we will so treat them. Data were extracted from the 3 regions outlined in Figure 4.3 - the Head or S region, the bright NW strip which accounts for 80% of the emission from the Tail and a NE strip where there is fainter emission which might be indicative of a shock. After background subtraction the number of events in these regions was: S - 7960, NW - 4640 and NE - 1020. The first two regions contain enough events to support an interesting spectral analysis but the faint NE region yields less information. Background was taken from large source-free regions northeast and southwest of the remnant and was 35% of the remnant signal in the S region, 85% of the NW signal and 200% of the NE signal. The spectra of these regions are shown in Fig 4.10. The visually distinct spectra of the S and NW regions can be explained almost entirely by differences in absorption of the emitted X-rays. This can be seen by inspection of the softest emission and is greatest in the region between Head and Tail. The visual gap in the X-ray image which separates the Head from the Tail is most prominent in the softest energy band and is caused by absorbing material. This is not surprising considering the complex surrounding environment. The spectra of the bright structure just south of the O star and the surrounding outer part of the Head were examined separately and were, within uncertainties, the same. The bright structure is therefore plausibly explained as a density enhancement within

the SNR or an extension of the remnant structure along the line of sight.

We used the *xsvpshock* model, which accounts for non-equilibrium ionization in a one-dimensional shock, to fit the NW region which shows least absorption. Metal abundances were fixed at 0.3 solar and then allowed to vary to fit the data. It was necessary to vary only O, Ne, Mg, and Fe. We then fit the S and NE regions with the same spectrum allowing only the ISM absorption and timescale parameters to vary. Best-fit parameters are listed in Table 4. The NW fit is excellent, The S fit is good and the NE fit as good as any that can be achieved with the limited number of events. These fits are shown in Figure 4.10. The difference between fits of the S and NW regions is entirely due to different absorption of the O, Ne and Fe emission lines. The fit to the NE region requires a lesser value of the ionization timescale (τ_μ). Since the NE region comprises the outer part of the expanding remnant, this is expected.

The formal 1σ uncertainties in the S and NW spectral parameters due to counting statistics are $\approx 15\%$ for the absorption (N_H), $< 10\%$ for the temperature (kT), $\sim 40\%$ for the abundances and $\sim 50\%$ for the ionization timescale (τ_μ). The statistical uncertainties of the data points, however, allow acceptable fits over a large range of parameters, e.g. the temperature can be varied by $\pm$ 50% and reasonable fits can be obtained with small changes in abundances (although the Fe abundance is more sensitive than the lighter elements). Table 4 lists *CIAO/SHERPA* best-fit spectral parameters for the *xsvpshock* and the equilibrium *xsvmekal* models.

Table IV.4. Diffuse source spectral fits

Region	NW Tail	S Head	NE Tail	NW Tail	S Head
Model	*xsvpshock*			*xsvmekal*	
Reduced χ^2	0.79	1.05	1.38	0.91	1.08
N_H	0.14	0.37	0.17	0.22	0.29
kT		0.52		0.33	0.41
O		1.9		1.2	2.9
Ne		3.2		1.3	4.9
Mg		1.7		1.0	2.3
Fe		0.4		0.2	0.35
τ_μ	7×10^{11}	7×10^{11}	2×10^{11}	-	-

4.5 Discussion

4.5.1 Nature of compact object

The variability excludes an unresolved PWN such as that surrounding the Vela Pulsar. Furthermore the Vela PWN has $L_x = 2 \times 10^{33}$ ergs s^{-1}, considerably less than observed here. The compact object is too bright to be a Cas A-type CCO (Central Compact Object with $L_x = 10^{33} - 10^{34}$ ergs s^{-1}). The luminosity is compatible with an AXP (Anomalous X-ray Pulsar with $L_x = 10^{35} - 10^{36}$ ergs s^{-1}) but the spectrum is harder than that of most AXP (McGill Pulsar Group 2012). The hard spectrum suggests an accretion-powered binary which, comprising an O star and a neutron star, would be a High-Mass X-ray Binary (HMXB). This is unexpected. Only two other X-ray binaries have been discovered within observable SNR – SS 433, with a B or A giant primary star, within the galactic remnant W50 and recently, a Be X-ray pulsar

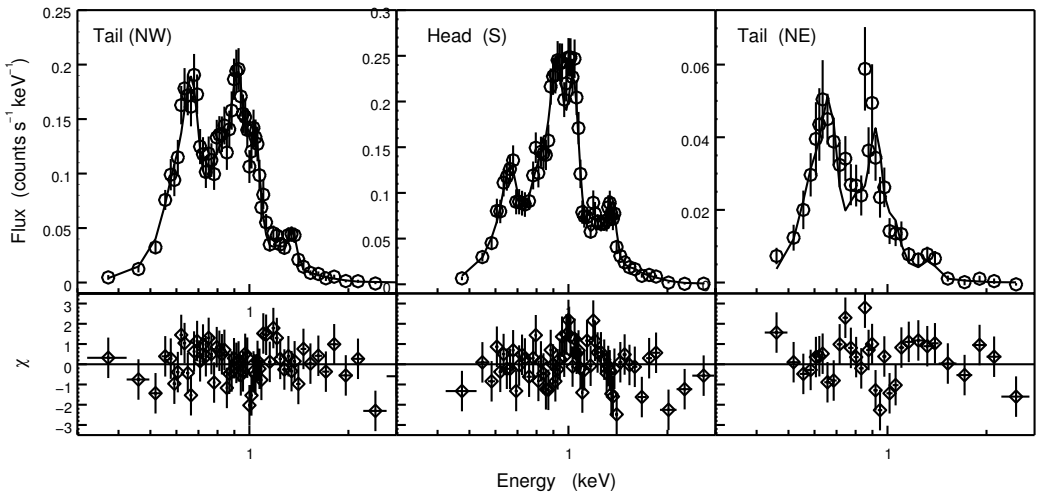

Figure 4.10: X-ray spectrum of the three diffuse regions. The lower panel illustrates deviation of data points from the best fit *xsvpshock model* shown by the solid lines. A linear scale is used to show the large apparent differences between spectra from the three regions. Only the absorption and timescale parameters vary from region to region. Prominent emission lines are O at 0.67 keV, Ne and Fe at $\approx$ 1 kev, and Mg at 1.32 keV.

system, SXP 1062, within a faint Small-Magellanic-Cloud remnant (Hénault-Brunet et al., 2012).

Although we have no evidence other than location that the O star under discussion and the X-ray source form a binary system, we suspect that the object within DEM L241 is the third HMXB to be found within a SNR. The compact object, in this HMXB, if a neutron star, would accrete material from the O-star wind and changes in luminosity would be caused by changes in the density of the wind. Scaling from the HMXB Cen X-3, the moderate luminosity and lack of observed outbursts imply (very roughly) a separation of $\sim$ 1 AU and an orbital period of weeks. At the moment this is speculation but the velocity of the O-star has indeed been observed to vary.

No regular pulsation in the X-rays have been found but the observations were not sensitive to pulsed fractions below $\sim 20\%$.

The fact that the supernova precursor must have been more massive than the O-star companion implies a precursor mass of 25, perhaps 40 $M_{\odot}$, thought to be the mass necessary for collapse to a black hole. It is therefore possible that the compact object, which we have assumed to be a neutron star, could actually be a black hole. The X-ray luminosity, however, is unusual for a black hole. Known black hole binaries are either bright with $L_x \geq 10^{37}$ erg s^{-1} or are transient systems in quiescence with $L_X < 10^{33}$ erg s^{-1} (Remillard and McClintock 2006).

However, the HMXB in DEM L241 has a luminosity ($2/times10^{35}$ erg s^{-1}), intermediate between these extremes. Interestingly, this is similar to the luminosity of SS433. While there is as yet no direct dynamical measurement of the compact object mass in SS433, all the indirect evidence strongly supports it being a $\sim$15 $M_{\odot}$ black hole accreting at extremely high mass transfer rates from a highly evolved supergiant primary (see e.g. Blundell et al. 2008). The reason that it's X-ray luminosity is so low ($\sim 10^{35}$ erg s^{-1}) is that it is observed at high inclination (it is eclipsing), and hence we only receive X-rays scattered from the surrounding material into our line of sight. i.e. it is an "accretion disc corona" system.

As discussed earlier, there is marginal evidence that L_x of the HMXB in DEM L241 does not vary much, but we consider it unlikely that it too would be a high inclination system. Consequently, a black hole is certainly possible but we have no

strong indication that this might be the case. A measure of the velocity variation of the O5III(f) companion would provide a test of this hypothesis. This remnant could become the first example of a remnant known to be created by stellar collapse to a black hole.

4.5.2 Nature of the remnant

Throughout this discussion it is assumed that the precursor star was originally bound to the O5III(f) star. After the SN, the compact remnant of this remained bound to the O star to form the present HMXB. The explosion itself probably determined the size and temperature of the remnant. The binary environment of the precursor may have shaped the remnant morphology.

The X-ray morphology of the SNR looks like that of a PWN with an extended elliptical structure showing no obvious shell and a point X-ray source near one end. However, all diffuse emission, including that close to the point source, is well fit with a thermal spectrum. There is no evidence for a power law component although a 10% contribution cannot be excluded. The X-ray extent along the major axis of about 80 pc makes the object one of the larger of the known SNR. The SN may have exploded between the two major H II regions and the expansion was impeded in the east-west direction. However, although the SNR and the H II region complex do appear coincident in the sky there is no indication in their structures that they have interacted so they could be at different distances along the line of sight.

The *vpshock* fits indicate an age of $\tau_\mu/n_e \sim 7\times10^{11}/0.14-0.27$ s $= 0.8-1.6\times10^5$ yr, about twice the lower limit estimated using the Sedov model. This age is old for a radio SNR as the expanding shock will have slowed sufficiently to reduce the shock acceleration of relativistic particles that create the radio synchrotron emission. Thus the age can explain both the relatively flat radio spectral index and the weak radio emission in general.

Since the plasma is close to equilibrium we also fit the X-ray spectra with the *xsvmekal* equilibrium model. Table 4 gives the best fit result of this model to the S and NW spectra. In this case, the two spectra have been fit separately. The S region, the Head surrounding the compact object requires somewhat higher temperature and abundances than the NW Tail region. Absorption is still higher in the S than in the NW region.

Although there is considerable uncertainty in the spectral fit parameters and in the volumes used for the three regions, enhanced abundances and derived densities indicate that we are seeing radiation from supernova debris above that from the normal ISM in the Magellanic Clouds. Table 5 gives the plasma densities and masses calculated from the *vpshock* results of Table 4. The excess of O, Ne, and Mg above that expected is 2.5, 0.8,and 0.15 $M_\odot$, indicating the explosion of a massive star. Woosley and Weaver (1995) have calculated the masses of elements ejected from explosions of massive stars. This amount of O can come from a precursor with mass $> 25M_\odot$ and the Ne from a precursor with mass $> 40M_\odot$. Since there is variation in the different

Table IV.5. Properties of the remnant

Region	F_X erg cm^{-2} s^{-1}	L_X erg s^{-1}	Volume cm^3	n_e cm^{-3}	Mass $M_\odot$	E_{th} erg
S Head	4.17×10^{-13}	6.10×10^{35}	2.8×10^{59}	0.27	83	1.9×10^{50}
NW Tail	3.86×10^{-13}	2.36×10^{35}	4.1×10^{59}	0.14	61	1.1×10^{50}
NE Tail	0.83×10^{-13}	0.68×10^{35}	1.6×10^{59}	0.12	21	0.4×10^{50}
Total SNR	-	9.14×10^{35}	8.5×10^{59}	-	165	3.4×10^{50}

Woosley & Weaver models and uncertainty in our measured abundances, we can only conclude that the precursor was massive. Since it evolved first, it should have been more massive than the present O5III(f) star, so this is expected. Martins et al. (2005) give the mass of an isolated O5III(f) star as about 40 $M_\odot$. However, Rappaport & Joss (1983) show evidence that the companion stars in HMXBs are "undermassive for their luminosity", so a precursor mass estimate of $> 25 M_\odot$ is more conservative.

The remnant parameters derived here differ somewhat from those obtained from the *XMM* observation by Bamba et al. (2006). Our X-ray flux and luminosity is 30% higher because we use a different energy band. Our total mass is 30% lower because we assume different volumes for the emitting regions. Bamba et al. assume ellipsoidal volumes for Head and Tail whereas we use cylindrical volumes with different dimensions. The *Chandra* best-fit spectra have higher temperature and greater enrichment. Remarkably, the total thermal energy content is the same for the two analyses.

The elongated structure may be due to a "blowout" to a lower density region in the north. If so, this was a major event. The Tail now has twice the volume of the

Head and contains 40% of the thermal energy of the hot gas. On the other hand, perhaps the unusual elongation of the remnant is associated with the unusual central source which is quite likely a HMXB. The massive binary might have produced a disk of material which channeled the ejecta into two lobes. Or, the precursor star itself could have been a Wolf-Rayet star with strong wind which shaped a cavity now filled by the remnant. Or, rotation of the precursor could have produced an asymmetrical explosion.

4.5.3 Comparison with W50/SS433

There is an interesting parallel with the morphology of the Galactic remnant W50 which is also large and elongated with dimension 95×200 pc (at a distance of 5.5 kpc, Lockman et al. (2007). The binary SS 433 lies at the center of W50 and produces opposing relativistic jets which have inflated and elongated the remnant in the EW direction. The optical manifestation of these jets is spectacular (Margon et al. 1980). SS 433 is an unresolved X-ray source with luminosity 3×10^{35} ergs s^{-1}, the same as that of the DEM L241 source.

DEM L241, with dimension 32×77 pc, is also elongated but only about one third the size of W50. From the O star to the northern end of DEM L241 is 57 pc, about half the length of 120 pc for the longer arm of W50. Perhaps the Tail of DEM L241 was inflated by a single northern jet and the structure south of the O star is due to energy deposited by the oppositely-directed jet. Since we see no other evidence for

jets, this probably happened in the past and is no longer operating. The lesser size of DEM L241 also indicates a weaker jet and/or a younger remnant.

Despite intensive searches, no other examples of SS 433/W50 systems have been found. Here in the LMC is a system with similarities that suggest further investigation might be worthwhile.

4.5.4 Magellanic Cloud inventory

As a matter of interest, we list here the compact objects now known to be associated with Magellanic Cloud supernova remnants. The Large and Small Magellanic Clouds (LMC and SMC) contain $\sim$ 60 remnants. About 45 of these are known to emit X-rays [Smith (web page, 2005), Williams et al. (2000), Inoue, Koyama, and Tanaka (1983), Filipovic et al. (1998)]. Thirty-four have so far been observed by *Chandra* and the results may be viewed in the online catalog at http://hea-www.cfa.harvard.edu/ChandraSNR/. Structure of the brighter remnants has been well-resolved with moderate observing times and much detail is visible. One can see shock waves, interior structure, clumpy material, central objects, and pulsar-wind nebulae. *Chandra* data have been used to compile Table 6, an inventory of X-ray emitting compact objects and PWN within Magellanic Cloud SNRs. Diffuse thermal radiation from the shells or interiors has not been included. Faint unresolved sources, for which no pulsations have been detected, could contain a contribution from a small PWN so the luminosities are listed under the header "PSR & PWN". All luminosities

Table IV.6. Luminosity of Magellanic Cloud compact objects and PWNe

Remnant	PSR or CCO	Period (s)	L_X PSR and PWN (erg s^{-1})	L_X Compact (erg s^{-1})	L_X Pulsed (erg s^{-1})	Ref.
SNR 0540-693	B0540-69	0.050	2.1×10^{37}	1.7×10^{37}	0.4×10^{37}	(1)
N157B	PSR J053747.3-691020	0.016	4.4×10^{36}	7×10^{35}	3×10^{35}	(2)
N49	SGR J052600.8-660436	8.04	1.0×10^{36}	1.0×10^{36}	$< 10^{35}$?	(3)
DEM L241	CXOU J053600.0-673507	-	-	2×10^{35}	-	this chaper
SNR 0453-685	-	-	6×10^{34}	-	-	(4)
DEM L316B	-	-	$\approx 5 \times 10^{34}$	-		(5)
N23	J050552.3-680141	-	-	8×10^{33}	-	(6)
SNR J0047.2-7308	J004719.7-730823	-	$\sim 3 \times 10^{33}$		-	(7)
N206	-	-	3×10^{33}	$< 1.5 \times 10^{33}$	-	(8)
SNR J0127.7-7333	SXP 1062	1062	-	7×10^{35}	1.4×10^{35}	(9)

(1) Kaaret et al. 2001 (2) Wang et al. 2001 (3) Kaplan 2002 (4) Gaensler et al. 2003 (5) Williams & Chu 2005 (6) Hughes et al. 2006 (7) Seward et al. 2012 (8) Williams et al. 2005 (9) Hénault-Brunet 2011

have been corrected to the 0.5-10 keV range. Ten of the 35 Magellanic Cloud SNRs observed by *Chandra* have PWN or compact objects. The luminosity range is a factor of 10^4 and there is great variety of type; 1 SGR, 2 rotation-powered PSR/PWN, 1 CCO, 2 PWN with no associated compact object, 2 XRB (including this observation), and 2 unclassified faint objects.

4.6 Conclusions

This is an interesting supernova remnant, larger and more elongated than most. The absence of X-ray emission from the outer shock, the X-ray spectra, and the size all indicate an older remnant. Because of its age and location close to a strong H II region, radio emission is weak and undetectable. It contains a compact object with an O-star optical counterpart which is unusual for a supernova remnant. No non-thermal X-rays, as might originate in a PWN, are detected from the immediate vicinity of

this source and the source luminosity and spectrum are consistent with that expected from a HMXB. The velocity of the O-star was observed to vary and a long period is suspected.

The diffuse X-ray spectrum from the remnant interior is enriched in O, Ne, and Mg. This enrichment and the more-slowly evolving O-star companion imply that the supernova precursor star had a mass of $> 25M_{\odot}$. We note that the elongated envelope and the structure close to the compact source might have been formed by an SS 433-type pair of jets but there is no indication of these in the optical spectrum.

Chapter V

ON THE NATURE OF THE HIGH-MASS X-RAY BINARY AT THE CENTER OF THE SUPERNOVA REMNANT IN DEM L241

In work I am leading, and which is being done in collaboration with Phil Charles, Fred Seward, Varun Bhalerao, Andry Rajoelimanana, and Keivan Stassun, I present here an in-progress analysis of spectroscopic observations of a recently discovered HMXB found in the Large Magellanic Cloud (LMC) and within a supernova remnant (SNR).

X-ray observations of the supernova remnant SNR 0536–67.6 in the H II region DEM L241 reveal elongated diffuse X-ray emission and a hard X-ray point source, named CXOU J053600.0–673507, centered in its SE region. It was previously thought that this source was an unresolved neutron star/pulsar wind nebula (PWN) system; however follow-up X-ray observations found no evidence of a PWN but confirmed the presence of the bright point-like hard X-ray source. Because of its bright optical counterpart and its X-ray variability, it has been suggested that this point source is an accretion-powered compact binary. We present here an analysis of optical spectra with the aim of constraining the orbital parameters of the putative binary. We found that the best explanation for the observed L_X and optical properties is a high mass X-ray binary (HMXB) with either a neutron star or black hole primary component undergoing wind accretion from a massive early-type donor. Our results are consistent

with previous work which suggested an orbital period $\gtrsim$ ten days. We propose a lower limit to the compact object mass of 2–3 $M_{\odot}$.

5.1 Background

Massive stars end their lives in core-collapse supernovae, leaving behind a neutron star (NS) or black hole (BH) remnant. Significant progress has been made in recent years in both theoretical and observational understanding of this process (Janka, 2012; Fryer, 2013). Nevertheless, several questions still remain unsolved: (1) What is the relation between the progenitor mass and remnant mass? (2) How (a)symmetric is the explosion? (3) How do progenitor properties affect the nature and outcome of the explosion? Addressing these questions demands knowledge of all three stages of the supernova: the progenitor, the explosion, and the remnant. But in many cases, the quest is reduced to a forensic investigation: understanding the circumstances of the star's death by gathering clues from the supernova remnant (SNR) and its environment. Sparse knowledge about the progenitor may be available in the form of detections in archival images. Some further information can come from the circumstellar/interstellar medium, nebular spectra of the ejecta, light echoes, etc. (see for example Tomasella et al., 2013; Eldridge et al., 2013).

This scenario is more complex when the supernova occurs as part of a massive binary system. In fact, massive stars are found more often as binaries or multiples within large, complex star-forming regions. The components of such a binary therefore

have essentially the same age and metallicity. The more massive component explodes first as a supernova, leaving behind a compact object (NS/BH) in orbit with the now more massive secondary (OB) star that is significantly enhanced as a result of mass transfer during the final stages of the pre-supernova primary star's evolution. Many such high mass X-ray binaries (HMXBs) are known, but very few are associated with discernible SNRs (Liu et al., 2006). In these cases, we can study the secondary star in great detail in order to infer the properties of its sibling, the supernova progenitor.

The relatively short lifetimes of SNRs (before they merge into the ambient medium) means that there are very few X-ray binaries embedded in or near the SNR presumably associated with the creation of the compact object. That rarity is highlighted by the exotic properties of the two well-known examples of the breed, namely SS433 (Margon, 1984) and Cir X-1 (Haynes et al., 1986). Of these two, one (SS433) is almost certainly a BH orbiting a more massive, but highly evolved early-type companion (Blundell, Bowler, and Schmidtobreick, 2008), whereas the other is a NS (it bursts) in an eccentric orbit about a more massive donor (Tennant, Fabian, and Shafer, 1986). Searches for further examples have been frustratingly unsuccessful, but recent *Chandra* observations of the LMC (Seward et al., 2012) have revealed another candidate HMXB associated with the SNR in DEM L241, which is the subject of this paper.

A soft X-ray imaging survey of the Large Magellanic Cloud (LMC; $D = 50$ kpc, Feast, 1999) was first undertaken in 1979 with the *Einstein* Observatory by Long et al. (1981b). Subsequent analyses (Cowley et al., 1984) identified the diffuse emission at

the location of the suspected X-ray point source CAL60 (Long et al., 1981b), and confirmed this diffuse emission to be a SNR (Mathewson et al., 1985). Crampton et al. (1985) measured the spectrum of the optical counterpart of CAL60 and determined its spectral type to be O5III(f) according to the classification scheme outlined in Walborn (1971).

Since the initial detection by *Einstein*, there have been further X-ray detections of this source by *ROSAT* (Williams et al., 1999), by *XMM-Newton* (Bamba et al., 2006), and by *Chandra* (Seward et al., 2012). The *XMM-Newton* observations were the first detailed images of the SNR, revealing an elongated and diffuse structure along with a bright, hard point-like X-ray source (Bamba et al., 2006). The proximity of this point-like source to the brightest region of the SNR hints at an association between the two sources. The X-ray morphology of the SNR and the location of the point-like source strongly suggested the presence of a rotation-powered neutron star/pulsar wind nebula (PWN) system (e.g., Gaensler et al., 2003); however, the *XMM-Newton* observations could not resolve the PWN and follow-up *Chandra* observations were needed to confirm the existence of the putative PWN. *Chandra* observations of the SNR confirmed the presence of the internal hard point source; however these observations showed the spectrum of the diffuse component to be thermal, contradicting earlier interpretations of the system as a PWN (Seward et al., 2012).

More precisely, CAL60 contains both the X-ray point source and diffuse emission. Hereafter we adopt CXOU J053600.0–673507 (Seward et al., 2012) as the name of the

X-ray point source in CAL60 and use J0536 as shorthand for the remainder of this paper. J0536 is either known by or associated with the following other names in the literature: CAL60 (Long et al., 1981b), DEM L241 (Davies et al., 1976), SNR 0536–67.6 (Mathewson et al., 1985), SNR 0535–67.5 (Seward et al., 2012), and XMMU J053559.3–673509 (Bamba et al., 2006).

J0536 is very bright at optical wavelengths and is also extremely hot ($V = 13.46$, $U-B = -1.04$, $B-V = -0.17$, $V-R = -0.92$, $\log(\mathrm{T_{eff}}) = 4.595$; Massey, 2002) with both Balmer and He II spectral lines in absorption. J0536 itself has X-ray luminosity $L_X \sim 10^{35}$ erg/s (Bamba et al., 2006; Seward et al., 2012) at the distance to the LMC.

Despite knowing these properties, J0536 is still open to a rich variety of interpretations. Prior to the *Chandra* observations of J0536, there was already considerable uncertainty about the nature of this source. The bright optical counterpart is suggestive of an accreting compact binary, but the intermediate X-ray luminosity hints at a colliding-winds binary (CWB). Is J0536 a CWB, similar to the system Wack 2134 (Mereghetti et al., 1994; Reig, 1999), or rather a HMXB undergoing wind-fed accretion onto a BH as in Cyg X-1 (e.g., Gies and Bolton, 1986), but with a lower $\dot{M}$ to account for the much lower L_X?

If J0536 is determined to contain a HMXB, then as an O5III(f) star the companion would be the earliest yet found in a HMXB (Liu, van Paradijs, and van den Heuvel, 2006). Therefore, we could be viewing the low-energy end of something more extreme

and similar to the γ-ray binary LS 5039 (Aharonian et al., 2005), in which a portion of the intense ultraviolet emission of the massive star is scattered to γ-ray energies by the relativistic particles of the pulsar wind (e.g., Mirabel, 2012). On the other hand, if J0536 is found to contain a CWB, then it would be amongst the highest L_X yet seen from such systems. Either of these interpretations would make J0536 a remarkable X-ray source worthy of further investigation.

To resolve the debate over the nature of this very interesting system, we conducted a spectral analysis and radial velocity study of the optical counterpart of J0536 to constrain any periodicities that may be exhibited by J0536, and if present, use these variations to constrain the system parameters.

5.2 Observations and Data Reduction

We observed J0536 with the SITe CCD Imaging Spectrograph of the 1.9-meter telescope at the South African Astronomical Observatory (SAAO) during the period 16 November 2012 – 1 January 2013. A total of 43 spectra were recorded with 900–1800 s integration times using a slit width of 1.05″–1.50″. Because we expect the orbital period to be up to several tens of days (Seward et al., 2012), we combined the spectra to produce one average spectrum for each night. We used grating #4 (Kilkenny and Worters, 2012) on 11 nights, which provided wavelength coverage roughly in the range $\lambda\lambda$4150–4974 and a dispersion of $\sim$0.5 Å pixel^{-1}. Our wavelength range enables us to measure several Balmer lines in absorption. A slightly

different grating angle was used for about half of the spectra, extending the wavelength coverage (down to 4093Å) to allow for measurement of the Hδ absorption line as well.

We used the IRAF package to perform the standard reduction procedures (e.g., cosmic-ray removal, wavelength calibration, background subtraction, etc.) CuAr comparison arcs were obtained both before and after science exposures in order to calibrate the wavelength scale.

5.3 Results

Almost nothing was known previously about the orbital parameters of the putative HMXB in J0536, as neither the orbital period ($P_{\rm orb}$) nor the mass of its compact object (M_X) had yet been measured either photometrically or kinematically. By measuring $P_{\rm orb}$ and the amplitude of the variation in the radial velocities of lines in the spectra ($K_{\rm opt}$), we can infer M_X once the mass function has been determined.

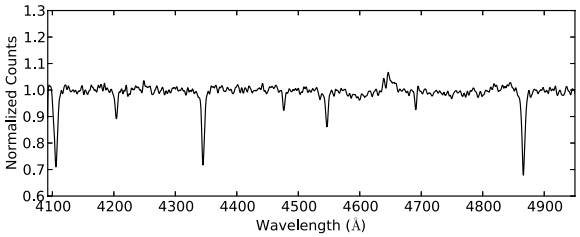

Figure 5.1: Continuum-normalized composite spectrum of CAL60/J0536 taken on the first night of observations with the SAAO 1.9-m telescope. He I 4471; He II 4200, 4541, and 4686; and the Balmer lines are all found in absorption. There is a bit of emission in the wings of the He II 4686 line and a prominent Bowen emission feature ($\lambda\lambda$4640–4660) due to fluorescence of X-rays from the central source.

Our analysis constrains $K_{\rm opt}$ and $P_{\rm orb}$, which allows us to place a lower limit on M_X; however, we know the spectral type of the companion and this can help us to constrain M_X further. Figure 5.1 is the optical spectrum of J0536, which shows Balmer and prominent helium lines in absorption, indicating the presence of an early O-type donor star. We determined the heliocentric velocities of the Hβ, Hγ (and when possible Hδ), as well as the He I 4471 and He II 4200, 4541, and 4686 absorption lines via cross-correlation with a reference spectrum. The heliocentric velocities of the Balmer lines (Fig. 5.2) suggest a variation on a time-scale of $\sim$ 50-d, consistent with the earlier data reported in Seward et al. (2012). The amplitude of the variation of the Balmer line velocities is $K_{\rm opt} \sim 30$ km s^{-1}.

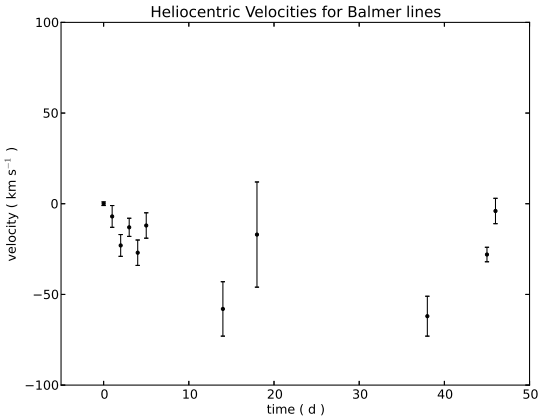

Figure 5.2: Heliocentric velocities of all the Balmer lines, determined via cross-correlation of the spectra.

In order to check for signs of variability in the spectral features, we trail the spectra in sequential order in Figure 5.3 which revealed what could to be a periodic evolution of the He II 4686 absorption feature during the course of our observations. The He II 4686 absorption line is of moderate depth at the start of observations, then gradually shrinks until it's consistent with the continuum, then grows in depth, and finally shrinks toward the end of the observing run. It's possible that strong emission at 4686Å by the He II in the accretion disk is "filling in" the absorption line from the donor, and therefore the varying depth of the absorption line could be either intimately tied to the orbital motion of the system, or (more likely) tied to the variable accretion.

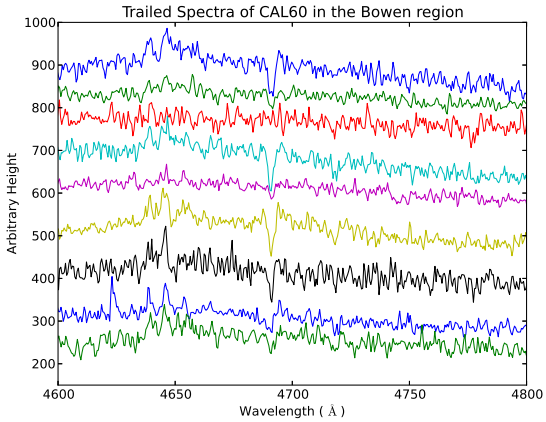

Figure 5.3: Un-normalized trailed spectra of J0536 in the Bowen region. Note the varying depth of the He II 4686 absorption feature.

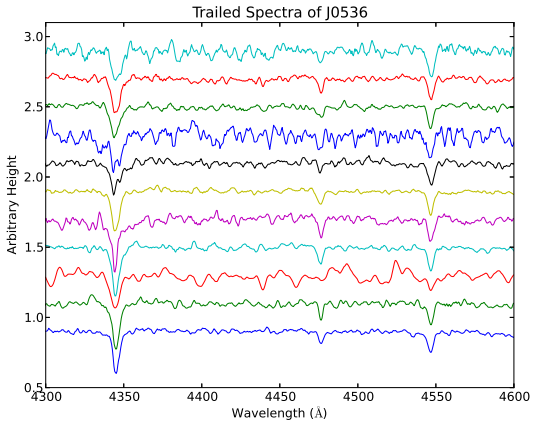

Figure 5.4: Continuum-normalized, trailed spectra of J0536.

5.4 Discussion

Yet another possible explanation of the X-ray emission in J0536 is that the system is not a HMXB at all, but rather a CWB consisting of, for example a Wolf-Rayet (WR) star and an O star (e.g., Mereghetti et al., 1994; Reig, 1999, in the case of Wack 2134), or a pair of O-type stars both having strong wind emission which collides to form a shock that produces X-rays. In the case of J0536, we can safely rule out a CWB containing a WR star since the spectra show no evidence of the presence of a WR-type star. Furthermore, the luminosity of observed CWB systems (e.g., W140; Pollock et al., 2005) is still less than that of J0536 typically by an order of magnitude. This makes the case for J0536 as a HMXB more compelling.

5.4.1 Comparing J0536 with other High Mass X-ray Binaries

The X-ray emission in HMXBs is driven by mass transfer between the binary components. Two key mechanisms for mass transfer in HMXBs are Roche-lobe overflow and accretion from a stellar wind; however, it has been suggested that these are two extremes of a continuum (Blondin and Owen, 1997), rather than mutually exclusive classes. Such mass transfer could be responsible for the X-ray emission in J0536, and it might be useful to compare it with similar HMXBs to try and pin down the nature of this source (see Table V.1). We discuss the possible interpretations of J0536 in terms of these HMXBs below.

5.4.1.1 SS433 and LS 5039

Consider the microquasar SS433 and its surrounding nebula, W50. J0536 is a HMXB in a SNR which could have formed as in the scenario discussed above. Having an environment akin to the SS433/W50 system, as well as a very similar L_X and their possibly comparable orbital periods, it is natural to assume that they could be related; however, the spectral types of their donor companions are quite different. The BH in SS433 is likely embedded in a common envelope with the evolving donor, leading to large outflows and hence supergiant temperatures, affecting the classification of the companion and causing it to appear to be of later type. Still, if the inclination in J0536 is near 90° the intrinsic X-ray luminosity could be significantly higher, just like in SS433, depending on the structure of the accretion disk. If the compact object is a

black hole is a microquasar, the γ-rays can be produced in the corona of the accretion disk, or at the termination shock of the relativistic jet with the interstellar medium (Casares et al., 2005; Dubus, 2013).

The binary system LS 5039 consists of a compact object and a massive star known to emit photons in a broad frequency range, from radio to very-high-energy (up to TeV) γ-rays (Aharonian et al., 2005), and thus is referred to as a "γ-ray binary." But LS 5039, and each one of the handful of confirmed γ-ray binaries, is easily overlooked at other wavelengths (Dubus, 2013). LS 5039 (all γ-ray binaries) have O or Be star companions that can emit powerful radiation-driven winds. J0536 has the earliest O companion yet seen in a HMXB and could itself be a γ-ray source, accelerating particles to MeV to TeV energies in the interaction between stellar wind of the O companion and the compact object.

5.4.1.2 Cyg X-1 and LMC X-1

Cygnus X-1 is one of the most thoroughly studied X-ray sources ever, and the first candidate source to be widely accepted as a BH. Cygnus X-1 and LMC X-1 are wind-fed black hole binaries. The massive early O-type companion of J0536 could make this HMXB similar to these wind-fed BH systems.

Table V.1. Comparing Properties of Selected HMXBs

Source	Spectral Type	P_{orb} (d)	L_X (10^{35}erg s^{-1})	D (kpc)	M_O ($M_\odot$)	M_X ($M_\odot$)
J0536	O5III(f)	$\gtrsim$10	2.5	50	$\sim$45	>2–3
Cyg X-1	O9.7I	5.6	80	2.15	33	16
SS 433	A7Ib†	13.1	7	5.5	12.4	4.3
LMC X-1	O8(f)	3.9	2000	50	32	10.91
LMC X-4	O7IV	1.4	120	50	14.5	1.25
SMC X-1	B0I	3.9	$\gtrsim$3000	60	17.2	1.6
LS 5039	O6.5V((f))	3.9	0.5	2.5	22.9	3.7
Cen X-3	O6.5II	2.1	$\gtrsim$1000	10	15.6	1.49

Note. — †The BH is within a common envelope with the evolving donor, leading to large outflows and hence supergiant temperatures, affecting the classification of the companion and causing it to appear to be of later type.

5.4.1.3 LMC X-4

Of course, the uncertainty in the mass of the compact object in J0536 means that a neutron star cannot be ruled out. LMC X-4 could be an example of the kind of system J0536 might represent.

5.4.1.4 SMC X-1 and Cen X-3

SMC X-1 and Cen X-3 are typical Roche-lobe overflow systems with neutron stars and massive companions. The X-ray variability of the system and spectral features could reveal J0536 to be this type of system. .

5.4.2 The Nature of the 50-day Timescale in J0536

Figure 5.2 shows the velocity curve for the Balmer absorption lines. Assuming in the outer layers of the stellar atmosphere, The motion of the Balmer lines is tied to the orbital motion of this system. There is a ∼50-day trend in the variation of the velocity measurements of these lines, which is consistent with the ∼ tens of days variation discussed in Seward et al. (2012), and supports the HMXB interpretation of this system.

5.4.3 Does J0536 contain a black hole?

Based on X-ray and optical data, Seward et al. (2012) concluded that the SNR hosts a HMXB at its center. The X-ray data show no pulsations, and the spectrum is consistent with the object being either a NS or a BH. The optical component of the HMXB is CAL60, a O5III(f) star that shows radial velocity variations of up to 30 km s^{-1} (Crampton et al., 1985; Seward et al., 2012). A typical O5III star has a mass $M_O \approx 45$ M⊙ and radius $R_O \approx 15$ $R_\odot$ (Martins, Schaerer, and Hillier, 2005). We can calculate the allowed range of some orbital parameters as follows. We take a conservative range of the semi-amplitude of the O star's radial velocity, $K_{\rm opt} \in$ (10–40) km s^{-1}. We consider compact object masses M_X between 1–5 $M_\odot$, and calculate the binary orbital period and size of the O star's Roche lobe for each value of $K_{\rm opt}$ and M_X. The results are shown in Fig. 5.5. Taking this into consideration, we infer that $K_{\rm opt} \sim 30$ km s^{-1} for a $P_{\rm orb} \lesssim 50$ d. It is possible that the compact object in

J0536 is a BH with $M_X > 3$, although the presence of a NS cannot be ruled out with the current data.

5.5 Summary & Conclusions

We conducted a radial velocity study of J0536, the X-ray point source in CAL60. The Doppler motion of Balmer lines show that a ∼50-day trend is apparent in the velocity curve of the binary, suggesting that the orbital period is consistent with the suggestion of Seward et al. (2012) that $P_{\rm orb} \sim$ tens of days. The trailed spectra of the system shows a dramatic variation in the He II 4686 absorption feature, which we interpret as the accretion disk filling in the absorption feature at 4686 Å to varying degrees based upon the phase of the binary orbit, and is thus another possible indicator of the orbital period of the system. It's possible that this variation is due to variable accretion onto the central compact object. These observations bolster the interpretation of the bright X-ray point source J0536 as a HMXB; however the current data could not settle whether the central source is a NS or a BH. We suggest that based on the amplitude velocity variations of the Balmer absorption lines ~ 30 km s^{-1} and the likely $\sim 10 - 50$ day orbital period, J0536 is an accreting compact binary and the compact object is at least $\sim$ 2–3 $M_\odot$. We have planned follow-up observations with much better signal-to-noise, which we will use to further constrain the orbital period of J0536 and to determine whether it contains a black hole.

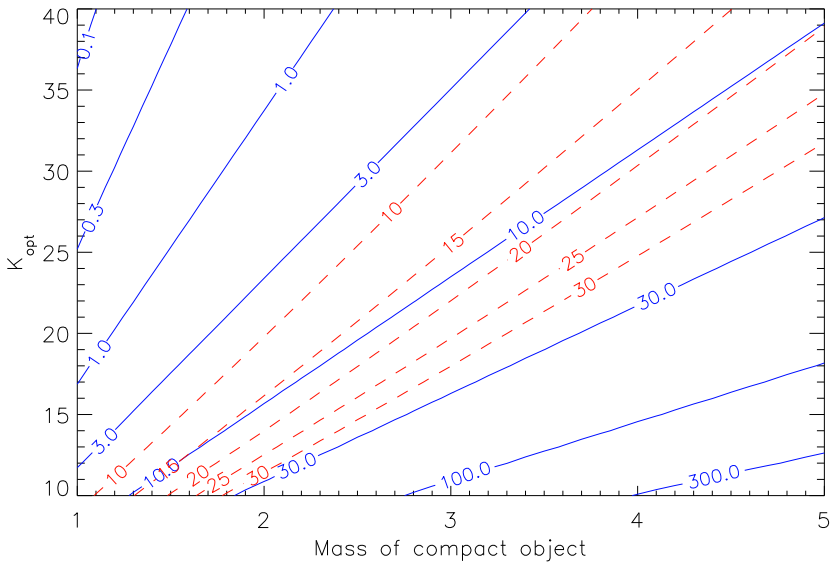

Figure 5.5: Calculated properties for the J0536 binary system as a function of the orbital velocity $K_{\rm opt}$ (km s^{-1}; vertical axis) and compact object mass M_X ($M_\odot$; horizontal axis). We assume an edge on system with a 45 $M_\odot$ O star. The red dashed lines are contours of constant Roche lobe radius in solar radii. Radii of non-interacting O5 stars range from 11 $R_\odot$ for luminosity class V to -20 $R_\odot$ for supergiants (Martins et al., 2005). Requiring that the O star be fully contained in its Roche lobe limits the acceptable values of $K_{\rm opt}$ and M_X to the lower right side of this figure. Solid blue lines are contours of orbital period in days. For the region allowed by the Roche lobe constraints, the orbital period must be about a week or longer.

Chapter VI

FUTURE WORK

In this thesis, we studied the very-long-term temporal variability of X-ray binaries in the Milky Way ("the Galaxy") as well as in nearby galaxies. We showed that by studying (quasi-)periods that are weeks to years in duration, we can shed light on the nature of ultraluminous X-ray sources (ULXs), particularly how their long-term periodic modulations can point away from the interpretation of ULXs as hosts of intermediate-mass black holes (IMBHs). Rather, the long-term temporal variability is a sign of hyper-accretion, which likely is common to ULXs, is responsible for their enhanced brightness, and the cause of accretion-disk warping and/or precession of their polar jets. The project described in this thesis forms a foundation for many interesting future research directions related to ULXs and other high-mass X-ray binaries.

6.1 ULX Monitor

The controversy regarding ULXs continues due to the lack of observational constraints on their key properties, including their orbital periods. Many Galactic XRBs now have well determined component masses and evolutionary states from optical spectroscopy of their counterparts (see e.g. Casares, 2010). However, this has proven

extremely difficult for ULXs because of their faintness and location in crowded regions of their host galaxies (no individual counterpart of a ULX has yet yielded any useful kinematic mass constraints). Our first priority must then be to search for periodicities in ULXs, and this is necessarily restricted to the X-ray regime.

Ideally, such a program should be undertaken on nearby interacting galaxies, such as NGC 5774/5 and NGC4885/90, selected so as to provide 20 ULX ($L_X > 10^{39}$ erg s^{-1}) targets for variability studies. This would be the first systematic survey of the long-term properties of such an extensive ULX population, all of which are likely HMXBs with mass ratios that render them susceptible to such superorbital modulations. This requires Chandra's unrivaled spatial resolution and will also provide unique databases for a wide range of secondary science projects. However, before such a campaign is undertaken, we propose to first assess the available archival Chandra and Swift data, now that they combine to form a long temporal baseline for a few galaxies, in order to search for very-long-term periods.

6.2 Follow-up archival study of M31 X-ray sources

Multi-epoch X-ray observations of nearby galaxies allow for the study of the long-term variability of their X-ray source populations. These populations are known to be dominated by X-ray binaries (XRBs; Fabbiano, 2006; Fabbiano and White, 2006). We know from previous temporal and spectral analysis on the most luminous XRBs in nearby galaxies that they exhibit behaviors similar to what is seen in the Galactic

XRBs (Fabbiano, 2006, and references therein). For example Kong et al. (2002) find that among the 204 sources detected in the nearby spiral galaxy M31, 50% are variable on the timescale of several weeks and 13 are transients. We expect that ultraluminous X-ray sources (ULXs) exhibit similar very-long-term modulations to those seen in the Galactic XRB population. Owing to the lack of regular, multi-epoch observations of extragalactic X-ray transients, not much is known about the variability of XRBs on timescales of tens to hundreds of days. In Chapter III we presented our analysis of a 10-year baseline of X-ray data for a handful of persistently bright sources in M87. There is additional data in the *Chandra* archive covering a very long baseline (about 12 years) with potentially hundreds of interesting X-ray point sources that may exhibit long-term (quasi-) periodic and/or transient behavior. Such a project would make a natural extension to the work presented in Chapter III and form a nice complementary analysis for the proposed ULX monitoring with a well-designed sampling plan.

6.3 Follow-up observations of CAL60/J0536

In Chapter V we presented a radial velocity study of the CAL60 system (inspired by the work presented in Chapter IV), which is believed to contain an unusual HMXB. We were able to place mild constraints on the period of the system and the mass of the compact object, however higher signal-to-noise is needed to constrain the system further. We plan follow-up spectroscopic observations with the *Southern African*

Large Telescope (SALT), to achieve further constraints on the orbital period and mass ratio of the system.

References

Aharonian, F., A. G. Akhperjanian, K.-M. Aye, A. R. Bazer-Bachi, M. Beilicke, W. Benbow, D. Berge, P. Berghaus, K. Bernlöhr, C. Boisson, O. Bolz, V. Borrel, I. Braun, F. Breitling, A. M. Brown, J. B. Gordo, P. M. Chadwick, L.-M. Chounet, R. Cornils, L. Costamante, B. Degrange, H. J. Dickinson, A. Djannati-Ataï, L. O. Drury, G. Dubus, D. Emmanoulopoulos, P. Espigat, F. Feinstein, P. Fleury, G. Fontaine, Y. Fuchs, S. Funk, Y. A. Gallant, B. Giebels, S. Gillessen, J. F. Glicenstein, P. Goret, C. Hadjichristidis, M. Hauser, G. Heinzelmann, G. Henri, G. Hermann, J. A. Hinton, W. Hofmann, M. Holleran, D. Horns, A. Jacholkowska, O. C. de Jager, B. Khélifi, N. Komin, A. Konopelko, I. J. Latham, R. Le Gallou, A. Lemière, M. Lemoine-Goumard, N. Leroy, T. Lohse, A. Marcowith, J.-M. Martin, O. Martineau-Huynh, C. Masterson, T. J. L. McComb, M. de Naurois, S. J. Nolan, A. Noutsos, K. J. Orford, J. L. Osborne, M. Ouchrif, M. Panter, G. Pelletier, S. Pita, G. Pühlhofer, M. Punch, B. C. Raubenheimer, M. Raue, J. Raux, S. M. Rayner, A. Reimer, O. Reimer, J. Ripken, L. Rob, L. Rolland, G. Rowell, V. Sahakian, L. Saugé, S. Schlenker, R. Schlickeiser, C. Schuster, U. Schwanke, M. Siewert, H. Sol, D. Spangler, R. Steenkamp, C. Stegmann, J.-P. Tavernet, R. Terrier, C. G. Théoret, M. Tluczykont, G. Vasileiadis, C. Venter, P. Vincent, H. J. Völk, and S. J. Wagner, 2005: Discovery of Very High Energy Gamma Rays Associated with an X-ray Binary. *Science*, **309**, 746–749.

Bamba, A., M. Ueno, H. Nakajima, K. Mori, and K. Koyama, 2006: A detailed observation of a LMC supernova remnant DEM L241 with XMM-Newton. A&A, **450**, 585–591.

Barnard, R., J. L. Galache, M. R. Garcia, N. Nooraee, P. J. Callanan, A. Zezas, and S. S. Murray, 2012a: A Period Distribution of X-Ray Binaries Observed in the Central Region of M31 with Chandra and the Hubble Space Telescope. ApJ, **756**, 32.

Barnard, R., M. Garcia, and S. S. Murray, 2012b: 12 Years of X-Ray Variability in M31 Globular Clusters, Including 8 Black Hole Candidates, as Seen by Chandra. ApJ, **757**, 40.

Bate, M. R., I. A. Bonnell, C. J. Clarke, S. H. Lubow, G. I. Ogilvie, J. E. Pringle, and C. A. Tout, 2000: Observational implications of precessing protostellar discs and jets. MNRAS, **317**, 773–781.

Begelman, M. C., A. R. King, and J. E. Pringle, 2006: The nature of SS433 and the ultraluminous X-ray sources. MNRAS, **370**, 399–404.

Blondin, J. M. and M. P. Owen, 1997: Wind Accretion VS Roche Lobe Overflow in HMXBs. In Wickramasinghe, D. T., G. V. Bicknell, and L. Ferrario, eds., *IAU Colloq. 163: Accretion Phenomena and Related Outflows*, vol. 121 of *Astronomical Society of the Pacific Conference Series*, p. 361.

Blundell, K. M., M. G. Bowler, and L. Schmidtobreick, 2008: SS 433: Observation of the Circumbinary Disk and Extraction of the System Mass. ApJ, **678**, L47–L50.

Brenneman, L. W., 2007: *A spectral survey of black hole spin in active galactic nuclei*. Ph.D. thesis, University of Maryland, College Park.

Carpano, S., A. M. T. Pollock, A. R. King, J. Wilms, and M. Ehle, 2007: An ultraluminous supersoft source with a 4hour modulation in NGC 4631. A&A, **471**, L55–L58.

Casares, J., 2007: Observational evidence for stellar-mass black holes. In Karas, V. and G. Matt, eds., *IAU Symposium*, vol. 238 of *IAU Symposium*, pp. 3–12.

Casares, J., P. A. Charles, and T. Naylor, 1992: A 6.5-day periodicity in the recurrent nova V404 Cygni implying the presence of a black hole. Nature, **355**, 614–617.

Casares, J., M. Ribó, I. Ribas, J. M. Paredes, J. Martí, and A. Herrero, 2005: A possible black hole in the γ-ray microquasar LS 5039. MNRAS, **364**, 899–908.

Charles, P., W. Clarkson, R. Cornelisse, and C. Shih, 2008: Observational properties of accretion discs: Precessing and warped? , **51**, 768–774.

Charles, P., M. Kotze, and A. Rajoelimanana, 2010: Long-Term Optical/X-ray Variability of CVs, LMXBs and BeX Sources. In Kologera, V. and M. van der Sluys, eds., *American Institute of Physics Conference Series*, vol. 1314 of *American Institute of Physics Conference Series*, pp. 303–311.

Charles, P. A. and M. J. Coe, 2006: *Optical, ultraviolet and infrared observations of X-ray binaries*. pp. 215–265.

Colbert, E. J. M., T. M. Heckman, A. F. Ptak, D. K. Strickland, and K. A. Weaver, 2004: Old and Young X-Ray Point Source Populations in Nearby Galaxies. ApJ, **602**, 231–248.

Cowley, A. P., D. Crampton, J. B. Hutchings, D. J. Helfand, T. T. Hamilton, J. R. Thorstensen, and P. A. Charles, 1984: Optical counterparts of the Large Magellanic Cloud X-ray point sources. ApJ, **286**, 196–208.

Cowley, A. P., P. C. Schmidtke, K. Ebisawa, F. Makino, R. A. Remillard, D. Crampton, J. B. Hutchings, S. Kitamoto, and A. Treves, 1991: Discovery of a long-term periodic variation in LMC X-3. ApJ, **381**, 526–533.

Crampton, D., A. P. Cowley, and J. B. Hutchings, 1980: The probable binary nature of SS 433. ApJ, **235**, L131–L135.

Crampton, D., A. P. Cowley, I. B. Thompson, and J. B. Hutchings, 1985: Further spectroscopy of LMC X-ray candidates. AJ, **90**, 43–48.

Davies, R. D., K. H. Elliott, and J. Meaburn, 1976: The nebular complexes of the large and small Magellanic Clouds. MmRAS, **81**, 89–128.

Davis, S. W., R. Narayan, Y. Zhu, D. Barret, S. A. Farrell, O. Godet, M. Servillat, and N. A. Webb, 2011: The Cool Accretion Disk in ESO 243-49 HLX-1: Further Evidence of an Intermediate-mass Black Hole. ApJ, **734**, 111.

Di Matteo, T., V. Springel, and L. Hernquist, 2005: Energy input from quasars regulates the growth and activity of black holes and their host galaxies. Nature, **433**, 604–607.

Done, C., M. Gierliński, and A. Kubota, 2007: Modelling the behaviour of accretion flows in X-ray binaries. Everything you always wanted to know about accretion but were afraid to ask. A&A Rev., **15**, 1–66.

Dubus, G., 2013: Gamma-ray binaries and related systems. A&A Rev., **21**, 64.

Dubus, G., J.-P. Lasota, J.-M. Hameury, and P. Charles, 1999: X-ray irradiation in low-mass binary systems. MNRAS, **303**, 139–147.

Eikenberry, S. S., P. B. Cameron, B. W. Fierce, D. M. Kull, D. H. Dror, J. R. Houck, and B. Margon, 2001: Twenty Years of Timing SS 433. ApJ, **561**, 1027–1033.

Eldridge, J. J., M. Fraser, S. J. Smartt, J. R. Maund, and R. M. Crockett, 2013: The death of massive stars - II. Observational constraints on the progenitors of Type Ibc supernovae. MNRAS, **436**, 774–795.

Esin, A. A., J. E. McClintock, and R. Narayan, 1997: Advection-dominated Accretion and the Spectral States of Black Hole X-Ray Binaries: Application to Nova MUSCAE 1991. ApJ, **489**, 865.

Fabbiano, G., 1989: X rays from normal galaxies. ARA&A, **27**, 87–138.

—, 2006: Populations of X-Ray Sources in Galaxies. ARA&A, **44**, 323–366.

Fabbiano, G., A. R. King, A. Zezas, T. J. Ponman, A. Rots, and F. Schweizer, 2003: A Variable Ultraluminous Supersoft X-Ray Source in "The Antennae": Stellar-Mass Black Hole or White Dwarf? ApJ, **591**, 843–849.

Fabbiano, G. and N. E. White, 2006: *Compact stellar X-ray sources in normal galaxies*. pp. 475–506.

Fabbiano, G., A. Zezas, and S. S. Murray, 2001: Chandra Observations of "The Antennae" Galaxies (NGC 4038/9). ApJ, **554**, 1035–1043.

Fabian, A. C. and K. Iwasawa, 2000: Broad Fe-K lines from Seyfert Galaxies. *Advances in Space Research*, **25**, 471–480.

Fabrika, S., 2004: The jets and supercritical accretion disk in SS433. *Astrophysics and Space Physics Reviews*, **12**, 1–152.

Fabrika, S. and P. Abolmasov, 2007: The Enigma of Ultraluminous X-ray Sources may be Resolved by 3D-Spectroscopy (MPFS Data). In Kissler-Patig, M., J. R. Walsh, and M. M. Roth, eds., *Science Perspectives for 3D Spectroscopy*, p. 309.

Fabrika, S. and A. Mescheryakov, 2001: Face-on SS 433 stars as a possible new type of extragalactic X-ray sources. In Schilizzi, R. T., ed., *Galaxies and their Constituents at the Highest Angular Resolutions*, vol. 205 of *IAU Symposium*, p. 268.

Farrell, S. A., N. A. Webb, D. Barret, O. Godet, and J. M. Rodrigues, 2009: An intermediate-mass black hole of over 500 solar masses in the galaxy ESO243-49. Nature, **460**, 73–75.

Feast, M., 1999: Cepheids as Distance Indicators. PASP, **111**, 775–793.

Ferrarese, L. and D. Merritt, 2000: A Fundamental Relation between Supermassive Black Holes and Their Host Galaxies. ApJ, **539**, L9–L12.

Foster, D. L., P. A. Charles, and K. Holley-Bockelmann, 2010: Interpretation of the 115 Day Periodic Modulation in the X-ray Flux of NGC 5408 X-1. ApJ, **725**, 2480–2484.

Foster, D. L., P. A. Charles, D. A. Swartz, R. Misra, and K. G. Stassun, 2013: Monitoring the very-long-term variability of X-ray sources in the giant elliptical galaxy M87. MNRAS, **432**, 1375–1381.

Frank, J., A. R. King, and J.-P. Lasota, 1987: The light curves of low-mass X-ray binaries. A&A, **178**, 137–142.

Franx, M., G. Illingworth, and T. Heckman, 1989: Major and minor axis kinematics of 22 ellipticals. ApJ, **344**, 613–636.

Fridriksson, J. K., J. Homan, W. H. G. Lewin, A. K. H. Kong, and D. Pooley, 2008: The Long-Term Variability of the X-Ray Sources in NGC 6946 and NGC 4485/4490. ApJS, **177**, 465–492.

Fryer, C. L., 1999: Mass Limits For Black Hole Formation. ApJ, **522**, 413–418.

—, 2013: Compact Object Formation and the Supernova Explosion Engine. *ArXiv e-prints*.

Gaensler, B. M., S. P. Hendrick, S. P. Reynolds, and K. J. Borkowski, 2003: Discovery of a New Pulsar Wind Nebula in the Large Magellanic Cloud. ApJ, **594**, L111–L114.

Gebhardt, K., R. Bender, G. Bower, A. Dressler, S. M. Faber, A. V. Filippenko, R. Green, C. Grillmair, L. C. Ho, J. Kormendy, T. R. Lauer, J. Magorrian, J. Pinkney, D. Richstone, and S. Tremaine, 2000: A Relationship between Nuclear Black Hole Mass and Galaxy Velocity Dispersion. ApJ, **539**, L13–L16.

Gebhardt, K., D. Richstone, S. Tremaine, T. R. Lauer, R. Bender, G. Bower, A. Dressler, S. M. Faber, A. V. Filippenko, R. Green, C. Grillmair, L. C. Ho, J. Kormendy, J. Magorrian, and J. Pinkney, 2003: Axisymmetric Dynamical Models of the Central Regions of Galaxies. ApJ, **583**, 92–115.

Gehrels, N., 1986: Confidence limits for small numbers of events in astrophysical data. ApJ, **303**, 336–346.

Gerend, D. and P. E. Boynton, 1976: Optical clues to the nature of Hercules X-1/HZ Herculis. ApJ, **209**, 562–573.

Gies, D. R. and C. T. Bolton, 1986: The optical spectrum of HDE 226868 = Cygnus X-1. II Spectrophotometry and mass estimates. ApJ, **304**, 371–393.

Gies, D. R., M. V. McSwain, R. L. Riddle, Z. Wang, P. J. Wiita, and D. W. Wingert, 2002: The Spectral Components of SS 433. ApJ, **566**, 1069–1083.

Gladstone, J. C. and T. P. Roberts, 2009: The ultraluminous X-ray source population of NGC 4485/4490. MNRAS, **397**, 124–134.

Gladstone, J. C., T. P. Roberts, and C. Done, 2009: The ultraluminous state. MNRAS, **397**, 1836–1851.

Godet, O., B. Plazolles, T. Kawaguchi, J.-P. Lasota, D. Barret, S. A. Farrell, V. Braito, M. Servillat, N. Webb, and N. Gehrels, 2012: Investigating Slim Disk Solutions for HLX-1 in ESO 243-49. ApJ, **752**, 34.

Greene, J., C. D. Bailyn, and J. A. Orosz, 2001: Optical and Infrared Photometry of the Microquasar GRO J1655-40 in Quiescence. ApJ, **554**, 1290–1297.

Greiner, J., J. G. Cuby, and M. J. McCaughrean, 2001: An unusually massive stellar black hole in the Galaxy. Nature, **414**, 522–525.

Grisé, F., P. Kaaret, S. Corbel, D. Cseh, and H. Feng, 2013: A long-term X-ray monitoring of the ultraluminous X-ray source NGC 5408 X-1 with Swift reveals the presence of dips but no orbital period. MNRAS, **433**, 1023–1038.

Gültekin, K., D. O. Richstone, K. Gebhardt, T. R. Lauer, S. Tremaine, M. C. Aller, R. Bender, A. Dressler, S. M. Faber, A. V. Filippenko, R. Green, L. C. Ho, J. Kormendy, J. Magorrian, J. Pinkney, and C. Siopis, 2009: The M-σ and M-L Relations in Galactic Bulges, and Determinations of Their Intrinsic Scatter. ApJ, **698**, 198–221.

Haynes, R. F., M. M. Komesaroff, D. L. Jauncey, J. L. Caswell, D. K. Milne, M. J. Kesteven, K. J. Wellington, and R. A. Preston, 1986: A radio nebula associated with Circinus X-1. Nature, **324**, 233–235.

Heger, A., 2013: Astrophysics: Going supernova. Nature, **494**, 46–47.

Heger, A., C. L. Fryer, S. E. Woosley, N. Langer, and D. H. Hartmann, 2003: How Massive Single Stars End Their Life. ApJ, **591**, 288–300.

Heger, A. and S. E. Woosley, 2002: The Nucleosynthetic Signature of Population III. ApJ, **567**, 532–543.

Hénault-Brunet, V., L. M. Oskinova, M. A. Guerrero, W. Sun, Y.-H. Chu, C. J. Evans, J. S. Gallagher, III, R. A. Gruendl, and J. Reyes-Iturbide, 2012: Discovery of a Be/X-ray pulsar binary and associated supernova remnant in the Wing of the Small Magellanic Cloud. MNRAS, **420**, L13–L17.

Hjellming, R. M. and M. P. Rupen, 1995: Episodic ejection of relativistic jets by the X-ray transient GRO J1655 - 40. Nature, **375**, 464–468.

Irwin, J. A., 2006: The remarkable stability of probable black hole low-mass X-ray binaries in nearby galaxies. MNRAS, **371**, 1903–1911.

Janka, H.-T., 2012: Explosion Mechanisms of Core-Collapse Supernovae. *Annual Review of Nuclear and Particle Science*, **62**, 407–451.

Jordan, A., 2004: *Studies of extragalactic globular clusters*. Ph.D. thesis, Rutgers The State University of New Jersey - New Brunswick, New Jersey, USA.

Jordán, A., P. Côté, L. Ferrarese, J. P. Blakeslee, S. Mei, D. Merritt, M. Milosavljević, E. W. Peng, J. L. Tonry, and M. J. West, 2004: The ACS Virgo Cluster Survey. III. Chandra and Hubble Space Telescope Observations of Low-Mass X-Ray Binaries and Globular Clusters in M87. ApJ, **613**, 279–301.

Kaaret, P. and S. Corbel, 2009: A Photoionized Nebula Surrounding and Variable Optical Continuum Emission from the Ultraluminous X-Ray Source in NGC 5408. ApJ, **697**, 950–956.

Kaaret, P., S. Corbel, A. H. Prestwich, and A. Zezas, 2003: Radio Emission from an Ultraluminous X-ray Source. *Science*, **299**, 365–368.

Karachentsev, I. D., M. E. Sharina, A. E. Dolphin, E. K. Grebel, D. Geisler, P. Guhathakurta, P. W. Hodge, V. E. Karachentseva, A. Sarajedini, and P. Seitzer, 2002: New distances to galaxies in the Centaurus A group. A&A, **385**, 21–31.

Katz, J. I., S. F. Anderson, S. A. Grandi, and B. Margon, 1982: Nodding motions of accretion rings and disks - A short-term period in SS 433. ApJ, **260**, 780–793.

Kilkenny, D. and H. Worters, 2012: *The SAAO 1.9-m Telescope and Grating Spectrograph*. pp. 1–115.

King, A., 2008a: Hyperaccretion. , **51**, 775–777.

King, A. R., 2002: The brightest black holes. MNRAS, **335**, L13–L16.

—, 2008b: Accretion rates and beaming in ultraluminous X-ray sources. MNRAS, **385**, L113–L115.

—, 2009: Masses, beaming and Eddington ratios in ultraluminous X-ray sources. MNRAS, **393**, L41–L44.

King, A. R., R. E. Taam, and M. C. Begelman, 2000: The Evolutionary Status of SS 433. ApJ, **530**, L25–L28.

Kong, A. K. H., 2011: Monitoring Variable X-ray Sources in Nearby Galaxies. *ArXiv e-prints*.

Kong, A. K. H., M. R. Garcia, F. A. Primini, S. S. Murray, R. Di Stefano, and J. E. McClintock, 2002: X-Ray Point Sources in the Central Region of M31 as Seen by Chandra. ApJ, **577**, 738–756.

Kormendy, J. and D. Richstone, 1995: Inward Bound—The Search For Supermassive Black Holes In Galactic Nuclei. ARA&A, **33**, 581.

Kotani, T., S. A. Trushkin, R. Valiullin, K. Kinugasa, S. Safi-Harb, N. Kawai, and M. Namiki, 2006: A Massive Jet Ejection Event from the Microquasar SS 433 Accompanying Rapid X-Ray Variability. ApJ, **637**, 486–493.

Kotze, M. M. and P. A. Charles, 2010: Very long-term X-ray variations in LMXBs: solar cycle-like variations in the donor? MNRAS, **402**, L16–L20.

Kozai, Y., 1962: Secular perturbations of asteroids with high inclination and eccentricity. AJ, **67**, 591.

Kubota, K., Y. Ueda, S. Fabrika, A. Medvedev, E. A. Barsukova, O. Sholukhova, and V. P. Goranskij, 2010: Subaru And Gemini Observations Of SS 433: New Constraint On The Mass Of The Compact Object. ApJ, **709**, 1374–1386.

Lang, C. C., P. Kaaret, S. Corbel, and A. Mercer, 2007: A Radio Nebula Surrounding the Ultraluminous X-Ray Source in NGC 5408. ApJ, **666**, 79–85.

Lasota, J.-P., 2001: The disc instability model of dwarf novae and low-mass X-ray binary transients. , **45**, 449–508.

Liu, Q. Z., J. van Paradijs, and E. P. J. van den Heuvel, 2006: Catalogue of high-mass X-ray binaries in the Galaxy (4th edition). A&A, **455**, 1165–1168.

Lomb, N. R., 1976: Least-squares frequency analysis of unequally spaced data. Ap&SS, **39**, 447–462.

Long, K. S., S. Dodorico, P. A. Charles, and M. A. Dopita, 1981a: Observations of the X-ray sources in the nearby SC galaxy M33. ApJ, **246**, L61–L64.

Long, K. S., D. J. Helfand, and D. A. Grabelsky, 1981b: A soft X-ray study of the Large Magellanic Cloud. ApJ, **248**, 925–944.

Magorrian, J., S. Tremaine, D. Richstone, R. Bender, G. Bower, A. Dressler, S. M. Faber, K. Gebhardt, R. Green, C. Grillmair, J. Kormendy, and T. Lauer, 1998: The Demography of Massive Dark Objects in Galaxy Centers. AJ, **115**, 2285–2305.

Makishima, K., A. Kubota, T. Mizuno, T. Ohnishi, M. Tashiro, Y. Aruga, K. Asai, T. Dotani, K. Mitsuda, Y. Ueda, S. Uno, K. Yamaoka, K. Ebisawa, Y. Kohmura, and K. Okada, 2000: The Nature of Ultraluminous Compact X-Ray Sources in Nearby Spiral Galaxies. ApJ, **535**, 632–643.

Maloney, P. R., M. C. Begelman, and M. A. Nowak, 1998: Radiation-driven Warping. II. Nonisothermal Disks. ApJ, **504**, 77.

Maloney, P. R., M. C. Begelman, and J. E. Pringle, 1996: Radiation-driven Warping: The Origin of WARPS and Precession in Accretion Disks. ApJ, **472**, 582.

Margon, B., 1984: Observations of SS 433. ARA&A, **22**, 507–536.

Margon, B., S. A. Grandi, and R. A. Downes, 1980: The 164 and 13 day periods of SS 433 - Confirmation of the kinematic model. ApJ, **241**, 306–315.

Martins, F., D. Schaerer, and D. J. Hillier, 2005: A new calibration of stellar parameters of Galactic O stars. A&A, **436**, 1049–1065.

Massey, P., 2002: A UBVR CCD Survey of the Magellanic Clouds. ApJS, **141**, 81–122.

Mathewson, D. S., V. L. Ford, I. R. Tuohy, B. Y. Mills, A. J. Turtle, and D. J. Helfand, 1985: Supernova remnants in the Magellanic Clouds. III. ApJS, **58**, 197–200.

Mazeh, T., E. N. Leibowitz, O. Lahav, and Y. Sheffer, 1980: SS 433. IAU Circ., **3527**, 2.

Medvedev, M. V. and N. Murray, 2002: Hot Settling Accretion Flow onto a Spinning Black Hole. ApJ, **581**, 431–437.

Mereghetti, S., T. Belloni, M. Shara, and L. Drissen, 1994: On the nature of the X-ray emission from 1E 1024.0-5732/Wack 2134: The first X-ray-selected Wolf-Rayet star. ApJ, **424**, 943–946.

Merloni, A., S. Heinz, and T. di Matteo, 2003: A Fundamental Plane of black hole activity. MNRAS, **345**, 1057–1076.

Merloni, A., S. Heinz, and T. Di Matteo, 2005: A Fundamental Plane of Black Hole Activity: Pushing Forward the Unification Scheme. Ap&SS, **300**, 45–53.

Middleton, M., C. Done, M. Gierliński, and S. W. Davis, 2006: Black hole spin in GRS 1915+105. MNRAS, **373**, 1004–1012.

Miller, J. M., 2005: Present Evidence for Intermediate Mass Black Holes in ULXs and Future Prospects. Ap&SS, **300**, 227–238.

Miller, M. C. and E. J. M. Colbert, 2004: Intermediate-Mass Black Holes. *International Journal of Modern Physics D*, **13**, 1–64.

Mirabel, I. F., 2012: Gamma-Ray Binaries Revealed. *Science*, **335**, 175–.

Mirabel, I. F. and L. F. Rodríguez, 1994: A superluminal source in the Galaxy. Nature, **371**, 46–48.

Morgan, E. H., R. A. Remillard, and J. Greiner, 1997: RXTE Observations of QPOs in the Black Hole Candidate GRS 1915+105. ApJ, **482**, 993.

Mukai, K., W. D. Pence, S. L. Snowden, and K. D. Kuntz, 2003: Chandra Observation of Luminous and Ultraluminous X-Ray Binaries in M101. ApJ, **582**, 184–189.

Orio, M., 2006: A Close Look at the Population of Supersoft and Quasi-soft X-Ray Sources Observed in M31 with XMM-Newton. ApJ, **643**, 844–862.

Petterson, J. A., 1977: The 35 day cycle of the X-ray binary Hercules X-1. ApJ, **218**, 783–791.

Pollock, A. M. T., M. F. Corcoran, I. R. Stevens, and P. M. Williams, 2005: Bulk Velocities, Chemical Composition, and Ionization Structure of the X-Ray Shocks in WR 140 near Periastron as Revealed by the Chandra Gratings. ApJ, **629**, 482–498.

Portegies Zwart, S. F. and S. L. W. McMillan, 2002: The Runaway Growth of Intermediate-Mass Black Holes in Dense Star Clusters. ApJ, **576**, 899–907.

Poutanen, J., G. Lipunova, S. Fabrika, A. G. Butkevich, and P. Abolmasov, 2007: Supercritically accreting stellar mass black holes as ultraluminous X-ray sources. MNRAS, **377**, 1187–1194.

Press, W. H. and G. B. Rybicki, 1989: Fast algorithm for spectral analysis of unevenly sampled data. ApJ, **338**, 277–280.

Rappaport, S. A., P. Podsiadlowski, and E. Pfahl, 2005: Stellar-mass black hole binaries as ultraluminous X-ray sources. MNRAS, **356**, 401–414.

Rau, A., J. Greiner, and M. L. McCollough, 2003: The 590 Day Long-Term Periodicity of the Microquasar GRS 1915+105. ApJ, **590**, L37–L40.

Reig, P., 1999: On the nature of the X-ray source 1E 1024.0-5732/Wack 2134. A&A, **345**, 576–582.

Remillard, R. A., E. H. Morgan, J. E. McClintock, C. D. Bailyn, and J. A. Orosz, 1999: RXTE Observations of 0.1-300 HZ Quasi-periodic Oscillationsin the Microquasar GRO J1655-40. ApJ, **522**, 397–412.

Remillard, R. A., G. J. Sobczak, M. P. Muno, and J. E. McClintock, 2002: Characterizing the Quasi-periodic Oscillation Behavior of the X-Ray Nova XTE J1550-564. ApJ, **564**, 962–973.

Reynolds, C. S. and M. A. Nowak, 2003: Fluorescent iron lines as a probe of astrophysical black hole systems. Phys. Rep., **377**, 389–466.

Rico, J., 2008: The Variable Superorbital Modulation of Cygnus X-1. ApJ, **683**, L55–L58.

Robertson, B., L. Hernquist, T. J. Cox, T. Di Matteo, P. F. Hopkins, P. Martini, and V. Springel, 2006: The Evolution of the M_{BH}-σ Relation. ApJ, **641**, 90–102.

Scargle, J. D., 1982: Studies in astronomical time series analysis. II - Statistical aspects of spectral analysis of unevenly spaced data. ApJ, **263**, 835–853.

Servillat, M., S. A. Farrell, D. Lin, O. Godet, D. Barret, and N. A. Webb, 2011: X-Ray Variability and Hardness of ESO 243-49 HLX-1: Clear Evidence for Spectral State Transitions. ApJ, **743**, 6.

Seward, F. D., P. A. Charles, D. L. Foster, J. R. Dickel, P. S. Romero, Z. I. Edwards, M. Perry, and R. M. Williams, 2012: DEM L241, a Supernova Remnant Containing a High-mass X-Ray Binary. ApJ, **759**, 123.

Shakura, N. I. and R. A. Sunyaev, 1973: Black holes in binary systems. Observational appearance. A&A, **24**, 337–355.

Shaposhnikov, N. and L. Titarchuk, 2009: Determination of Black Hole Masses in Galactic Black Hole Binaries Using Scaling of Spectral and Variability Characteristics. ApJ, **699**, 453–468.

Silk, J. and M. J. Rees, 1998: Quasars and galaxy formation. A&A, **331**, L1–L4.

Soria, R., R. P. Fender, D. C. Hannikainen, A. M. Read, and I. R. Stevens, 2006: An ultraluminous X-ray microquasar in NGC5408? MNRAS, **368**, 1527–1539.

Strohmayer, T. E., 2001: Discovery of a 450 HZ Quasi-periodic Oscillation from the Microquasar GRO J1655-40 with the Rossi X-Ray Timing Explorer. ApJ, **552**, L49–L53.

—, 2009: Discovery of a 115 Day Orbital Period in the Ultraluminous X-Ray Source NGC 5408 X-1. ApJ, **706**, L210–L214.

Strohmayer, T. E. and R. F. Mushotzky, 2009: Evidence for an Intermediate-mass Black Hole in NGC 5408 X-1. ApJ, **703**, 1386–1393.

Strohmayer, T. E., R. F. Mushotzky, L. Winter, R. Soria, P. Uttley, and M. Cropper, 2007: Quasi-periodic Variability in NGC 5408 X-1. ApJ, **660**, 580–586.

Swartz, D. A., K. K. Ghosh, V. Suleimanov, A. F. Tennant, and K. Wu, 2002: Chandra Discovery of Luminous Supersoft X-Ray Sources in M81. ApJ, **574**, 382–397.

Szuszkiewicz, E. and J. C. Miller, 2001: Non-linear evolution of thermally unstable slim accretion discs with a diffusive form of viscosity. MNRAS, **328**, 36–44.

Tanaka, Y., K. Nandra, A. C. Fabian, H. Inoue, C. Otani, T. Dotani, K. Hayashida, K. Iwasawa, T. Kii, H. Kunieda, F. Makino, and M. Matsuoka, 1995: Gravitationally redshifted emission implying an accretion disk and massive black hole in the active galaxy MCG-6-30-15. Nature, **375**, 659–661.

Tennant, A. F., A. C. Fabian, and R. A. Shafer, 1986: The discovery of X-ray bursts from CIR X-1. MNRAS, **219**, 871–881.

Titarchuk, L. and R. Fiorito, 2004: Spectral Index and Quasi-Periodic Oscillation Frequency Correlation in Black Hole Sources: Observational Evidence of Two Phases and Phase Transition in Black Holes. ApJ, **612**, 988–999.

Titarchuk, L., I. Lapidus, and A. Muslimov, 1998: Mechanisms for High-Frequency Quasi-periodic Oscillations in Neutron Star and Black Hole Binaries. ApJ, **499**, 315.

Tomasella, L., E. Cappellaro, M. Fraser, M. L. Pumo, A. Pastorello, G. Pignata, S. Benetti, F. Bufano, M. Dennefeld, A. Harutyunyan, T. Iijima, A. Jerkstrand, E. Kankare, R. Kotak, L. Magill, V. Nascimbeni, P. Ochner, A. Siviero, S. Smartt, J. Sollerman, V. Stanishev, F. Taddia, S. Taubenberger, M. Turatto, S. Valenti, D. E. Wright, and L. Zampieri, 2013: Comparison of progenitor mass estimates for the Type IIP SN 2012A. MNRAS, **434**, 1636–1657.

Trudolyubov, S. P., K. N. Borozdin, W. C. Priedhorsky, J. P. Osborne, M. G. Watson, K. O. Mason, and F. A. Cordova, 2002: The Discovery of a 2.78 Hour Periodic Modulation of the X-Ray Flux from Globular Cluster Source Bo 158 in M31. ApJ, **581**, L27–L31.

Tully, R. B., E. J. Shaya, I. D. Karachentsev, H. M. Courtois, D. D. Kocevski, L. Rizzi, and A. Peel, 2008: Our Peculiar Motion Away from the Local Void. ApJ, **676**, 184–205.

Urry, C. M. and P. Padovani, 1995: Unified Schemes for Radio-Loud Active Galactic Nuclei. PASP, **107**, 803.

van der Klis, M., J. H. Swank, W. Zhang, K. Jahoda, E. H. Morgan, W. H. G. Lewin, B. Vaughan, and J. van Paradijs, 1996: Discovery of Submillisecond Quasi-periodic Oscillations in the X-Ray Flux of Scorpius X-1. ApJ, **469**, L1.

van Dokkum, P. G. and S. A. Stanford, 2003: The Fundamental Plane at z=1.27: First Calibration of the Mass Scale of Red Galaxies at Redshifts z1. ApJ, **585**, 78–89.

Vikhlinin, A., E. Churazov, M. Gilfanov, R. Sunyaev, A. Dyachkov, N. Khavenson, R. Kremnev, K. Sukhanov, J. Ballet, P. Laurent, L. Salotti, A. Claret, J. F. Olive, M. Denis, P. Mandrou, and J. P. Roques, 1994: Discovery of a low-frequency broad quasi-periodic oscillation peak in the power density spectrum of Cygnus X-1 with Granat/SIGMA. ApJ, **424**, 395–400.

Volonteri, M., 2007: Evolution of Supermassive Black Holes. In Aschenbach, B., V. Burwitz, G. Hasinger, and B. Leibundgut, eds., *Relativistic Astrophysics Legacy and Cosmology - Einstein's Legacy*, p. 174.

Walborn, N. R., 1971: Some Spectroscopic Characteristics of the OB Stars: an Investigation of the Space Distribution of Certain OB Stars and the Reference Frame of the Classification. ApJS, **23**, 257.

Watson, M. G., G. C. Stewart, A. R. King, and W. Brinkmann, 1986: Doppler-shifted X-ray line emission from SS433. MNRAS, **222**, 261–271.

Webster, B. L. and P. Murdin, 1972: Cygnus X-1-a Spectroscopic Binary with a Heavy Companion ? Nature, **235**, 37–38.

Wen, L., A. M. Levine, R. H. D. Corbet, and H. V. Bradt, 2006: A Systematic Search for Periodicities in RXTE ASM Data. ApJS, **163**, 372–392.

Williams, R. M., Y.-H. Chu, J. R. Dickel, R. Petre, R. C. Smith, and M. Tavarez, 1999: Supernova Remnants in the Magellanic Clouds. III. an X-Ray Atlas of Large Magellanic Cloud Supernova Remnants. ApJS, **123**, 467–485.

Woosley, S. E., A. Heger, and T. A. Weaver, 2002: The evolution and explosion of massive stars. *Reviews of Modern Physics*, **74**, 1015–1071.

Woosley, S. E. and T. A. Weaver, 1995: The Evolution and Explosion of Massive Stars. II. Explosive Hydrodynamics and Nucleosynthesis. ApJS, **101**, 181.

Zampieri, L. and T. P. Roberts, 2009: Low-metallicity natal environments and black hole masses in ultraluminous X-ray sources. MNRAS, **400**, 677–686.